Assimilation of Swarm C atmospheric density observations into NRLMSISE-00

Analysis on the accuracy of orbit prediction

M. Callejón Cantero

Technical University of Delft

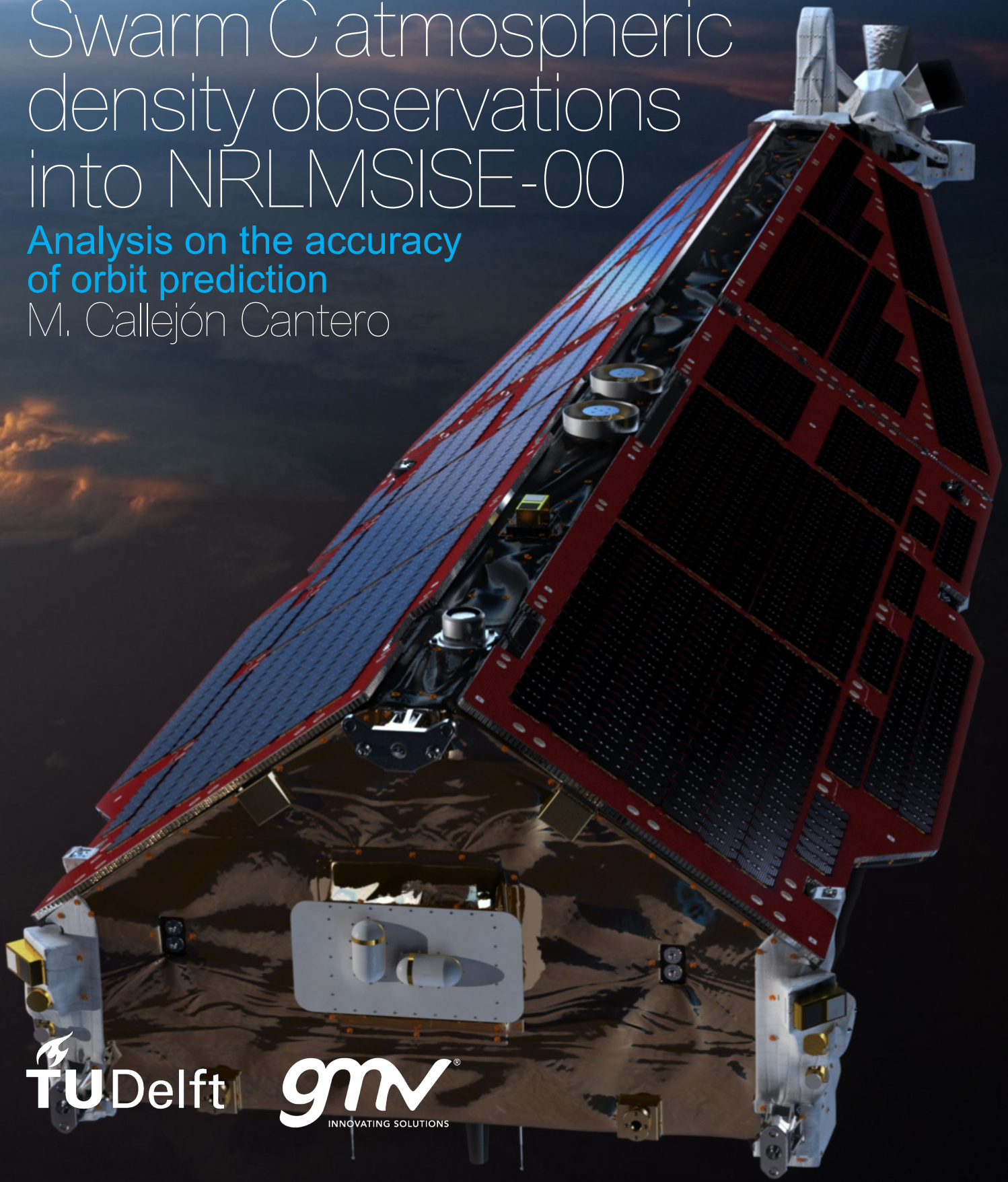

TU Delft

gmv INNOVATING SOLUTIONS

Assimilation of Swarm C atmospheric density observations into NRLMSISE-00

Analysis on the accuracy of orbit prediction

by

M. Callejón Cantero

to obtain the degree of Master of Science
at the Delft University of Technology,
to be defended publicly on Friday April 28th, 2023 at 13:00 PM.

Student number:	5140218	
Project duration:	June 1st, 2022 – April 28th, 2023	
Thesis committee:	Dr. ir. E. Mooij	TU Delft, chair
	Dr. ir. C. Siemes	TU Delft, supervisor
	Dr. ir. S. Speretta	TU Delft, examiner
	Dr. ir. A. Pastor	GMV, supervisor

Cover: Front of Swarm satellite. Image credit: ESA

TU Delft

gmv INNOVATING SOLUTIONS

Preface

With this master's thesis, I am concluding a four-year journey at TUDelft. It has been an incredible learning experience, and I am grateful for the opportunities and experiences that I have gained along the way. The journey was not easy, and there were moments when I thought about dropping out during the 2021-2022 academic year. However, with the support of my friends, family, and the opportunity of this master's thesis, I was able to push through and complete my studies.

I wish to express my sincere gratitude to my daily supervisors, Christian and Alejandro, for their invaluable feedback and the close collaboration between TUDelft and the private company GMV. Christian provided insightful comments related to the physical environment of the outer atmosphere, offering a broader perspective on the problem at hand. Alejandro, on the other hand, demonstrated a high level of commitment to the project, being flexible with the work needs throughout the entire internship, and fostering a very healthy work environment. Their constructive and complementary feedback has been instrumental in shaping the current outcome of this thesis.

This master's thesis topic provided an excellent platform for me to explore the fields of data analysis, atmospheric physics, and astrodynamics, all of which I found highly interesting and enjoyed mastering. Additionally, I have had ample opportunities to refine my programming skills in a specific domain, which will undoubtedly prove to be valuable assets in my upcoming career. In particular, I have recently signed a full-time employment contract with GMV, enabling me to apply the knowledge and skills gained during this internship.

I would like to thank Diego Escobar, head of the Space Surveillance and Tracking (SST) department at GMV Spain, for the opportunity given with this internship. I also want to express my work colleagues at GMV, that reminded me the reasons why I studied aerospace engineering in the first place, and helped me recover the motivation that was lost (but slowly appearing) at the beginning of the internship. Loris, Pietro, Lorenzo, Diego, Alex, Gabri, Rui (and sorry if I forgot about someone): muito obrigado per aver creato un ambiente di lavoro così accogliente!

Por último, y no menos importante, querría agradecer a mis padres, Ana y Miguel Ángel su incuantificable apoyo durante todos estos años. A mis amigos, los viejos y los nuevos, por las risas y el tiempo de calidad disfrutado en compañía. También, por qué no, al Farol de Cantarranas, en el que, según Google Maps, he pasado más tiempo que en la Facultad de Aeroespacial de TUDelft a lo largo de mi vida. Finalmente, agradecer a mi novia, Ester, por volcarse completamente en mi y por su infatigables muestras de amor a lo largo de los meses en los que he tenido que ceder parte de mi tiempo a este trabajo. Te quiero.

Abstract

The accurate prediction of satellite orbits is essential for the proper functioning of space-based services such as navigation, communication, and Earth observation. However, atmospheric drag is a significant source of error in satellite orbit prediction, especially in Low Earth Orbit (LEO), where the majority of space objects operate. The thermosphere, the outermost layer of Earth's atmosphere, plays a crucial role in determining atmospheric drag. However, the thermospheric density is subject to high levels of uncertainty, up to 30%, when computed from atmospheric models. This uncertainty is particularly relevant in LEO, where it can affect the operational lifespan of satellites.

To increase the accuracy of thermospheric density models, this paper presents an assessment of the accuracy of orbit predictions using empirical Thermospheric Mass Density (TMD) observations obtained from the Swarm C satellite. The study uses a Principal Component Analysis (PCA) to decompose a fine grid of density into the main temporal and spatial modes. Then, each of the modes is calibrated with Swarm C observations using a Least Squares Estimation (LSE) algorithm. The calibration is validated with the observation using unbiased metrics. These observations were assimilated into the NRLMSISE-00 (Picone et al., 2002) atmospheric model, and the resulting calibrated density model was used to predict the orbits of Swarm C, GRACE-FO and Sentinel 1-A satellites. To analyse the consistency of the results, a slicing window analysis was performed, and the median evolution of the windows was computed.

The results of the study indicate that a calibrated density model with a several satellite geometries, such as the cannonball model, a panel model, or a scaled panel model, can significantly improve the accuracy of orbit predictions in LEO. During March 2022, a period of medium solar activity, the median accuracy of orbit predictions for Swarm C was reduced from 20.67 km with NRLMSISE-00 to 13.75 km with the calibrated model and a scaled panel model geometry. During the same period, the median accuracy of orbit predictions for GRACE-FO C was reduced from 17.98 km with NRLMSISE-00 to 2.89 km with the calibrated model and an (unscaled) panel model geometry. These findings have important implications for the sustainable operation of satellites in the increasingly crowded space environment.

Contents

Nomenclature

Abbreviations

ANN	Artificial Neural Networks
C/DA	Calibration and Data Assimilation
CT	Clough Toucher interpolation
DCA	Dynamic Calibration Atmosphere
DTM2013	Drag Temperature Model 2013
DTM2020	Drag Temperature Model 2020
ECEF	Earth-Centred, Earth-Fixed
EMA	Equatorial Mass Density Anomaly
EnKF	Ensemble Kalman Filter
EnSRF	Ensemble Square-Root Kalman Filter
ESA	European Space Agency
EUV	Solar Extreme Ultraviolet
GCRF	Geocentric Celestial Reference Frame
GITM	Global Ionosphere-Thermosphere Model
GMST	Greenwich Mean Sidereal Time
GNSS	Global Navigation Satellite Systems
GPS	Global Positioning System
GSA	Global Sensitivity Analysis
HASDM	High Accuracy Satellite Drag Model
HWM14	Horizontal Wind Model 2014
ISA	International Standard Atmosphere
ISR	Incoherent Scatter Radar
ITRF	International Terrestial Reference Frame
JB08	Jacchia-Bowman 2008 model
LEO	Low Earth Orbit
LSE	Least Squares Estimation
LST	Local Solar Time
MAD	Median Absolute Deviation
MAORI	Multipurpose Advanced Orbit Restitution Infrastructure
NRLMSISE-00	US-Naval Research Laboratory Mass Spectrometer and Incoherent Scatter-radar Exosphere model - 2000 version
PCA	Principal Component Analysis
POD	Precise Orbit Determination
RBF	Radial Basis Functions
RMS	Root Mean Square
ROM	Reduced-Order Model
SRP	Solar Radiation Pressure
SSA	Space Situational Awareness
SST	Space Surveillance and Tracking
STM	Space Traffic Management
SVD	Singular Value Decomposition
TIE-GCM	Thermosphere-Ionosphere-Electrodynamics General Circulation Model
TLE	Two-Line Elements
TMD	Thermospheric Mass Density
TNW	Tangential-Normal-Along track reference frame
UKF	Unscented Kalman Filter
UV	Ultra-Violet

Characters & Symbols

Greek symbols

$\Delta \boldsymbol{z}$	Residuals of the Least Squares Estimation (LSE)
$\boldsymbol{\omega}_E$	Angular velocity of the Earth
$\boldsymbol{\Phi}$	State Transition Matrix
ρ	Amospheric density in drag acceleration
ρ_{400}	Density observations at 400 km of altitude
ρ_h	Density observations at Swarm C altitude
$\rho_{M,400}$	NLRMSISE-00 computed density at 400 km of altitude
$\rho_{M,h}$	NLRMSISE-00 computed density at Swarm C altitude
$\rho_{observations}$	Density observation distribution at Swarm C altitude
ρ_{model}	NLRMSISE-00 computed density distribution at Swarm C altitude
$\sigma_{observations}$	Standard deviation of the density observations
σ	Standard deviation metric
$\hat{\sigma}$	Median Absolute Deviation (MAD) estimator
μ	Mean of a distribution
θ_{GMST}	position of the GMST with respect to the vernal equinox
$\theta_{GMST,0h}$	GMST at midnight
θ_{LST}	Local Solar Time (LST)
λ	Longitude

Latin symbols

`ptm[0]`	Internal NLRMSISE-00 parameter
`pt0`	Internal NLRMSISE-00 parameter
`sec`	Seconds in the day
$\mathbf{a}_d$	Drag acsceleration
$\mathbf{f}$	Propagation function in the LSE algorithm
$\mathbf{g}$	Prediction function in the LSE algorithm
$\mathbf{h}$	Measurement function in the LSE algorithm
$\mathbf{n_d}$	Unit vector in the drag direction
$\mathbf{q}$	Quaternion
$\mathbf{r}_{GCRF}$	Position in the GCRF frame
$\mathbf{r}_{ITRF}$	Position in the ITRF frame
$\mathbf{r}_{pre,i}$	Range of the satellite with respect to Earth at prediction window i.
$\mathbf{r}_{pod,i}$	POD orbit at prediction window i
$\mathbf{x}$	State in the LSE
$\mathbf{y}$	Estimated parameter in the LSE
$\boldsymbol{z}$	Measurement in the LSE
$\hat{\mathbf{z}}$	Prediction of a measurement in the LSE
$\mathbf{E}$	PCA matrix that contains the spatial component
$\mathbf{H}$	Jacobian matrix in the LSE
$\mathbf{N}(t)$	Nutation matrix
$\mathbf{P}(t)$	Precesion matrix
$\mathbf{P}$	PCA matrix that contains the temporal component
$\mathbf{S}$	USV decomposition matrix
$\mathbf{R}(t)$	Rotation matrix
$\mathbf{U}$	USV decomposition matrix
$\mathbf{V}^T$	USV decomposition matrix
$\mathbf{X}_{grid}$	Grid that contains the spatial and temporal discretisation of NRLMSISE-00 computed density
$\bar{\mathbf{X}}$	Mean component of the USV decomposition
$\mathbf{W}$	Weights matrix in the LSE
$\mathbf{W}(t)$	Polar motion matrix
a_P	3-hourly geomagnetic index
k	Boltzmann constant
m	Median of a distribution
m_{atm}	Mass of each atmospheric particle
m_S	Mass of the satellite
r_{msi}	Norm of the range of the satellite with respect to POD orbit, for NLRMSISE-00 model
r_{cal}	Norm of the range of the satellite with respect to POD orbit, for the calibrated model
v	Velocity of the satellite in wind frame
t	Time
x	x axis
y	y axis
y_{mean}	Estimated parameter that contains the mean of the observations
z	z axis
a_P	Daily geomagnetic index
A	Area of the satellite
C_D	Drag coefficient
C_R	Solar radiation pressure coefficient
D_{st}	Disturbance storn time
$F_{10.7A}$	Solar proxy used by NRLMSISE-00 model

$F_{10.7}$	Solar proxy, daily solar radio flux density
$\bar{F}_{10.7}$	Solar proxy used by NRLMSISE-00 model
K_p	Geomagnetic index that measures the variation of geomagnetic field
M_{10}	Solar proxy used by Jacchia-Bowman models
S	Speed ratio of the satellite
S_{10}	Solar proxy used by Jacchia-Bowman models
T_{ex}	Temperature at the exosphere
T_{inc}	Local temperature of the atmosphere
Y_{10}	Mixed solar index used by Jacchia-Bowman models

1 Introduction

In recent years, there has been a growing interest in developing accurate and consistent models for the Earth's thermosphere, particularly for improving the accuracy of TMD prediction in LEO. The development of a calibrated model and its subsequent use for propagating several LEO objects is explored in this report, and the accuracy of the method is analysed.

Atmospheric drag is the main perturbation force acting on space objects on LEO under 600 km, excluding Earth's non-spherical gravity field. However, the uncertainty in satellite drag modelling is large compared to other perturbing forces. Drag contribution is described by Equation (1.1), where C_D is the drag coefficient of the object, A is the frontal area of the object in the direction of the wind, m_S is the mass of the object, v is the relative velocity with respect to wind, $\mathbf{n}_d$ is the unit vector in the same direction, and ρ is the TMD of the atmosphere. Usually, the ballistic coefficient $BC = \frac{m_S}{C_D A}$ is used as a unique parameter which defines the satellite geometry.

$$\mathbf{a}_d = \frac{1}{2} C_D \frac{A}{m_S} \rho v^2 \mathbf{n}_d \tag{1.1}$$

The uncertainty sources on drag derive from imprecise knowledge of each term of Equation (1.1): the object's shape and position; the wind acting on the object, which affects its inertial velocity; the aerodynamic coefficients of the object, either from an imperfect geometric model or an imperfect characterization of the gas-surface interaction; and the true physical TMD in the atmosphere. Several models exist that characterize the density in the upper layers of the atmosphere, but the uncertainty on the computed TMD can reach values up to 30%, or even higher (He et al., 2018). The accuracy of the models can be improved by assimilating atmospheric density observations retrieved from Precise Orbit Determination (POD) of LEO satellites. However, as C_D and ρ are multiplied by each other in Equation (1.1), the effect of estimating the C_D could overshadow any accuracy improvement of calibrating ρ.

One of the direct applications of improved drag modelling is space debris risk mitigation, as LEO region harbours more than 17500 objects in data at the end of 2021, which represents almost 60% of the objects orbiting Earth (ESA, 2022). LEO orbits are defined as those with a perigee and apogee below 2000 km. From the total LEO catalogued objects, around 33% of them are active payloads, 41% are fragmentation debris, 14% are composed of rocket fragmentation debris, and the remaining part is distributed among payload mission related objects, payload debris, rocket mission related debris, and other kind of objects (ESA, 2022, Table 3.1). A small part of objects orbiting Earth (0.32%) does not have an identified source. Most of the active payloads in LEO orbit the Earth below 600 km (ESA, 2022, Figure 3.6), where improvements in the atmospheric model are crucial. These numbers update the space debris statistics given by Klinkrad (2006): at the beginning of 2002, there were around 9000 objects catalogued, and 69.2% were in LEO. From 1963 to 2002, a near-linear increasing rate of 260 on-orbit objects per year was observed. The need to mitigate the effect of space debris on the space environment has become a critical need in recent years. However, the number of objects in orbit has exponentially raised since 2014, as a result of the increased number of commercial constellation satellite launches, as illustrated in Figure 1.1. Furthermore, the vast majority of potential collision events

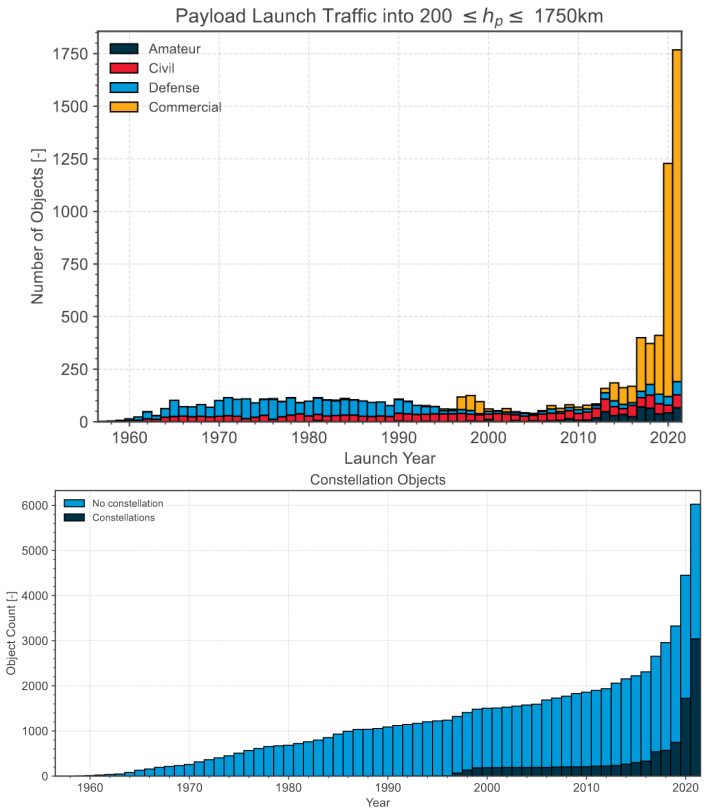

Figure 1.1: Evolution of the launch traffic near LEO per mission funding (top) and distinguishing constellations (bottom). Retrieved from (ESA, 2022, Figures 2.8 and 2.19).

found during 2021 took place for objects below 600 km. Reducing the uncertainty on possible collision events between objects, effectively increasing our confidence in the conjunction probability, is critical for the operating satellites in a crowded space environment. Final Space Situational Awareness (SSA) goal is to reduce fragmentation events, which are the main contribution to the debris catalogue. By 2002, 175 on-orbit fragmentation events had been detected (Klinkrad, 2006, section 2.2). By 2021, that number was augmented to 636 during all history, and 246 in the last 20 years (ESA, 2022, section 5.1). Although only a small percentage of the fragmentation events is due to collision events, all known fragmentations by 2002 occurred in orbits below 2000 km. The continued effort in SST, which aims to characterize every object in Earth orbit using different observations, as well as SSA and Space Traffic Management (STM), can hugely benefit from an improved TMD characterization.

The physical environment of the upper layers of the atmosphere is quite complex to model. Solar Extreme Ultraviolet (EUV) radiation, as well as coronal mass ejections, drive the temperature at the exopause, the composition of the exosphere, and the resulting density (Doornbos and Klinkrad, 2006). Both phenomena are characterized by proxies. For the heating of the atmosphere, caused by the EUV radiation, the $F_{10.7}$ index is usually used as a proxy. $F_{10.7}$ is measured in solar flux units: 1 sfu $= 10 \cdot 10^{22}\,\mathrm{Wm^{-2}Hz^{-1}}$. It represents the daily solar radio flux density at a wavelength of 10.7 cm, which can vary between 70 sfu to 370 sfu (He et al., 2018) depending on the solar activity, which alternates in cycles of 11 years. The 81-day mean value of $F_{10.7}$, $\bar{F}_{10.7}$, is also used in several models, as well as an adjusted proxy to exactly match one astronomical unit distance $\bar{F}_{10.7}$:

$$F_{10.7A} = \frac{F_{10.7}}{R_\odot} \tag{1.2}$$

In previous equation, $R_\odot$ is the distance of the Earth to the Sun in the moment of the observation. In the whole report, for conciseness, and when not stated differently, $F_{10.7}$ refers to the adjusted proxy. Coronal mass ejections and solar wind, on the other hand, highly affect the thermosphere during geomagnetic storms due to complex interactions with the magnetosphere and ionosphere (Bruinsma et al., 2021; Doornbos, 2011). The proxies a_P and K_p are usually used to account for geomagnetic activity, which

measure the variation of geomagnetic field with different scales (He et al., 2018). The disturbance storm time D_{st} indicates the intensity of horizontal magnetic field at the storm-time ring current, which is highly energized during magnetic storms (Bowman et al., 2008b).

When predicting the TMD in the close future, any uncertainty on these parameters propagates to the density, and afterwards to the drag. Therefore, it is crucial to have a realistic uncertainty characterization of existing parameters. Also, if the indices are predicted, as in a short- or medium-term propagation (propagation over days, up to one month), an extra source of uncertainty on the density inputs arises: the indices are not measurement of a proxy of solar activity, but the prediction of the proxy. Sáez Bo and Escobar Antón (2018) performed a statistical analysis of $F_{10.7}$ and A_P proxies. For $F_{10.7}$, a higher uncertainty on high solar activity was found and, regardless of the solar activity, $F_{10.7}$ uncertainty (1σ equivalent) could be bound to 5% for one-day prediction, and, for A_P, no correlation with the solar activity was found, and A_P uncertainty could be bound to 50%. Licata et al. (2020) analysed the uncertainty of the drivers for several solar and geomagnetic combinations and propagated a small theoretical satellite at three altitudes. The standard deviation of in-track position error is higher at lower altitudes and grows with increasing solar and geomagnetic activity. $F_{10.7}$ was found to have a greater impact on the propagation than A_P.

Spatial variation of TMD accounts for several physical phenomena. The vertical variation is approximated by the exponential decay from hydrostatic equilibrium with an uncertainty estimated to be around 3.5% at 400 km in geomagnetic calm periods, that may be highly underestimated in geomagnetic storms (He et al., 2018). The International Standard Atmosphere (ISA; ISO, 1975) model is based on this formula, which is more accurate at lower altitudes. The horizontal variation is caused by several factors, such as global atmospheric circulation, variation in the Earth gravity field due to tides, Sun-Earth distance, Joule heating, solar flux, or solar wind. Latitudinal and longitudinal variations are usually coupled, as with the Equatorial Mass Density Anomaly (EMA): a two-cell structure with two crests around geomagnetic latitude of 25° to 30° and a dip at the geomagnetic equator (He et al., 2018). Furthermore, the spatial distribution of the TMD varies with diurnal, semi-diurnal, and higher harmonic terms of the motion of the Sun and the corresponding heating of the atmosphere, as the PCA performed by Mehta and Linares (2017) suggests.

Existing models of the upper atmosphere can be categorized into three groups: parametric models, physics-based models, and semi-empirical models. Parametric models, such as ISA or the Harries-Priester model (Montenbruck and Gill, 2005, subsection 3.5.2), design an analytic function of the density that is explicitly based on physical parameters such as the altitude. Physics-based models, such as the Global Ionosphere-Thermosphere Model (GITM; Ridley et al., 2006), and the Thermosphere-Ionosphere-Electrodynamics General Circulation Model (TIE-GCM; Qian et al., 2014), solve the full continuity, momentum, and energy Navier-Stokes equations for either neutral or charged particles in a three-dimensional grid. The difference between both models lies in using different advection equations: TIE-GCM assumes hydrostatic equilibrium, while GITM solves for a non-hydrostatic thermosphere, and GITM also includes the divergence of all velocity terms. The last group is semi-empirical models, such as the NRLMSISE-00, its updated version NRLMSIS 2.0 (Emmert et al., 2021), the Drag Temperature Model 2013 (DTM2013; Bruinsma, 2015), updated by the DTM2020 (Bruinsma and Boniface, 2021), or Jacchia-Bowman 2008 model (JB08; Bowman et al., 2008a). These models are based on equations of thermal and diffusive equilibrium on the atmosphere, that are afterwards fitted in the least squares sense to large datasets which give more accurate measurements of atmospheric density. NRLMSISE-00 uses the solar indices $F_{10.7}$ and A_P as proxies of the solar flux and geomagnetic activity, respectively. JB08 uses a different set of solar indices ($F_{10.7}$, S_{10}, M_{10} and Y_{10}) more representative of real solar activity, an improved description of semi-annual density variation, and the geomagnetic index model D_{st}. Bowman et al. (2008a) found that the JB08 represents more closely High Accuracy Satellite Drag Model (HASDM; Storz et al., 2005) derived density, especially during geomagnetic storms. DTM2013 uses F_{30} index as solar proxy, as it represents with higher fidelity the solar flux than $F_{10.7}$, and K_m or K_p instead of A_P.

All models overestimate Ultra-Violet (UV) flux during solar minima, while DTM2013 and JB08 are more precise compared to the observations of the satellites that were part of the construction of the model (Bruinsma, 2015). In the case of DTM2013, the augmented precision can be related to using an internally consistent scale: there is neither a consensus nor a standard on the C_D and BC used to derive the final density (Bruinsma et al., 2018; He et al., 2018). Difference within the models cause a bias related to the satellite model used, which can vary both in geometric shape differences and gas-

surface interaction. Furthermore, all models should be compared using an unbiased metric. Bruinsma et al. (2018, 2021) have proposed to use the mean and the standard deviation of the ratio between the observed and computed densities in a logarithmic scale. NRLMSISE-00 has been updated recently to accurately describe the atmospheric region between 70 km and 200 km in the model NRLMSIS 2.0 (Emmert et al., 2021), although no major changes have been made in the model's upper layers of the atmosphere, and NRLMSISE-00 is still more frequently used in operational conditions. Bruinsma and Boniface (2021) have presented the DTM2020 models, with two versions: an operational one, that uses $F_{10.7}$ and K_p indices for solar and geomagnetic activity, and a research model that is more accurate and uses the indices F_{30} and H_{po}. Furthermore, it includes densities from all the sources used in DTM2013, as well as Swarm constellation densities. Nevertheless, not any of the models presents a clear advantage over the others in a generic configuration (as in not limited to particular orbits): DTM2013 and JB08 are usually more accurate, but they require solar indices that are not available in a near real-time operational set-up (He et al., 2018; Pardini et al., 2012; Vallado and Finkleman, 2014).

Current trends to reduce uncertainty in the drag atmospheric modelling include calibrating these models with new and more accurate satellite observations, which are still very sparse (Bruinsma and Boniface, 2021; Matsuo et al., 2012). The broad database of Two-Line Elements (TLE) has been used to calibrate TMD semi-empirical models (Doornbos et al., 2008; Gondelach and Linares, 2020; Pardini et al., 2012). Radar and GPS density measurements have also been used to calibrate empirical models (Doornbos et al., 2007; Forootan et al., 2020; Gondelach and Linares, 2021; Zeitler et al., 2021). Artificial Neural Networks (ANN) have been suggested as a method to include density observations into a model to improve its accuracy and prediction capabilities (Licata et al., 2022; Pérez et al., 2014). Kalman filters' have been used to assimilate atmospheric data into physics-based model GITM (Kim et al., 2008; Morozov et al., 2013).

Recently, Global Navigation Satellite Systems (GNSS) of Swarm allow obtaining very precise measurements of density along its orbit (van den IJssel et al., 2020; Visser et al., 2013). Swarm mission was launched on 22 November 2013 by the European Space Agency (ESA) with the main goal of measuring the Earth's magnetic field and how it interacts with the Earth (Friis-Christensen et al., 2008). Swarm constellation is formed of three satellites: Swarm B flies at an altitude of 510 km, while the other two identical satellites fly side-by-side at a lower initial altitude of 480 km. Van den IJssel et al. (2020) proposed an improved processing method based on GNSS tracking observations, a very precise geometrical satellite model, and a realistic aerodynamic model. The method outputs density in 24 h files sampled in 30 s with a resolution of 20 min along the orbit. The model was validated with a statistical comparison with NRLMSISE-00. The comparison confirmed how the improved method augments the correlation with the model, and that NRLMSISE-00 generally over-predicts the density observations of Swarm C. The obtained densities are available as a ESA Level 2 product, and are could, in principle, be produced in near real-time (private communication, C. Siemes, 2022). Thus, as suggested by previous literature, to implement a near real-time assimilation approach of Swarm densities into NRLMSISE-00 model might improve the model accuracy and highly benefit SSA and improve orbit predictions.

Swarm TMD observations are provided with a lower latency than other missions, and the recent development in an internally consistent scale for density observations (Bruinsma et al., 2018) can provide a mechanism to test the assimilation of thermospheric density observations into density models. Although the accuracy of the different density models (He et al., 2018; Mehta and Linares, 2017) and the assimilation of density observations into atmospheric models (Doornbos et al., 2007; Forootan et al., 2020; Gondelach and Linares, 2021; Zeitler et al., 2021)have been thoroughly studied, a thorough analysis of the improvement on accuracy of orbit prediction using calibrated density models is missing.

In this report, the accuracy of numerical orbit propagation for several LEO objects is investigated under different solar activity conditions when empirical thermospheric density observations are assimilated into NRLMSISE-00 atmospheric model. Accurate dynamical modelling is needed to support space missions design and operations, as space debris and other objects in orbit pose an increasing threat to spacecraft. For example, providing more accurate trajectories could enhance SSA products, such as conjunction analysis, or space debris catalogue maintenance. The empirical density measurements assimilation into NRLMSISE-00 offers a promising approach to improving atmospheric modelling accuracy, but the effect of the dynamical environment on the accuracy of orbit prediction with assimilation is not yet well assessed. Therefore, this study seeks to address this gap in knowledge by conducting numerical simulations of LEO orbits under different solar activity conditions. The accuracy

of the resulting propagation is compared with precise orbits of the satellites GRACE-FO 1, Swarm C, and Sentinel 1-A. The latter three are well-tracked LEO objects, with known attitude and manoeuvres, at different altitudes. Furthermore, only Swarm C density was assimilated to the improved density model. By doing so, we aim to provide insights into the potential benefits and limitations of assimilating empirical density measurements into atmospheric models and inform the development of improved modelling techniques for future research.

1.1. Research questions

The following research question will be addressed in this thesis to quantify the accuracy improvement in orbit prediction of LEO objects by assimilating thermospheric density observations of Swarm C:

How much can assimilating empirical thermospheric density observations retrieved from GNSS data into the NRLMSISE-00 atmosphere model improve the orbit prediction of LEO objects?

Based on the different solar activity and common test cases for LEO objects in SST and POD scenarios, the previous research question can be divided into the following smaller research questions:

- *How does the improvement on accuracy of orbit prediction with a calibrated model vary with different solar activity conditions?*
- *How the improvement on accuracy of orbit prediction with a calibrated model vary with altitude?*
- *Can the calibrated density model correctly predict the orbit of other objects, whose density observations are not assimilated into the model?*
- *What are the limitations of a prediction the calibrated density model?*
- *What dynamical model should be used to predict the orbit, and how does it affect the accuracy of orbit prediction with a calibrated model?*
- *How does the coupling between C_D and density affect the accuracy of orbit prediction, and to what extent can this coupling be reduced with the calibrated model?*
- *How does the calibrated density model interacts with different satellite geometries?*

Overall, this master's thesis seeks to make a significant contribution to the field of space research by applying a calibrated density model to improve the accuracy of orbit prediction of LEO objects. The research has been performed in a collaboration between the Space Exploration department of TUDelft and the SST department of GMV.

1.2. Report outline

The thesis consists of two main chapters. Chapter 2 presents the core of the work in the form of a journal paper. In Chapter 3, the extensive answers to the research questions and recommendations for future work are presented. Chapter 2 and Chapter 3 are complemented by Appendix A, where the reference frames mentioned throughout the report are explained, and by Appendix B, where the parameter selection procedure for the LSE is presented. The verification and validation approach is detailed in Appendix C, where the steps taken to validate the adopted methodology are outlined.

2

Research publication

Next, it follows a standalone document, in a research publication format, that summarices the methodology, results, and main conclusions. An earlier version of the document was published with preliminary results of this master's thesis work (Callejón Cantero et al., 2023). The main differences of the published work with respect to the following chapter can be listed as: a different dynamical model, the satellite Sentinel 1-A included as a test case, a panel model geometrical specification for each of the satellites, extended epoch options during the testing period, and an updated discussion.

Improving orbit prediction via thermospheric density calibration

M. Callejón Cantero

Faculty of Aerospace Engineering, Delft University of Technology, Kluyverweg 1, 2629HS, Delft, The Netherlands.
GMV, Isaac Newton 11, 28670, Tres Cantos, Madrid, Spain.
E-mail: miguel.callejon.cantero@gmv.com.

Abstract

The uncertainty on Thermospheric Mass Density (TMD), as derived from atmospheric models, can reach values up to 30%. This effect is noteworthy in Low Earth Orbit (LEO), where drag is the main perturbing force. Furthermore, LEO regime harbours more than 17500 objects at the end of 2021, almost 60% of tracked objects orbiting Earth, and the rate of growth raises every year. Increasing the accuracy of density models is needed to ensure sustainable satellite operations in a crowded space environment. This paper presents an assessment on the accuracy of orbit predictions up to 10 days after assimilating Swarm C thermospheric density observations into the atmospheric model NRLMSISE-00, using Principal Component Analysis (PCA) to decompose a fine grid in density into the main temporal and spatial modes. The orbit of GRACE-FO and Sentinel 1-A satellites, whose data was not assimilated, is predicted. The results obtained show that a simple Least Squares Estimation (LSE) can fit all density observations of one month, and correctly predict the density during the next month. A more realistic $\boldsymbol{C_D}$ is found with the calibrated model during January 2019, period of low solar activity. The median accuracy of a set of orbit predictions during a month is reduced during January 2019 and March 2022, period of medium solar activity, with a cannonball and a scaled panel model geometry. The best improvement is achieved during March 2022 for satellite Swarm C, as the median accuracy is reduced from $20.67\,\mathrm{km}$ with NRLMSISE-00 to $13.75\,\mathrm{km}$ with the calibrated model.

1 Introduction

Atmospheric drag is the main perturbation force acting on space objects on LEO under $1000\,\mathrm{km}$, excluding Earth's non-spherical gravity field. Despite this, the uncertainty in satellite drag modelling is large compared to other perturbing forces. The uncertainty sources on drag derive from imprecise knowledge of the object's shape and position, the wind acting on the object, due to its effect on the inertial velocity of the object, the aerodynamic coefficients of the object, either from an imperfect geometric model or an imperfect characterization of the gas-surface interaction, and the error on the TMD of the atmosphere. Several models exist that characterize the density in the upper layers of the atmosphere, but the uncertainty on the TMD computed from atmospheres models can reach values up to 30%, or even higher (He et al., 2018). The accuracy of the models can be improved by assimilating atmospheric density observations retrieved from Precise Orbit Determination (POD) ephemeris of LEO satellites. Because of this, several space applications at LEO benefit from accurate thermosphere modelling. For example, LEO mission design, re-entry trajectory design, POD, Space Situational Awareness (SSA), or collision avoidance in Space Traffic Management.

The relevance for space debris risk mitigation is especially noteworthy, as the LEO region harbours the vast majority of space objects tracked (ESA, 2022; Klinkrad, 2006).

State-of-the-art models of the upper atmosphere can be categorized into two groups: physics-based models and semi-empirical models. Physics-based models, such as the Global Ionosphere-Thermosphere Model (GITM; Ridley et al., 2006), and the Thermosphere-Ionosphere-Electrodynamics General Circulation Model (TIE-GCM; Qian et al., 2014), solve the full Navier-Stokes equations for either neutral or charged particles in a three-dimensional grid. On the other hand, semi-empirical models, such as the US-Naval Research Laboratory Mass Spectrometer and Incoherent Scatter-radar Exosphere model - 2000 version (NRLMSISE-00; Picone et al., 2002), the Drag Temperature Model 2013 (DTM2013; Bruinsma, 2015), or Jacchia-Bowman 2008 model (JB08; Bowman et al., 2008), are based on equations of thermal and diffusive equilibrium on the atmosphere, and fitted in the least squares sense to large datasets which give more accurate measurements of atmospheric density. NRLMSISE-00 uses the solar indices $F_{10.7}$ and A_P as proxies of the solar flux and geomagnetic activity, respectively. JB08 and DTM2013 models use a different set of indices. Each model was tuned assimilating data from different sources such as Jacchia orbital drag, CHAMP, GRACE, and GOCE accelerometer-derived satellites. Nevertheless, none of these models presents a clear advantage over the others in a generic configuration (as in not limited to particular orbits): DTM2013 and JB08 are usually more accurate, but they require solar indices that are not available in a near real-time operational set-up (He et al., 2018; Pardini et al., 2012; Vallado & Finkleman, 2014).

Current trends to reduce uncertainty in the atmospheric drag modelling include calibrating these models with new and more accurate satellite observations, which are still very sparse (Bruinsma & Boniface, 2021; Matsuo et al., 2012). The broad database of Two-Line Elements (TLE) has been used to calibrate TMD semi-empirical models and improve the Root Mean Square (RMS) density model error from 30% to 15% (Doornbos et al., 2008). Some studies employed the TLE of decaying satellites to compare the bias of semi-empirical models Pardini et al. (2012). More recently, Unscented Kalman Filter (UKF) was used to assimilate TLE data in near real-time into a dynamical Reduced-Order Model of NRLMSISE-00, JB08, and TIE-GCM models (Gondelach & Linares, 2020). The accuracy in density was in general improved. Along the CHAMP orbit, whose TLE data was included in the model, the RMS of density error improved from 26.7% to 7.7%. However, it was also concluded that assimilating precise density data instead of carefully chosen TLE elements might improve the model.

Radar and GPS density measurements have also been used to calibrate empirical models (Doornbos et al., 2007; Gondelach & Linares, 2021; Zeitler et al., 2021). Artificial Neural Networks have been suggested as a method to include density observations into a model to improve its accuracy and prediction capabilities (Licata et al., 2022; Pérez et al., 2014). A predictor localized on certain orbits was proposed by Pérez et al. (2014), while a model based on High Accuracy Satellite Drag Model (Storz et al., 2005) dataset with an average error of 10.69% was generated by Licata et al. (2022). Kalman filters have been used to assimilate atmospheric data into the physics-based model GITM (Kim et al., 2008; Morozov et al., 2013). While a UKF was used in Kim et al. (2008) to assimilate atmospheric composition data into the model in localized parts of the grid, CHAMP density measurements were assimilated by Morozov et al. (2013) using an Ensemble Kalman Filter (EnKF), reducing its bias. Fitting the semi-empirical models' output density to a linear regression has also been proposed (Bowden, 2022) to afterwards assimilate, using a Kalman filter, Swarm C and GOCE satellite measurements into a state composed of the linear regression coefficients.

CHAMP and GRACE accelerometer-derived measurements have been assimilated (Forootan et al., 2020) using an EnKF and an Ensemble Square-Root Kalman Filter that modifies, at each analysis step, a set of density estimations and the four NRLMSISE-00 parameters that influenced the most the model after a sensitivity analysis: $F_{10.7}$, a_P, and two internal model coefficients that affect the upper exospheric temperature T_{ex}: `ptm[0]` and `pt[0]` (Forootan et al., 2020). The model was tuned to the TMD estimates during the entire year of 2003, and a reduction of 27% reduction of the RMS between the model and observations was achieved. Forootan et al. (2020) discussed how their method can be further extended, and implemented operationally, using GRACE and Swarm measurements.

Recently, Global Navigation Satellite Systems (GNSS) and accelerometer measurements of Swarm

allow obtaining very precise measurements of density along its orbit (van den IJssel et al., 2020; Visser, Doornbos, van den IJssel, & Teixeira da Encarnação, 2013). The obtained densities are available as a European Space Agency (ESA) Level 2 product, and could be produced in near real-time in the future (private communication, C. Siemes, 2022). Thus, as suggested by previous literature, implementing a near real-time assimilation approach of Swarm densities into NRLMSISE-00 model might improve the model accuracy and highly benefit SSA and space debris risk mitigation.

The novelty of this work consist on assessing the capabilities of assimilating density data into NRLMSISE-00 model with two objectives: 1) predicting the density at future epochs, and 2) assessing the possible benefits of propagating a typical scenario using the calibrated model over a period from one week up to one month. First, a first step in assimilating Swarm densities into NRLMSISE-00 model is taken. NRLMSISE-00 has been decomposed in its main components using PCA (Forootan et al., 2019; Mehta & Linares, 2017). For that, a grid of NRLMSISE-00 has been created in longitude, latitude, and time. Second, each principal component has been calibrated using LSE procedure with Swarm C density observations. The model has been validated with training data by analysing the residuals of the fit, and its prediction capabilities have been tested. Finally, the calibrated density model has been tested in several scenarios, comparing the propagation of three precisely known objects: satellites Swarm C, GRACE-FO 1, and Sentinel 1-A. Present work is divided into three sections: in section 2, the particularities of each method are explained, in section 3, the calibration, prediction, and propagation output are analysed, and finally, in section 4, the conclusions and future work are laid out.

2 Methodology

The methodology employed in this study involves using LSE to fit NRLMSISE-00 model to the atmospheric density observations of the Swarm C satellite. LSE method is a commonly used technique for fitting a mathematical model to a set of observations and is chosen for its simplicity and robustness. This section is divided into two subsections: subsection 2.1, which describes the procedure for calibrating and predicting the NRLMSISE-00 model using LSE and subsection 2.2, which outlines the design of test cases to evaluate the accuracy of the calibrated model.

2.1 Density calibration and prediction

The NRLMSISE-00 model has been sampled using PCA in longitude, latitude and time. This approach involves analysing the data to identify patterns and variations in the atmospheric density at different locations and times. PCA allows identifying the main directions of variation in both the spatial and temporal domains. Spatial discretization was on a grid with 80 points in longitude and 40 points in latitude. The time grid collected a sample every 10 minutes for one month. The time discretization was the same as in literature (Forootan et al., 2020). This grid size and sampling frequency provide a high-resolution representation of the atmospheric density at different locations and times in a matrix $\mathbf{X}_{grid}$ of size 4464×3200, allowing for a detailed analysis of the patterns and variations in the data.

Using a high-resolution grid and a fine time sampling allows capturing the small-scale variations in the atmosphere, which can be useful for different applications. Additionally, the one-month coverage allows considering up to semi-monthly period variations in the atmosphere. This sampling strategy ensures that the model is representative of the Earth's atmosphere under certain conditions (a particular level of solar heating, altitude close to that of Swarm C orbit) and provides a detailed understanding of the atmospheric density at different locations and times. Coarser resolution grids have been tested in the calibration process, but the results were not as accurate as the 80x40 grid used. While the resolution can be further enhanced, the accuracy of the model is already sufficient and an increase in computation time would be unnecessarily incurred.

Regarding altitude discretization, there are several options. It is possible to add a third dimension to the spatial grid, by making the grid coarser, as in the work of Mehta and Linares (2017). However, it is also possible to use the vertical variation profile as in the NRLMSISE-00 model (Forootan et al., 2020; Picone et al., 2002). Although this hypothesis might add non-negligible differences during geomagnetic storms (He et al., 2018), the added error is assumed to be far below the model error during the present work. The vertical variation profile can be computed as:

$$\rho_h = \rho_{400} \frac{\rho_{M,h}}{\rho_{M,400}}, \tag{1}$$

where subscript M represents NRLMSISE-00 model, and 400 represents density at altitude of $400\,\mathrm{km}$. Therefore, NRLMSISE-00 grid is created at an altitude of $400\,\mathrm{km}$, and density at any other height is computed with Equation 1.

The input of NRLMSISE-00 was chosen according to the recommendations in the literature (Picone et al., 2002; Vallado & Finkleman, 2014). This involved using actual observed values for $F_{10.7}$ and a_P indices instead of predicted ones. This allows for a more accurate representation of the current atmospheric conditions. Additionally, 3-hourly a_P indices were used, which capture the small-time-scale variations in the atmosphere better than the one-day A_P index. Furthermore, the $F_{10.7}$ values were adjusted to exactly $1\,\mathrm{AU}$, as recommended by Vallado and Finkleman (2014). The use of observed values for indices, 3-hourly a_P and adjusted $F_{10.7}$ values have been found to improve the model's accuracy (Vallado & Finkleman, 2014).

PCA is a technique used to analyse and reduce the dimensionality of a dataset, it is often used in the context of atmospheric density data. $\mathbf{X}_{grid}$, a matrix that contains time observations along rows and spatial observations along columns, is decomposed in its main components, such that:

$$\mathbf{X}_{grid} = \bar{\mathbf{X}} + \mathbf{U} \cdot \mathbf{S} \cdot \mathbf{V}^T = \bar{\mathbf{X}} + \mathbf{P} \cdot \mathbf{E} \tag{2}$$

In Equation 2, time variation t of the components is retained in matrix $\mathbf{P} = \mathbf{U} \cdot \mathbf{S}$, while space matrix $\mathbf{E} = \mathbf{V}^T$ retains information about the spatial grid $\mathbf{s}$. Matrix $\bar{\mathbf{X}}$ contains the mean spatial value of each component, and $\mathbf{U}$, $\mathbf{S}$, and $\mathbf{V}^T$ matrices are the output of Singular Value Decomposition (Wall et al., 2003) factorization, the core of PCA algorithm. The components are sorted in descending order of their variance. The first component has the highest variance, and each subsequent component has a lower variance. This is because, by sorting by eigenvalues, the directions (components) in the data that have the most significant variance (or information) are found, and the data is projected onto these directions. By sorting the components in this way, the first few components will account for the majority of the variation in the data, and the remaining components will account for less and less variance.

The amount of information that is retained using PCA can be measured with the normalized eigenvalues, i.e., each component of matrix $\mathbf{S}$ divided by the summation of all the eigenvalues in a PCA with all possible components (in this case, 3200, the spatial grid size). The data can be represented in fewer dimensions without losing information: with 10 components, 92.89% of the information is retained; with 15 components, 96.53%, and with 20 components, 98.08%. Previous numbers were computed using the method from Mehta and Linares (2017) For a comprehensive overview of PCA, the reader is directed to the work by Forootan et al. (2019); Wall et al. (2003), or (Forootan et al., 2020).

PCA matrices of atmospheric density are generated using the NRLMSISE-00 model. However, it is acknowledged that models can be subject to errors and biases. To enhance the accuracy of NRLMSISE-00, a calibration process has been implemented using the LSE algorithm in conjunction with observations of the Swarm C satellite. The Swarm satellite mission provides highly precise observations of the atmosphere, which are considered to be state-of-the-art in terms of atmospheric density knowledge. These observations have been extensively used as ground-truth data in various studies (Bowden, 2022; Bruinsma & Boniface, 2021) and are readily available to the public.

The calibration has been performed using LSE (Montenbruck & Gill, 2005) to estimate the parameters $\mathbf{y} = [\mathbf{y}_{PCA}, y_{mean}]$, where $\mathbf{y}_{PCA}$ is a vector containing scale factors of the PCA components, and y_{mean} is the scale factor for the mean (Forootan et al., 2020, section 2.3.2):

$$\mathbf{X}_{calibr} = y_{mean}\bar{\mathbf{X}} + \mathbf{P} \cdot \mathrm{diag}(\mathbf{y}_{PCA}) \cdot \mathbf{E} \tag{3}$$

Previous equation is linear with respect to the estimated parameters, and thus it is with a linear LSE, as by (Forootan et al., 2020). Linear LSE method Montenbruck and Gill (2005) can be mathematically represented with the measurement function:

$$\mathbf{z} = \mathbf{H}\mathbf{y} \tag{4}$$

where $\mathbf{H} = \dfrac{\partial \mathbf{h}(t, \mathbf{y})}{\partial \mathbf{y}}$ is the Jacobian of the measurement function $\mathbf{h} = \hat{\mathbf{z}} = \hat{\mathbf{x}}$, $\mathbf{x}$ is the state, in this case, the logarithm of the density $\mathbf{x} = \ln \boldsymbol{\rho}$, $\mathbf{z}$ are the measurements, and $\hat{\mathbf{x}}$ and $\hat{\mathbf{z}}$ are the computed state and measurement, respectively. When the linear

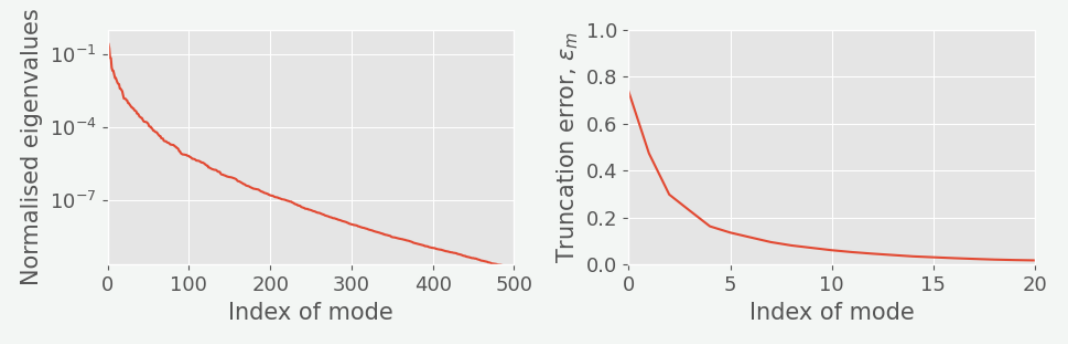

Fig. 1: Normalized eigenvalues of X_{grid} and truncation error in the 10 first components.

system is solved, the diagonal matrix of measurement weights $\mathbf{W}$ is introduced:

$$\mathbf{H}^T\mathbf{W}\mathbf{z} = \mathbf{H}^T\mathbf{W}\mathbf{H}\mathbf{y} \tag{5}$$

Matrix $\mathbf{W}$ has used values of the standard deviation of the residuals $\Delta\mathbf{z}$. The residuals to minimize are $\Delta\mathbf{z} = \hat{\mathbf{z}} - \mathbf{z}$. This linearization procedure has obtained the same results as the direct method from Forootan et al. (2020). The matrix $\mathbf{P} = \left(\mathbf{H}^T\mathbf{W}\mathbf{H}\right)^{-1}$ denotes the covariance matrix of the parameters, a measurement of the sensitivity of the parameters.

Matrix $\mathbf{H}$ is computed from Equation 3. In order to provide a dense grid over the observations $\mathbf{z}$, the density computed with Equation 3 is interpolated. Two interpolators have been compared: a Radial Basis Functions (RBF) interpolator, and a grid interpolator based on the Clough Toucher interpolation (CT) algorithm. Both are available in the open-source library SciPy (Virtanen et al., 2020). Both RBF and CT have shown to effectively interpolate within acceptable error margins: RBF has a $4.06 \cdot 10^{-5}$ relative error, and CT $7.74 \cdot 10^{-5}$. For the prediction and calibration of the density, RBF has been used. However, for the orbital propagation, a simple bi-dimensional method has been created based on one-dimensional Lagrange interpolators. The method first interpolates on one dimension and solves N points. Afterwards, it interpolates along the second dimension using as nodal points the N points previously computed. Both interpolators add an associated error below the expected intrinsic error of the density model.

This calibration process is expected to significantly improve the precision of the NRLMSISE-00 model. To provide a dense grid over the period that is being calibrated, matrices $\bar{\mathbf{X}}$, $\mathbf{P}$, and $\mathbf{E}$ are interpolated at a certain point in time and space (longitude and latitude).

Finally, the calibration has been tested for predicting atmospheric densities during the period following the calibration. It has been assumed that all the inputs of NRLMSISE-00 are available during the close future (i.e., all indices are available, and the error due to a predicted solar index is not taken into account). Thus, matrices $\bar{\mathbf{X}}$, $\mathbf{P}$, and $\mathbf{E}$ are available in the future, and parameters $\mathbf{y}$ are calibrated with the preceding month. The residuals of the prediction are analysed in section 3.

2.2 Orbital propagation with calibrated model

The calibrated model has afterwards been tested in the propagation of a LEO satellite to assess and quantify the advantages of the calibration with satellite TMD observations. In a near real-time scenario, a calibrated model might be able to present benefits in terms of better characterization of an orbit. Two periods have been tested: one with very low solar activity, January 2019, and one with mild solar activity, March 2022. The calibrated model has been tested with three satellites: Swarm C, GRACE-FO 1, and Sentinel 1-A. Swarm C is expected to be the best-case scenario because its density observations have been assimilated. On the other hand, GRACE-FO 1 and Sentinel 1-A are realistic test cases for operational satellites with a stable, well-controlled attitude, and well known satellite geometry. Also, the POD ephemeris is known for the three satellites. However, there are differences between both satellites' altitude and local-solar time, due to the different orbit: Swarm C flies at an approximate altitude of $480\,\mathrm{km}$,

while GRACE-FO 1 at $500\,\mathrm{km}$. Sentinel 1-A flies at a higher altitude $693\,\mathrm{km}$, where the drag force is lower due to the diminishing atmosphere.

The orbital propagation has two steps. First, an orbital fit is performed during a short period (3 days). The fit is a LSE process in which the initial position, velocity, drag coefficient C_D and radiation coefficient C_R of the satellite, which minimizes the residuals with respect to a POD orbit, are found. In the second step, the orbit is propagated using the initial state obtained with the fit. The objective of the fit is to minimize any discrepancies in the dynamical model used to obtain POD orbit and one used when propagating so that the effect of the dynamical model which was used to retrieve POD observations is minimized.

As the results are not consistent depending on the epoch, the following bootstrapping strategy has been followed: to fit the orbit during 3 days, and afterwards propagated for 10 days, in a moving 13-day window, starting on the 1^{st} of the month, up to the 18^{th}, resulting in 19 windows. As there is not enough time between manoeuvres for Sentinel 1-A, this test has only been performed for GRACE-FO 1 and Swarm C.

The dynamical model for the orbit prediction consist of the following contributions: spherical harmonics with degree and order 200, solid tides, drag force, Solar Radiation Pressure (SRP), and third body effects of the Sun, the Moon, and J2 harmonic of the Moon as perturbations. More spherical terms are included than the Space Surveillance and Tracking (SST) configuration for a typical LEO orbit, 64x64. The C_D which is the output of the previous fit will compensate partially the calibration performed in the density, as drag is described by Equation 6 and the acceleration shall be the same to fit the dynamical model to the observations. However, using a detailed dynamical model might enhance the accuracy of an orbit prediction with the calibrated model.

$$\mathbf{a}_d = \frac{1}{2} C_D \frac{A}{m_S} \rho v^2 \mathbf{n}_d \tag{6}$$

In previous equation, $\mathbf{a}_d$ is the drag acceleration acting on the satellite, A is the area of the satellite exposed to drag, m_S is the mass of the satellite, ρ is the density of the atmosphere, v is the velocity of the satellite with respect to wind, and $\mathbf{n}_drag$ is the unit vector in the direction of wind. A panel model has also been implemented for the three satellites following the geometrical specifications in literature for Swarm C (Siemes, 2019), GRACE-FO 1 (Wen et al., 2019), and Sentinel 1-A (GMV, 2019). The aerodynamic and radiation force coefficients for a one-sided panel have been computed using the description of Sentman's equations given by Doornbos (2011); March et al. (2019). An energy accommodation coefficient of 0.85 has been assumed for all test cases. The attitude of the spacecraft is described by quaternions to the spacecraft body frame that are publicly available as ESA or NASA JPL Level 1b data products. In the case of Sentinel 1-A (ESA, 2023), and GRACE-FO 1 (Wen et al., 2019), the quaternions define a rotation from an inertial frame. In the case of Swarm C (ESA, 2014), the rotation is from an earth-centered frame.

A summary of the design choices is presented in Table 1, and Figure 2 shows the top-level architectural design for the calibration.

Table 1: Summary of the design choices and test cases.

Longitude grid	80 (0°, 360°)		
Latitude grid	40 (−90°, 90°)		
Time grid	144 · 31 (1 month)		
PCA	10 components		
Interpolation	RBF for calibration Lagrange for propagation		
Dynamical model	Spherical harmonics 200x200: EIGEN-GRGS.RL04.MEAN-FIELD model Solid tides Third body: Moon, Sun, J2-Moon Cannonball SRP Drag force		
	Case 1	Case 2	
Training period	Jan. 2019	Mar. 2022	
Predicting period	Feb. 2019	Apr. 2022	
Satellites	GRACE-FO 1	Swarm C	Sentinel 1-A

3 Results

In this section, the findings of the present study on calibrating NRLMSISE-00 to TMD observations are presented. The analysis is divided into three main subsections, each focusing on a specific aspect of the study. In the first subsection, we discuss the main modes of the PCA, its physical meaning and its temporal variation. In the second subsection, we present the results of the density calibration and prediction, including the methods and metrics used to evaluate the accuracy of the predictions. Finally, in the third subsection, we detail the results of the orbital propagation with the calibrated, and how it was used to improve the accuracy of the predictions.

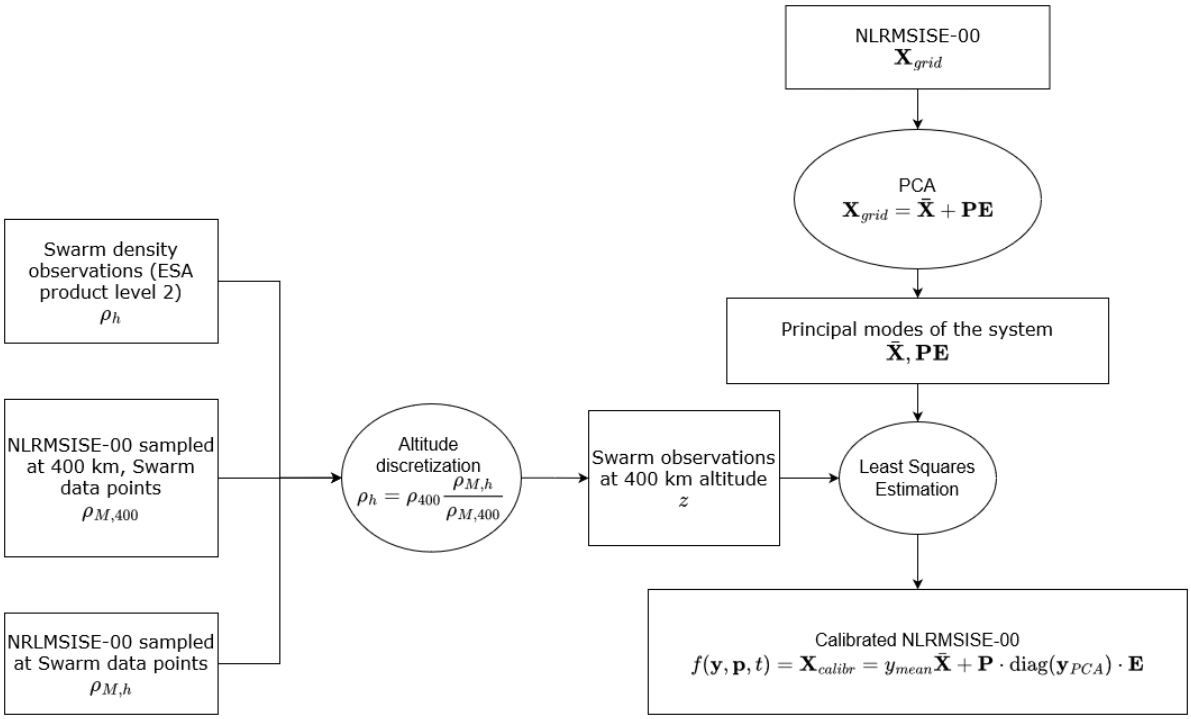

Fig. 2: Top level flow-chart of the calibration process.

3.1 Principal Component Analysis

In this subsection, the results of the PCA and its application to the dataset are presented. PCA was performed on the dataset with 10 components, which were chosen as it retains 92.89% of the energy of the system (see Figure 1). Increasing the number of modes was found to correspond with a negligible increase in accuracy, both in the calibration and the orbit propagation. Figure 3 shows the shape of the spatial modes obtained, very similar to the modes found in literature (Mehta & Linares, 2017). However, there are several differences. First, a coverage of one month in this analysis, as opposed to only one day. Second, to create Figure 3, observed a_P and $F_{10.7}$ indices have been used. Third, the use of a bi-dimensional spatial grid, and scaling altitude with Equation 1, instead of creating a coarser grid in three dimensions.

Each of the 10 components extracted from the PCA has a physical meaning associated with features of the atmosphere. For example, modes 1 and 2 correspond to the diurnal migrating solar tide, and modes 4 and 5 correspond to the semi-diurnal migrating solar tide (see Figure 3). Modes 3, 6, and 9 correspond to a slower variation, and modes 3 and 6 seem to be in phase opposition, according to the pattern in Figure 3. These results indicate that the PCA correctly captures the relevant patterns and relationships over the sampling period. These slower varying modes do not appear in the work by Mehta and Linares (2017), due to the brief sampling period.

3.2 Density calibration and prediction

In this subsection, the results of the LSE used for the density model calibration are described, including the residuals, covariance and correlation analysis. The calibrated density values are presented, and their precision is evaluated through comparison with Swarm C density data. The ability of the model to predict density values at unobserved locations and altitudes based on the calibrated density values is demonstrated. In the first step, residuals have been scaled with the standard deviation of the observations $\sigma_{observations}$. During calibration, this parameter was chosen to ensure that the weighted RMS is exactly 1. The mean and standard deviation obtained with this scaling parameter are 0 and 1, respectively.

Furthermore, the calibrated model should be compared using a consistent metric. An example consistent metric is the mean and the standard

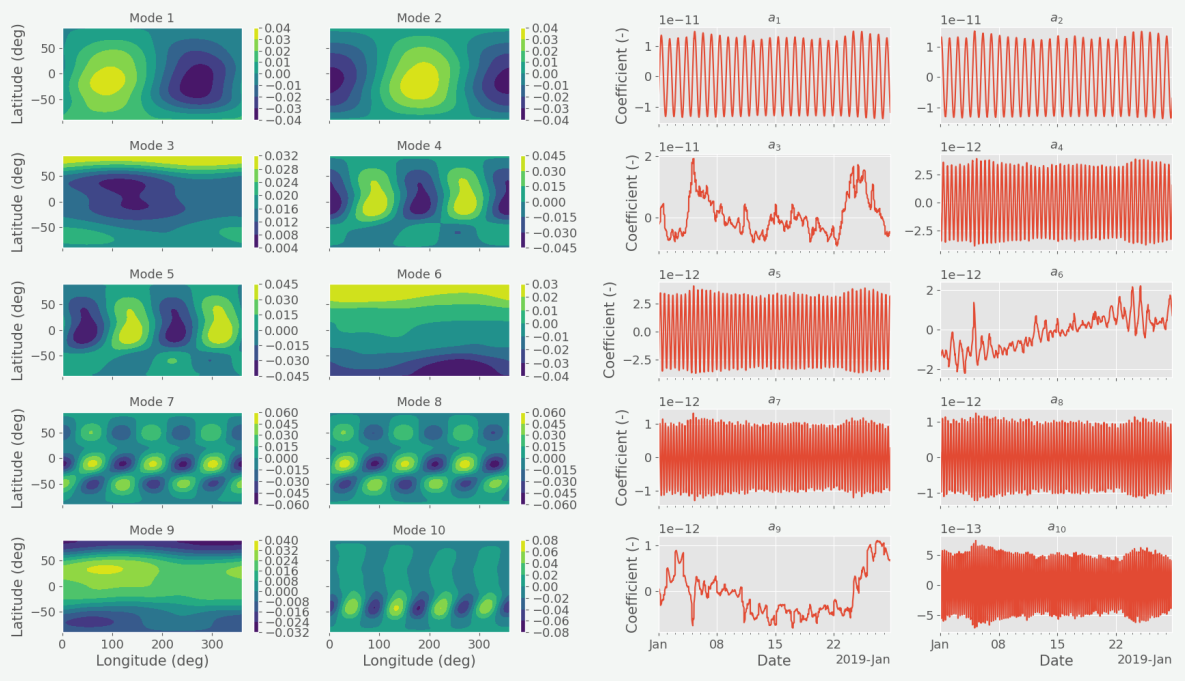

Fig. 3: Spatial and temporal evolution of the 10 principal components or modes of NRLMSISE-00 during January 2019. Shape of the modes in adimensional units, and temporal evolution in $\mathrm{kg\,m^{-1}}$

deviation of the ratio between the observed and computed densities in a logarithmic scale (Bruinsma et al., 2021, 2018). The main metrics used to compute the residuals and evaluate the fit are the ones described by Bruinsma et al. (2018):

$$\mu = \exp\left(\text{mean}\left(\ln\left(\frac{\rho_{observations}}{\rho_{model}}\right)\right)\right) \tag{7}$$

$$\sigma = \exp\left(\text{std}\left(\ln\left(\frac{\rho_{observations}}{\rho_{model}}\right)\right) - 1\right) \cdot 100 \tag{8}$$

These metrics take into account both the magnitude and spread of the residuals and have been argued as a fair assessment metric (Bruinsma et al., 2018). The residuals are defined as:

$$\Delta z = \ln\left(\frac{\rho_{observations}}{\rho_{model}}\right) \tag{9}$$

Table 2 shows the mean and standard deviation from Equation 7 and Equation 8 for all cases. This metric shows that the calibrated model mirrors the residuals for almost all cases. The calibrated model has been tested with respect to the observations that

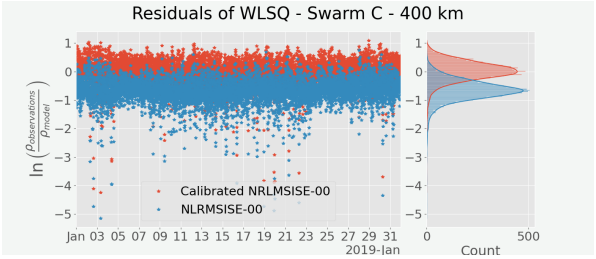

Fig. 4: Relative residuals during January 2019.

Table 2: Mean and standard deviation for both cases, computed using Equation 7 and Equation 8.

	Case 1		Case 2	
	μ	σ	μ	σ
	Calibration			
NRLMSISE-00	0.51	51.16%	0.81	15.19%
Calibrated	1.00	47.19%	1.00	13.53%
	Prediction			
NRLMSISE-00	0.58	35.70%	0.83	22.70%
Calibrated	1.04	34.14%	1.00	25.60%

were fitted into the model, Swarm C. Comparing the calibrated model with the observations of other satellites, such as GRACE or GOCE, would

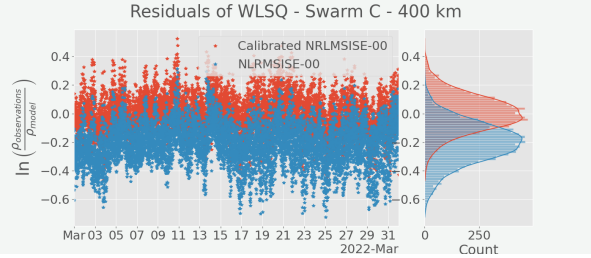

Fig. 5: Relative residuals during March 2022.

be possible. Nevertheless, this work focus is on the accuracy gain from orbit prediction from this calibration.

Figure 4 shows the logarithm of the ratio of the residuals for January 2019. For this case, the standard deviation has been slightly reduced during the calibration too: from 51.16% to 47.19%. During the medium solar activity (March 2022), NRLMSISE-00 is closer to Swarm C density observations, as the mean closer to the unit, 0.81 with respect to 0.51, and lower standard deviation, 15.19% with respect to 51.16% in Table 2 and Figure 5 show. Furthermore, the calibrated model fits the observations with a mean of one and reduces the standard deviation.

Calibration of the model has been performed using the logarithm of Swarm C GNSS-derived density observations as measurements. When the model is calibrated on the density (as opposed to the logarithm of the density), the calibration performed slightly worse: a mean of 0.9681 was obtained on the ratio and a standard deviation of 49.95%. As the logarithm of the density is represented by a normal distribution, it was expected that the calibration on the logarithm would have better results.

The correlation matrix of the estimation process and the parameter values normalized by their standard deviation are shown in Figure 6. For every parameter but parameters 5 and 9, which correspond to modes 6 and 10, the parameter value is at least one order of magnitude higher than the estimated variance, which provides confidence in the estimated parameters. Furthermore, the correlation matrix shows a very low inverse relationship between parameters 0 and 1, 3 and 4, and a weak direct correlation between parameters 6 and 7, and 0, 1, 6, and 7. The inverse relationship can be explained as the parameters are opposite in phase, as it can be seen in Figure 3, so the LSE keeps the physical properties of the method. Figure 6 shows a direct correlation around 30% between parameters 0, 1, 6, and 7, which are modes with a frequency of $24\,\mathrm{h}$ and $8\,\mathrm{h}$. The calibration was also performed using coarser grids in time, obtaining worse calibration and correlation output.

It is of interest to predict the density values during the following time interval while using prior calibration $\mathbf{y}$. To do so, PCA is performed again on NRLMSISE-00, and matrices $\bar{\mathbf{X}}$, $\mathbf{E}$, and $\mathbf{P}$ have been computed in February 2019 and April 2022. It is assumed that all solar indices and other NRLMSISE-00 inputs are available, i.e., observed $F_{10.7}$ and a_P indices have been used instead of predicted ones. However, no density observations have been used during the propagation, and parameters $\mathbf{y}$ are the output of prior calibration. As the residuals show in Figure 7, the model is fitted to Swarm C observations with a mean value of almost one, and the standard deviation is reduced. The standard deviation is lower for the residuals in February 2019 than for the residuals in January 2019, due to NRLMSISE-00 being closer to the residuals during the testing data. Density has also been predicted during April 2022, and similar results can be observed for the medium solar activity case in Figure 8: the calibrated model is fitted to Swarm C observations using data from March 2022, and the mean of the density ratio is close to one in April 2022. However, the standard deviation increases for the calibrated model. This might be due to the particular pattern, i.e., the sinusoidal variation with a monthly period shown by the ratio of Swarm C observation and the NRLMSISE-00 model during April 2022.

3.3 Orbital propagation with calibrated NRLMSISE-00

This subsection deals with the propagation of an orbit after it has been fitted to POD observations. The fitting process, which adjusts initial orbital parameters to better match observed data, is a crucial step in orbit determination. Its only purpose is to obtain an initial state vector which is compatible with the underlying dynamical model. Propagating these orbits allows for a better understanding of their behaviour and potential deviations from the fitted parameters. The test orbits examined in this subsection include three satellites: GRACE-FO 1, Swarm C, and Sentinel 1-A.

In this study, the choice of dynamical model used for the propagation of the orbits was a crucial step. As previously mentioned in subsection 2.2, a dynamical model with spherical harmonics of degree and order 200 has been used to simulate the orbits of the three

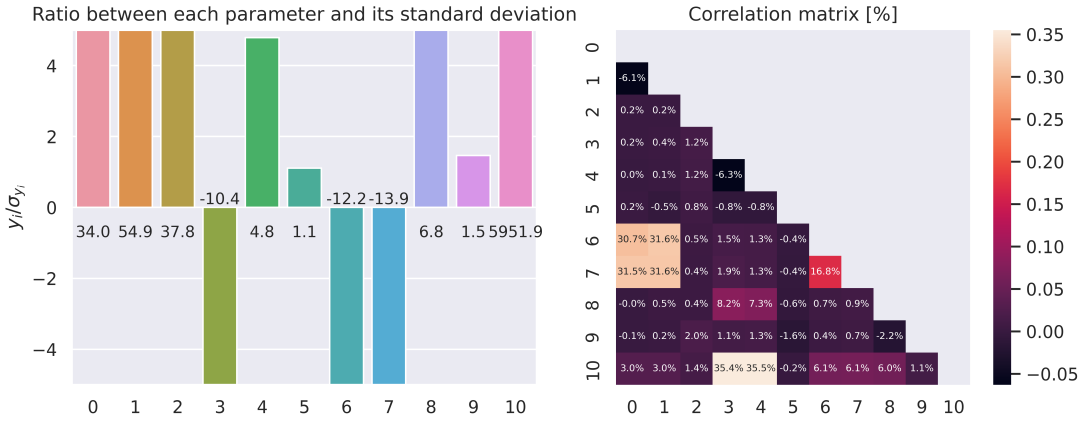

Fig. 6: Left: ratios of the estimated parameters and their standard deviation, indicating the parameters' significance. Right: correlation matrix of the parameters.

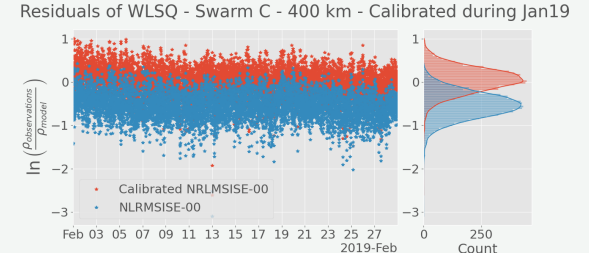

Fig. 7: Relative residuals during February 2019 calibrating during January 2019.

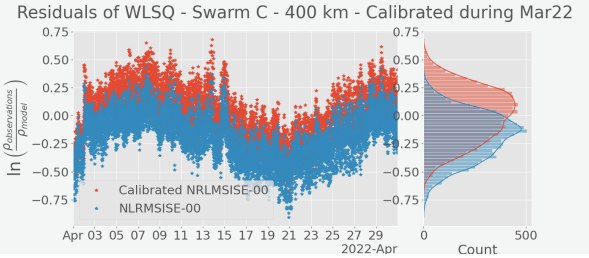

Fig. 8: Relative residuals during April 2022 calibrating during March 2022.

satellites considered in this study, with additional perturbations from solid tides, drag force, SRP, and third body effects. The typical SST dynamical model for LEO objects usually considers up to order 64 in the dynamics. Assimilation of TMD observations into a density model would require an increased computational cost for the possibility of an increase in accuracy.

Table 3: Drag and SRP coefficients and areas for the dynamical model validation.

Satellite	Case	C_D	A_D $[m^2]$	C_R	A_R $[m^2]$
Swarm C	1	1.99	0.84	0.62	7.23
	2	3.17	0.84	1.26	7.23
GRACE-FO 1	1	2.04	1.00	0.40	4.0
	2	2.91	1.00	0.65	4.0
Sentinel 1-A	1	2.79	6.35	1.20	38.0
	2	3.25	6.35	0.96	38.0

To demonstrate the effect of the dynamical model on the accuracy of the orbits, accelerations are computed for the three satellites under two solar conditions (low solar activity, January 2019, case 1; and medium solar activity, March 2022, case 2). A cannonball model is used for both the drag and SRP. The realistic values employed for the C_D and C_R are specified in Table 3, along with the corresponding areas. The realistic C_D and C_R are the result of a fit to the POD orbit, which is analysed thoroughly at the end of this subsection. Then, the orbit is predicted for a short period of time, i.e., 4 days, using the default integrator and propagator scheme. The truncation error for Swarm C, under low solar conditions (case 1), using a geopotential contribution of order 64, 128, and 200 is compared in Figure 9.

Figure 9 shows that the truncation error resulting from using spherical harmonics of degree and order 64 is of the same magnitude as other perturbations such as drag. In a usual configuration, the orbital fit would assimilate this error on the estimated parameters. However, the estimation of C_D might neglect the improvement of the density model. When

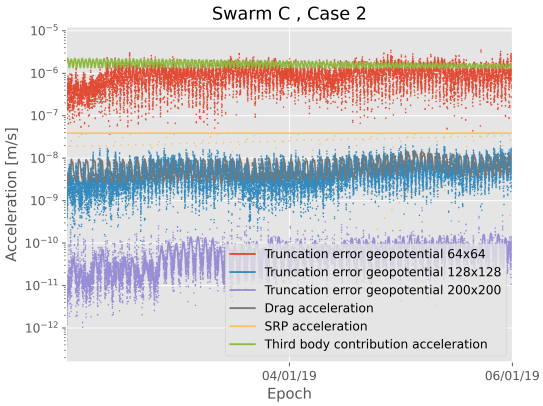

Fig. 9: Accelerations along Swarm orbit for case 1, and option (b).

using a geopotential perturbation of order 64, the drag coefficient might absorb not only perturbations caused by drag, but any truncation of the gravity field. Although the isolated contribution of the gravity field truncation propagates a non-accumulative error of $1.5\,\mathrm{m}$, and the drag contribution propagates to $40\,\mathrm{m}^2$, the combined effect of the estimation of the C_D and prediction with increased order and degree can be the reason for the calibrated density model to improve the accuracy, with the computational cost associated. However, computational efficiency is not a requirement of this work, and the perturbations need to be decoupled to analyse the accuracy improvement. The geopotential contribution has the largest contribution at the lowest altitude. Therefore, the truncation error committed diminishes for GRACE-FO 1 and Sentinel 1-A, satellites flying higher than Swarm C. Order and degree 200 is needed for Swarm C, and order 128 for satellites Sentinel 1-A and GRACE-FO-1. For consistency, order and degree 200 was chosen for the all the tests.

When using a fixed-area cannonball geometry for the satellite, the effect of the calibration of density and orbital fit can be blended. The main reason is drag acceleration being proportional to both C_D and TMD (Equation 6). Hence, estimating the C_D compensates for incorrectly scaled density, i.e., any bias on the atmospheric model. Therefore, the use of a calibrated density model is diminished when using a simple geometry. Because of that, a panel model geometry was implemented, with interpolated attitude obtained from the GRACE-FO Level-1B product release (JPL, 2019), Swarm C Level-1B data (ESA, 2014), and Sentinel 1-A (ESA, 2023). The drag and SRP contributions of the panel model are described by Sentman's equations Doornbos (2011); March et al. (2019), as mentioned in subsection 2.2. Nevertheless, when using the panel geometry, the C_D is also estimated by escalating Sentman's equations with a parameter with initial value the unit. Thus, three geometries are implemented: cannonball model, scaled panel model, and unscaled panel model, in order to minimize any additional discrepancies between the dynamical environment used in this propagation, and one used to generate the POD orbit. The simple geometry of the cannonball model is widely used for space debris objects, for which the shape, size, orientation, and rotational motion is often poorly known.

Table 4: Different combinations of geometric satellite model and atmospheric density model.

Option	Geometry model	Density model
(a)	Cannonball	Calibrated
(b)	Cannonball	NLRMSISE-00
(c)	Scaled panel	Calibrated
(d)	Scaled panel	NLRMSISE-00
(e)	Panel	Calibrated
(f)	Panel	NLRMSISE-00

Therefore, six different options were tested, as covered in Table 4: (a) estimating the C_D, C_R, and state of the satellite when modelling the density using the calibrated density model, and a cannonball geometry, (b) estimating the C_D, C_R, and state of the satellite using original NRLMSISE-00 density model, and a cannonball geometry, (c) estimating the C_D and C_R as an scaling factor for the panel model, the state of the satellite, and propagating with the calibrated density model, (d) estimating the C_D and C_R as a scaling factor for the panel model, the state of the satellite, and propagating with the NRLMSISE-00 calibrated density model, (e) estimating only the state of the satellite, and using the panel model unscaled, and propagating with the calibrated density model, and (f) estimating only the state of the satellite, and using the panel model unscaled, and propagating with NRLMSISE-00 density model.

Figure 10 shows the result of the bootstrapping strategy, explained in subsection 2.2, for Swarm C satellite, the six options considered grouped by geometry, allowing a visual comparison between the calibrated density model and NRLMSISE-00. The result for GRACE-FO 1 satellite is shown in

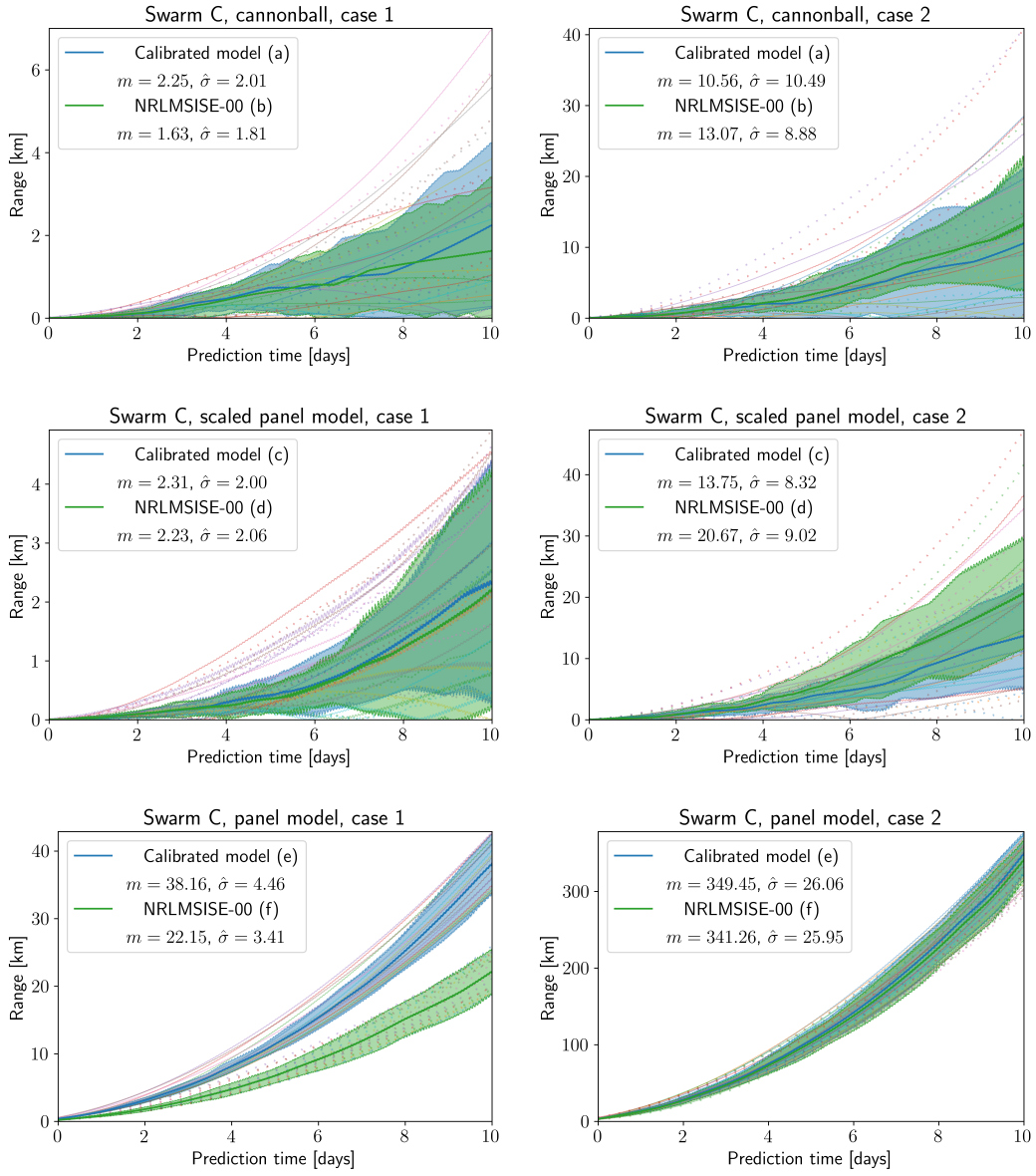

Fig. 10: Results of the moving window strategy for satellite Swarm C, for three geometry models, and two cases. Median m and Median Absolute Deviation (MAD) $\hat{\sigma}$ in km.

Figure 11. No bootstrapping could be performed for satellite Sentinel 1-A because of its frequent manoeuvres, but only a representative window is shown in Figure 12. For each of the 2 satellites, 6 options and 2 temporal cases considered, the bootstrapping strategy yielded a total of 19 windows, each spanning 3 days of orbital fit and 10 days of propagation. This approach involved moving a 13-day window from the 1^{st} to the 18^{th} to generate 19 distinct windows. During the orbit prediction, both the calibrated NRLMSISE-00 and normal NRLMSISE-00 models were employed. For each window, the range against the POD orbit was plotted, and, to provide a robust statistic, the median m and the Median Absolute Deviation (MAD) $\hat{\sigma}$ of the windows were

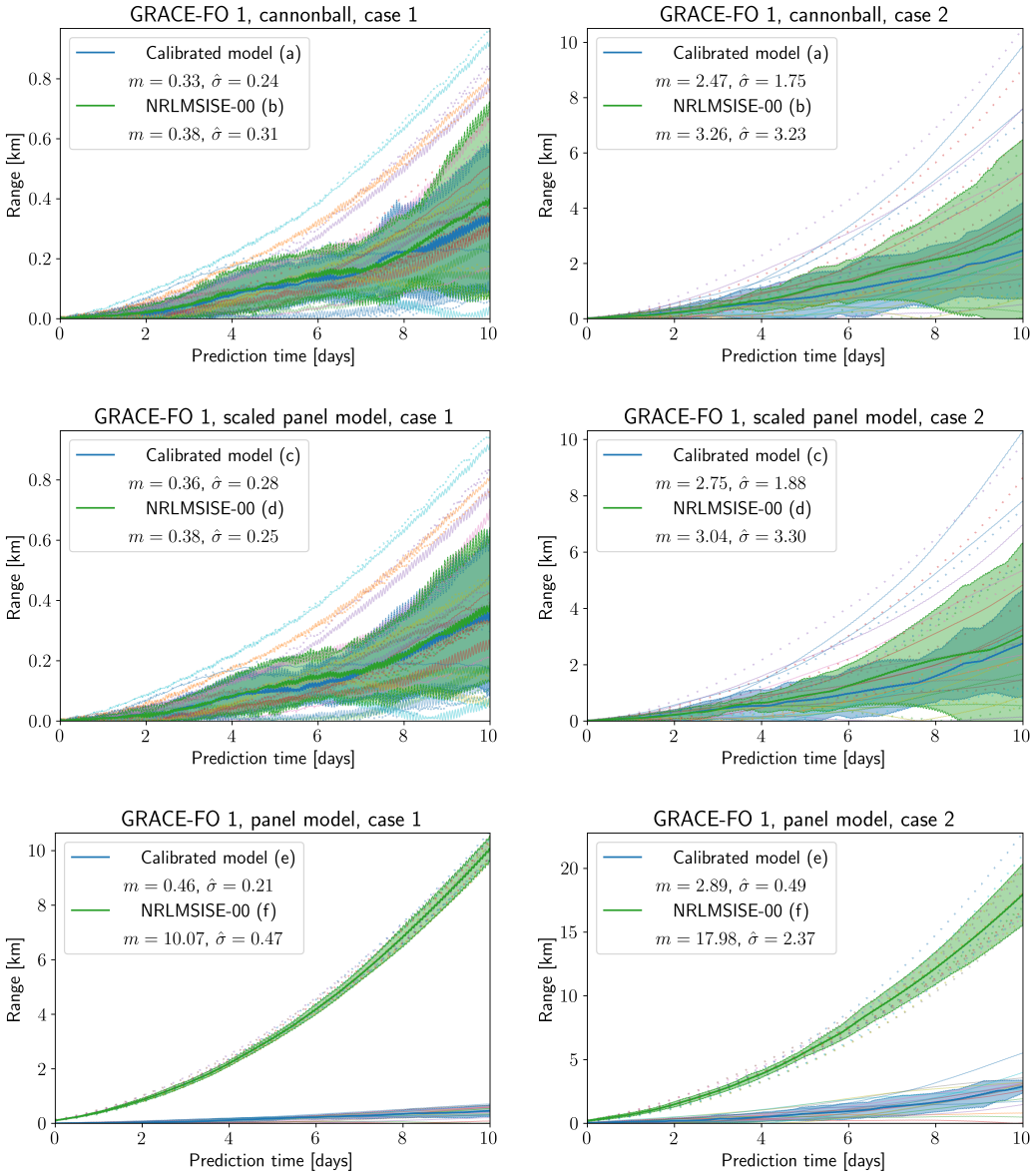

Fig. 11: Results of the moving window strategy for satellite GRACE-FO 1, for three geometry models, and two cases. Median m and Median Absolute Deviation (MAD) $\hat{\sigma}$ in km.

computed during the prediction:

$$\hat{\sigma} = \text{median}(|r_i - m|) \cdot 1.4826 \qquad (10)$$

In Equation 10, $r_i = |\mathbf{r}_{pre,i} - \mathbf{r}_{pod,i}|$ represents the range of the satellite, i.e., the difference of predicted RMS position $r_{pre,i}$ with the POD orbit RMS position $r_{pod,i}$, for the window i. The factor 1.4826 is included to use the MAD as a consistent estimator with the standard deviation, namely, an estimator for which 68.27% of the values of a Gaussian distribution would lie within one MAD of the median.

In Figure 10 and Figure 11, the temporal evolution of the median of the windows is plotted in blue for the calibrated model, and in green for NRLMSISE-00. A half-transparent region of the same colour indicates

a spread of $m \pm \hat{\sigma}$. In the background, thin solid lines represent each of the windows for the calibrated model, and dashed lines for NRLMSISE-00. The values for the median and the MAD at the end of the prediction time is also shown in the legend in Figure 10 and Figure 11, while the final range for all the windows is covered in Appendix A.

Overall, the calibrated model has performed better for Swarm C in case 2, March 2022, for GRACE-FO, in both cases and all options. Figure 10 shows the orbit prediction bootstrapping results for satellite Swarm C. During case 1, the median at the end of the prediction slightly increases when using the calibrated atmosphere and a cannonball geometry , from $1.63\,\mathrm{km}$ (b) to $2.25\,\mathrm{km}$ (a). With the scaled panel model geometry, the median slightly increases from $2.23\,\mathrm{km}$ (d) to $2.31\,\mathrm{km}$ (c). During case 2, the median at the end of the prediction is reduced from $13.07\,\mathrm{km}$ (b) to $10.56\,\mathrm{km}$ (a) with cannonball geometry, and from $20.67\,\mathrm{km}$ (d) to $13.75\,\mathrm{km}$ (c) with scaled panel geometry. The MAD slightly increases for all options except for the scaled panel geometry during case 2. As the results for all the windows in Appendix A show, the calibrated model shows an improvement for around half of the windows tested, when using a fitted geometry (panel model, and cannonball). Thus, performing a fit with POD observations might have a similar effect than calibrating the atmospheric model with TMD observations. In the bottom row of Figure 10 it is shown that the panel model without scaling performs notably worse than the above fitted geometries. The final median of the prediction is more than one order of magnitude higher for the (unscaled) panel model, and the calibrated model increases the MAD at both cases: $22.15\,\mathrm{km}$ (f) to $38.16\,\mathrm{km}$ (e) at case 1, and $341.26\,\mathrm{km}$ (f) to $341.45\,\mathrm{km}$ (e) at case 2. The decrease in accuracy using Swarm C panel model might be due to the 30% difference in accuracy of the panel model with respect to high fidelity panel models (March et al., 2019), explaining the need to scale the geometry.

On the other hand, the orbit prediction of GRACE-FO 1 using the calibrated model improved for both cases and all geometries, as shown in Figure 11. For case 1, the final median of the 19 windows was reduced from $0.38\,\mathrm{km}$ (b) to $0.33\,\mathrm{km}$ (a) with a cannonball geometry, from $0.38\,\mathrm{km}$ (d)to $0.36\,\mathrm{km}$ (c) with the scaled panel model, and from $10.07\,\mathrm{km}$ (f) to $0.46\,\mathrm{km}$ (e) with the (unscaled) panel model. For case 2, the median was reduced from $3.26\,\mathrm{km}$ (b) to $2.47\,\mathrm{km}$ (a) with a cannonball geometry, from $3.04\,\mathrm{km}$ (d) to $2.75\,\mathrm{km}$ (c) with the scaled panel model, and from $17.98\,\mathrm{km}$ (f) to $2.89\,\mathrm{km}$ (e) with the (unscaled) panel model. The panel geometry, in combination with the calibrated atmosphere, obtained a similar order of magnitude than the fitted geometries. Nevertheless, for the cannonball and scaled panel geometries, as with Swarm C, the calibrated model improves the accuracy for half of the 19 tests, as detailed in Appendix A.

The prediction range increases by one order of magnitude in case 2 compared with case 1, when the drag force is higher due to an increased atmospheric TMD. For satellite GRACE-FO and case 2, the sparsity of the prediction is reduced, the MAD decreases from $3.30\,\mathrm{km}$ to $1.88\,\mathrm{km}$ with the panel model, and from $3.23\,\mathrm{km}$ to $1.75\,\mathrm{km}$ with the cannonball geometry, as Figure 11 shows. The sparsity of the results for Swarm C is also more prominent for case 2, as Figure 10, but only for the scaled panel geometry. The results suggest that a higher sparsity is achieved for higher solar conditions.

Comparing the scaled panel geometry with the unscaled geometry prediction for GRACE-FO 1 satellite, the prediction with the scaled geometry outperforms the unscaled panel for both calibrated and NRLMSISE-00, case 1 and case 2. Only in case 2, the prediction with the calibrated atmosphere and unscaled panel model is closer to POD orbit than the prediction with NRLMSISE-00 and scaled panel model. When comparing Swarm C satellite, the unscaled geometry gives a range with respect to the POD orbit which is around ten times higher than the scaled geometry, for both the calibrated and NRLMSISE-00 atmospheric model, and case 1, and case 2. As mentioned before, the inaccuracy in the panel geometry might be the reason for the inability of the calibrated atmosphere model to improve the accuracy. However, as long as the C_D is estimated in some form, the accuracy of the propagation improves. This result, on the one side, consolidates the need for descriptive geometries of space objects, asserts the importance of estimation of the orbital state before orbit prediction, and suggests that using a detailed dynamical environment would enhance further the capabilities of the calibrated model. On the other hand, the inability to provide either a detailed dynamical model (for example, because of computational limitations or because of model uncertainty), or a detailed object geometry (for example, in the case of a poorly tracked space debris

object) would diminish the accuracy improvement of the calibrated atmospheric model.

Table 5 shows the percentage of windows for which the calibrated model outperforms NRLMSISE-00. It confirms the already mentioned fact that the panel model for GRACE-FO enhances the calibrated model, while Swarm C panel model is not descriptive enough. Although the number of windows for which the prediction improves are between 45% and 70%, the mean and MAD described above show a more robust analysis of the improvement for each test case.

It was expected that the range would grow quadratically with time. However, it is not the general case for all the orbital propagations. For some window and options, the range would decrease to zero to afterwards increase quadratically, indicating that the POD orbit and the propagated orbit had cross paths. This fact might indicate that more tests cases are needed, for example, extending the test cases to more months. Furthermore, the assumed dynamical environment might have a key role on the interaction with the atmospheric modelling, as it can enhance or diminish the modes described in subsection 3.1. However, the investigation of the interaction of the modes with the dynamical perturbations is out of the scope of this work.

Satellite Sentinel 1-A, flying at a higher altitude, $690\,\mathrm{km}$ performs frequent manoeuvres during both time cases (February 2019 and March 2022), and thus, the slicing window tests could not be performed. However, a representative estimation and prediction is shown in Figure 12 for the six options and both test cases. Figure 12 shows both the range of the prediction with respect to the POD orbit and the projection in the local reference frame Tangential-Normal-Along track reference frame. The tangential direction of this frame is collinear with the velocity of the satellite, the cross-track axis is perpendicular to the orbit plane, and the normal axis is similar to the acceleration direction. The main deviation, as expected, is on the tangential direction. A slight deviation is observed on the normal axis, and small periodical variations are observed in the cross-track axis. For case 1, the initial extended state is estimated from the 24^{th} to 27^{th} of January 2019, and the orbit is afterwards propagated until the end of the month (4 days). In this case, option (c), accumulates a propagation error around $25\,\mathrm{m}$ after the 4 days propagation, followed by option (a), which accumulates a prediction error of $30\,\mathrm{m}$. Then, options (d) and (b), which correspond to NRLMSISE-00 density model, obtain a slightly worse prediction error, around $35\,\mathrm{m}$ and $40\,\mathrm{m}$ respectively. As with Swarm C, the estimation procedure during the initial epochs of the test does not converge with a (unscaled) panel model geometry, and options (e) and (f) quickly deviate from the POD orbit.

For case 2, the orbit prediction evolution is shown in the right half of Figure 12. The estimation is performed from the 17^{th} of March 2022 to the 20^{th}, and the orbit is predicted for 10 days. In this case, at the last epoch, the outperforming model and geometry is also option (c), below $50\,\mathrm{m}$. However, the orbital evolution does not grow quadratically with time from the start for the fitted geometries, options (a) to (d), as the predicted orbit crosses the POD orbit. Therefore, from the 21^{th} to the 26^{th}, option (e) outperforms the other combinations. Then, from the 26^{th} to the 29^{th}, the best model and geometry are option (a), followed by options (c), (b), and (d). The particular evolution range of the different geometries and models during the propagation suggests that extended tests are needed to thoroughly analyse the accuracy of orbit prediction with assimilation of TMD observations in a density model. However, the improvement with a scaled panel model is a promising result, which might indicate the potential of this method to override the coupling between TMD and C_D in the formulation on drag.

When comparing the propagation for the three satellites, the most significant difference is the magnitude of the range. For case 1, options (a) to (d), Swarm C range raises to $6\,\mathrm{km}$, while GRACE-FO 1 range is bounded to $800\,\mathrm{m}$, and Sentinel 1-A is bounded to $40\,\mathrm{m}$. During case 2, as the density signal is higher, the maximum range is $40\,\mathrm{km}$, $10\,\mathrm{km}$, and $500\,\mathrm{m}$, respectively, as the altitude increases and the atmosphere vanishes. Regarding the improvement made by assimilating Swarm C density observations, it appears to be higher when the drag signal is higher, that is, in lower altitudes, and medium solar conditions. The test cases could be extended to confirm this hypothesis.

The projection of GRACE-FO 1 and Swarm C satellites was also computed, obtaining similar a similar shape of TNW projections than Figure 12. The main difference with POD orbit is in the tangential component, while an oscillatory behaviour of one order of magnitude less is observed in the cross-track component. On the T-N projection, the normal component appears to grow quadratically with the tangential deviation from the nominal orbit. Further investigation is needed to determine the physical cause

Table 5: Percentage of time windows (out of the 19 distinct windows) in which the calibrated model outperforms NRLMSISE-00.

GRACE-FO 1			Swarm C		
Case	Geometry	Percentage	Case	Geometry	Percentage
Case 1	Cannonball	68.42%	Case 1	Cannonball	57.89%
	Scaled panel model	63.16%		Scaled panel model	47.37%
	Panel model	100%		Panel model	0%
Case 2	Cannonball	52.63%	Case 2	Cannonball	68.42%
	Scaled panel model	47.37%		Scaled panel model	57.89%
	Panel model	100%		Panel model	0%

of the normal and cross-track evolution. Nevertheless, the oscillation on the cross-track axis could be due to the nodal precession, i.e., the effect of the oblateness of the Earth on the longitude of the ascending node. On the other hand, the quadratic relation between normal and tangential components could be explained with the relation between velocity and altitude of an orbit, for small changes on the altitude of the orbit. However, a detailed analysis of these effects is out of the scope of this work.

The C_D product of the estimation of the dynamical model is displayed in Table 6 for a representative window test of each satellite and option that include a fitted geometry. For Swarm C and GRACE-FO 1, the C_D as obtained from (March et al., 2019) is also included. March et al. (2019) computed the C_D by using a high-fidelity geometry, and providing the reference values for the C_D depending on different values for aerodynamic angles of attack α and side-slip β, and speed ratio S. To provide the number in Table 6, the aerodynamic angles have been assumed null $\alpha = \beta = 0°$. Parameter S, on the other hand, has been carefully chosen. It is defined as the ratio between satellite speed v and the most probable speed of the atmospheric particles:

$$S = \frac{v}{\sqrt{\frac{2kT_{inc}}{m_{atm}}}} \tag{11}$$

In Equation 11, $k = 1.380\,649 \cdot 10^{-23}\,\mathrm{J\,K^{-1}}$ is the Boltzmann constant, T_{inc} is the local atmospheric temperature, and m_{atm} is the molecular mass of the atmospheric particle. As the model NRLMSISE-00 gives the local concentration of each atmospheric species, as well as the local atmospheric temperature, a speed ratio has been computed for each particle. Then, the weighted average has been computed using the local concentration of each species. This assumption should not degrade the C_D obtained from March et al. (2019), neither the null angle of attack and side-slip for a cannonball geometry (options a and b). However, for the panel model, certain attitude has been computed, which might modify the instantaneous C_D. Further analysis might be required on the attitude dynamics of the satellite to compare the panel model implemented with the models in March et al. (2019) in a trustworthy manner.

Regarding the scaled C_D of the panel model, options (c) and (d), the values of the C_D obtained with the fit have been scaled to the reference area in Table 3, using the associated area to each panel model, in order to provide a comparison with the values for the cannonball model.

Table 6 shows that the estimated C_D for Swarm C and GRACE-FO 1 is closer to literature values for the cannonball model, in case 1. In low solar activity, NRLMSISE-00 overpredicts density by a factor of two (He et al., 2018), effect that is then applied on the C_D during the estimation. On the other hand, in case 2, the estimated C_D increases, but exceeds the reference value in literature. For options (c) and (d), Swarm C estimated C_D is higher than the reference value in case 1 by almost a factor of three: 9.964 for option (a), 4.804 for option (b), and 3.522 in literature. In case 2, the estimated C_D is lower than the reference value by a factor around two. On the other hand, the estimation for GRACE-FO 1 obtains more similar C_D values to literature with the calibrated model. Again, this difference might be due to the 32% error with respect to high fidelities model in Swarm C panel model described by March et al. (2019).

In summary, the orbit prediction with the different atmospheric density models, satellite geometries, time windows, satellites, and solar activity conditions present a clear view of the requirements of the assimilation procedure, its potential, and its limitations.

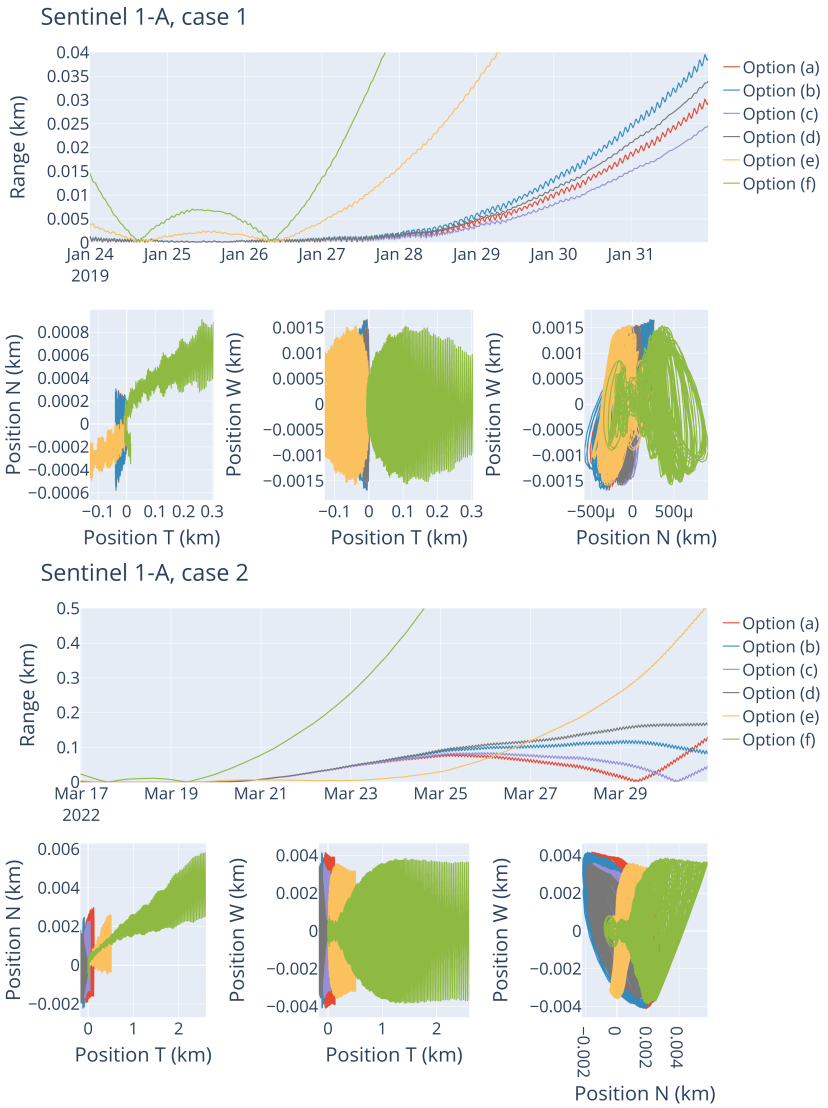

Fig. 12: Representative Sentinel 1-A orbit estimation and prediction for case 1 (top) and case 2 (bottom).

Table 6: Estimated C_D for the different combinations of satellites, test cases, and options.

	Case 1			Case 2		
	Swarm C	GRACE-FO 1	Sentinel 1	Swarm C	GRACE-FO 1	Sentinel 1
Option (a)	3.957	3.690	5.133	4.026	3.600	5.069
Option (b)	1.985	2.036	2.789	3.174	2.908	2.709
Option (c)	9.964	3.453	4.524	1.731	2.183	1.168
Option (d)	4.804	1.914	2.472	1.344	1.763	0.627
March et al. (2019)	3.522	3.964	-	3.453	3.384	-

4 Conclusions

In summary, the results present a study on improving the accuracy of satellite orbit propagation through the calibration of atmospheric density models. NRLMSISE-00 model has been factorized into a PCA, and the calibration method has been developed and verified. The main modes of the PCA decomposition correspond to physical phenomena and capture most of the energy of the system. The complexity of the problem is reduced while also retaining 92.89% of the density grid information. A simple, but effective LSE algorithm has been proposed as a means of reducing the over-prediction of NRLMSISE-00 when comparing it to GNSS-derived thermospheric density observations. The calibration has been validated, and two tests have determined that it is feasible to use this method to predict values of the density in the close future. Observed values for the $F_{10.7}$ and a_P indices have been used, as using a predicted value would add another source of uncertainty.

Finally, the propagation of orbits using the calibrated model has been tested with three satellites, namely Swarm C, GRACE-FO 1, and Sentinel 1-A, each one with three different geometrical descriptions: a cannonball model, a scaled panel model, and a (non-scaled) panel model. Two different cases have been considered: low solar activity (January 2019, case 1), and medium solar activity (March 2022, case 2). The prediction with the calibrated density model has been compared with the nominal NRLMSISE-00 model for all options considered. As POD orbit is available for all three satellites, an orbital fit has been performed prior to the propagation. For the cannonball model, the co-estimation of the C_D was expected to overshadow the benefits of the calibration, as both C_D and density affect the drag acceleration in the same way. However, the method increased the accuracy of the propagation for some variations of the initial epoch, and a more realistic C_D coefficient is drawn from the orbital fit with the calibrated model, which might be beneficial for space objects without precisely known orbits. With a realistic C_D coefficient, not only the prediction can be improved, but the uncertainty on the size, shape, and attitude of the object can be reduced.

The results show the importance of the appropriate selection of the dynamical environment to perform orbital predictions, as geopotential contribution of order and degree up to 200x200 is not negligible, a higher order than the typical needs in SST LEO orbit prediction. The results show that in certain cases, the calibrated density model greatly improves the accuracy of the orbit propagation compared to the nominal NRLMSISE-00 model. To provide a robust estimator, the median and MAD of 19 moving window tests has been computed. For the options with a higher drag signal, that is, case 1, and lower-flying satellites, the median and the MAD is reduced with the calibrated density model. A panel model that accurately describes the dynamics of the satellite would complement the density model. The best improvement was obtained with a panel geometry for Swarm C satellite, in which the median of the orbit prediction range is reduced from $20.67\,\mathrm{km}$ to $13.75\,\mathrm{km}$ with the calibrated model. Overall, this study provides important insights into the calibration of atmospheric density models and its impact on the accuracy of satellite orbit propagation.

The accuracy of the calibrated density model depends heavily on the dynamical environment and the satellite geometry. It is crucial to have a descriptive enough dynamical propagation to obtain better results. The use of interpolated attitude, a scaled panel model, and estimating the initial state before the prediction can enhance the potential of any atmospheric model. Additionally, when the panel model accurately describes the satellite, the density model improves the propagation deviation with respect to the POD orbit significantly, regardless of the solar conditions. That is the case for the panel model geometry implemented for GRACE-FO 1. For every window, the accuracy of the propagation with the calibrated density model outperformed NRLMSISE-00. Despite the fact that NRLMSISE-00 overestimated atmospheric density by a factor of two during low solar conditions in 2019, the calibrated model demonstrated similar accuracy for both low (case 1) and medium (case 2) solar conditions in the general case, contrary to the initial expectation of higher differences. Thus, the inability of NRLMSISE-00 to accurately describe the thermosphere during low solar conditions might not be adjusted by assimilation of TMD observations. However, further research is needed to establish the physical cause of the improvement during different solar activities, as the cause is more complex than a scaling of the density model. In this regard, the use of sequential estimators to adjust the atmospheric model during the prediction might be more beneficial than the simple LSE used.

As future steps of this research, outside the scope of this master's thesis, it remains open to consider other sources of uncertainty in the propagation. In

this work, the solar indices that form the input of NRLMSISE-00 have been the observed ones. Using predicted solar indices would add a non-negligible source of error in the density prediction, that would propagate to drag, and to the orbital state. The calibrated model has been chosen as NRLMSISE-00, however, more recent models, like Drag Temperature Model 2020 (Bruinsma & Boniface, 2021), which are fitted in the least squares sense to Swarm TMD observations, might equal the benefits of the calibration performed in this work. Further analysis is needed to compare the calibrated model presented here to recent versions of thermospheric density models. The spatial grid, input of the PCA decomposition, has been performed in longitude and latitude. Nevertheless, the changes of atmospheric density with respect to Local Solar Time (LST) are more prominent than to longitude (He et al., 2018). Hence, using LST and latitude as a two-dimensional grid could allow reducing the coverage of the grid, and reducing the uncertainty of the model.

The attitude of the spacecraft with a panel model has been downloaded from ESA public dissemination of spacecraft data, and thus, substituting it for simulated attitude would increase the uncertainty. Including test cases of objects without known shape, attitude, or POD orbit might give a clearer understanding of the limitations of the calibrated model. Finally, other periods and solar conditions would need to be included to completely assess the accuracy of the improved density model. Similarly, the different test cases and options could be extended to include other space objects, solar conditions, and object geometries. A test could be performed on a well-tracked space debris object, that would have enough TLE observations for an estimation on its C_D and C_R to converge. As this results suggest, the calibrated density model should be descriptive enough for the predictions on a space debris object to improve the accuracy. The higher order and degree of Earth gravity field terms having a significant importance in the propagation was initially unexpected. Therefore, it is recommended to consider factors such as the dynamical environment in LEO, including temporal variation of geopotential harmonics, gravity bulge due to lunisolar and ocean tides, and other perturbations. Additionally, the method could be extended to a sequential estimator that can include near-real density observations of Swarm spacecraft to enhance the density model in an operational setup.

Realistic uncertainty characterization of the density contribution, and propagating the contribution to drag, and to the orbit prediction, would improve SST applications as, for example, such as collision prediction and avoidance. Nevertheless, being able to characterize the uncertainty in a realistic manner would require to first, characterize the initial uncertainty of the orbit, and then, to propagate it in a trustworthy manner. The spread of Figure 10 and Figure 11 examples how a quite similar initial problem can spread up to $9.02\,\mathrm{km}$, due to the uncertainty on the density model. In conclusion, being able to accurately characterize and propagate LEO orbits through calibration of density model would hugely benefit the needs of both the space industry and space research community.

Appendix A Moving window

The range improvement made with the calibrated NRLMSISE-00 model for the three satellites, two test cases, and three different geometrical specifications are listed here, in Table A1 to Table A12. The difference in range is also computed as $\Delta r = r_{msi} - r_{cal}$.

Table A1: Swarm C, case 1, cannonball geometry: options (a) and (b).

Epoch (Jan. 2019)	r_{msi} [km]	r_{cal} [km]	Δr [km]
4^{th}	0.995	0.901	0.094
5^{th}	3.387	3.155	0.232
6^{th}	0.314	0.266	0.048
7^{th}	4.827	5.879	-1.052
8^{th}	5.953	7.005	-1.052
9^{th}	4.580	5.577	-0.996
10^{th}	2.971	3.864	-0.893
11^{th}	1.628	2.397	-0.768
12^{th}	1.025	0.286	0.740
13^{th}	1.287	0.560	0.727
14^{th}	0.007	0.432	-0.425
15^{th}	1.447	1.042	0.405
16^{th}	3.409	2.811	0.598
17^{th}	3.697	3.060	0.637
18^{th}	2.849	2.254	0.595
19^{th}	0.762	0.083	0.680
20^{th}	0.767	1.173	-0.406
21^{th}	0.977	0.902	0.075
22^{th}	2.710	2.764	-0.053

Table A2: Swarm C, case 1, scaled panel model: options (c) and (d).

Epoch (Jan. 2019)	r_{msi} [km]	r_{cal} [km]	Δr [km]
4^{th}	1.314	2.488	-1.175
5^{th}	3.937	4.560	-0.624
6^{th}	3.717	4.337	-0.620
7^{th}	2.410	2.999	-0.589
8^{th}	1.579	2.314	-0.735
9^{th}	0.326	0.965	-0.640
10^{th}	0.392	0.832	-0.441
11^{th}	0.842	0.429	0.413
12^{th}	3.018	2.528	0.489
13^{th}	2.381	2.143	0.238
14^{th}	0.764	0.771	-0.006
15^{th}	2.231	2.209	0.022
16^{th}	4.645	4.360	0.285
17^{th}	4.919	4.540	0.378
18^{th}	4.141	3.728	0.413
19^{th}	2.127	1.633	0.495
20^{th}	0.069	0.021	0.047
21^{th}	1.016	1.345	-0.329
22^{th}	2.690	3.035	-0.344

Table A3: Swarm C, case 1, unscaled panel model: options (e) and (f).

Epoch (Jan. 2019)	r_{msi} [km]	r_{cal} [km]	Δr [km]
4^{th}	24.399	41.846	-17.446
5^{th}	24.876	42.538	-17.663
6^{th}	25.171	42.880	-17.709
7^{th}	23.716	40.872	-17.156
8^{th}	21.700	38.159	-16.459
9^{th}	20.016	35.922	-15.906
10^{th}	19.057	34.540	-15.483
11^{th}	18.761	34.011	-15.250
12^{th}	18.737	33.754	-15.017
13^{th}	19.215	34.060	-14.845
14^{th}	19.433	34.174	-14.741
15^{th}	20.083	34.968	-14.885
16^{th}	21.070	36.062	-14.993
17^{th}	22.151	37.148	-14.997
18^{th}	23.324	38.385	-15.061
19^{th}	23.932	38.941	-15.010
20^{th}	24.451	39.480	-15.029
21^{th}	24.937	40.031	-15.094
22^{th}	25.901	41.164	-15.263

Table A4: Swarm C, case 2, cannonball model: options (a) and (b).

Epoch (Mar. 2022)	r_{msi} [km]	r_{cal} [km]	Δr [km]
4^{th}	27.659	14.413	13.245
5^{th}	40.890	28.391	12.499
6^{th}	20.534	12.757	7.777
7^{th}	0.514	2.259	-1.745
8^{th}	15.018	18.960	-3.941
9^{th}	11.969	8.858	3.111
10^{th}	6.847	1.852	4.995
11^{th}	8.963	3.485	5.477
12^{th}	13.069	19.600	-6.530
13^{th}	12.330	6.102	6.228
14^{th}	3.352	2.911	0.441
15^{th}	22.601	9.513	13.088
16^{th}	40.870	26.087	14.782
17^{th}	14.884	10.563	4.322
18^{th}	9.202	11.210	-2.008
19^{th}	13.282	12.605	0.676
20^{th}	7.083	0.246	6.837
21^{th}	4.266	5.217	-0.951
22^{th}	16.546	28.537	-11.991

Table A5: Swarm C, case 2, scaled panel model: options (c) and (d).

Epoch (Mar. 2022)	r_{msi} [km]	r_{cal} [km]	Δr [km]
4^{th}	41.536	26.110	15.426
5^{th}	47.294	36.710	10.584
6^{th}	14.590	7.168	7.422
7^{th}	11.230	19.357	-8.126
8^{th}	29.998	34.515	-4.518
9^{th}	23.060	19.360	3.701
10^{th}	24.917	14.331	10.586
11^{th}	21.924	7.063	14.861
12^{th}	4.204	8.358	-4.153
13^{th}	3.835	10.932	-7.097
14^{th}	10.624	14.758	-4.134
15^{th}	20.673	5.067	15.607
16^{th}	23.404	13.749	9.655
17^{th}	3.230	5.350	-2.120
18^{th}	24.021	24.706	-0.685
19^{th}	24.371	21.748	2.623
20^{th}	20.364	11.520	8.844
21^{th}	18.954	8.600	10.353
22^{th}	0.769	11.335	-10.566

Table A6: Swarm C, case 2, scaled panel model: options (e) and (f).

Epoch (Mar. 2022)	r_{msi} [km]	r_{cal} [km]	Δr [km]
4^{th}	301.954	311.823	-9.869
5^{th}	323.757	333.655	-9.898
6^{th}	342.038	351.904	-9.866
7^{th}	350.021	359.850	-9.829
8^{th}	350.403	360.181	-9.778
9^{th}	351.879	361.565	-9.686
10^{th}	357.428	367.028	-9.600
11^{th}	363.830	373.305	-9.475
12^{th}	368.551	377.939	-9.388
13^{th}	360.093	369.318	-9.225
14^{th}	348.517	357.598	-9.081
15^{th}	330.922	339.824	-8.903
16^{th}	310.503	319.297	-8.794
17^{th}	294.433	303.050	-8.616
18^{th}	294.441	302.932	-8.491
19^{th}	299.242	307.598	-8.356
20^{th}	310.649	318.931	-8.282
21^{th}	324.863	333.091	-8.228
22^{th}	341.261	349.453	-8.192

Table A7: GRACE-FO 1, case 1, cannonball model: options (a) and (b).

Epoch (Jan. 2019)	r_{msi} [km]	r_{cal} [km]	Δr [km]
4^{th}	0.405	0.245	0.160
5^{th}	0.662	0.506	0.156
6^{th}	0.845	0.774	0.072
7^{th}	0.313	0.320	-0.007
8^{th}	0.175	0.169	0.006
9^{th}	0.364	0.351	0.014
10^{th}	0.472	0.449	0.023
11^{th}	0.968	0.928	0.040
12^{th}	0.066	0.101	-0.035
13^{th}	0.774	0.809	-0.035
14^{th}	0.069	0.139	-0.070
15^{th}	0.352	0.279	0.073
16^{th}	0.439	0.380	0.059
17^{th}	0.383	0.330	0.054
18^{th}	0.627	0.688	-0.061
19^{th}	0.408	0.475	-0.068
20^{th}	0.151	0.064	0.087
21^{th}	0.086	0.025	0.061
22^{th}	0.338	0.220	0.118

Table A8: GRACE-FO 1, case 1, scaled panel model: options (c) and (d).

Epoch (Jan. 2019)	r_{msi} [km]	r_{cal} [km]	Δr [km]
4^{th}	0.347	0.176	0.171
5^{th}	0.593	0.422	0.171
6^{th}	0.836	0.762	0.074
7^{th}	0.351	0.363	-0.012
8^{th}	0.212	0.212	0.000
9^{th}	0.388	0.379	0.010
10^{th}	0.482	0.461	0.021
11^{th}	0.963	0.922	0.042
12^{th}	0.077	0.114	-0.038
13^{th}	0.777	0.814	-0.037
14^{th}	0.088	0.164	-0.076
15^{th}	0.325	0.243	0.082
16^{th}	0.432	0.371	0.061
17^{th}	0.378	0.322	0.055
18^{th}	0.636	0.700	-0.064
19^{th}	0.411	0.479	-0.068
20^{th}	0.135	0.046	0.089
21^{th}	0.052	0.062	-0.010
22^{th}	0.296	0.172	0.124

Table A9: GRACE-FO 1, case 1, panel model: options (e) and (f).

Epoch (Jan. 2019)	r_{msi} [km]	r_{cal} [km]	Δr [km]
4^{th}	10.067	0.012	10.055
5^{th}	10.308	0.078	10.230
6^{th}	10.548	0.209	10.340
7^{th}	10.409	0.326	10.083
8^{th}	10.042	0.407	9.634
9^{th}	9.737	0.457	9.280
10^{th}	9.641	0.531	9.110
11^{th}	9.728	0.656	9.073
12^{th}	9.752	0.713	9.040
13^{th}	9.570	0.601	8.968
14^{th}	9.555	0.545	9.010
15^{th}	9.840	0.589	9.251
16^{th}	10.072	0.635	9.437
17^{th}	10.199	0.659	9.541
18^{th}	10.244	0.581	9.663
19^{th}	10.260	0.420	9.840
20^{th}	10.340	0.348	9.992
21^{th}	10.474	0.317	10.157
22^{th}	10.626	0.271	10.356

Table A10: GRACE-FO 1, case 2, cannonball model: options (a) and (b).

Epoch (Mar. 2022)	r_{msi} [km]	r_{cal} [km]	Δr [km]
4^{th}	6.130	2.193	3.937
5^{th}	9.072	5.286	3.786
6^{th}	3.263	0.520	2.743
7^{th}	1.215	1.465	-0.250
8^{th}	4.882	5.261	-0.380
9^{th}	2.875	1.595	1.280
10^{th}	0.700	1.998	-1.298
11^{th}	1.236	2.312	-1.077
12^{th}	5.439	7.589	-2.150
13^{th}	3.277	2.473	0.805
14^{th}	0.794	0.236	0.559
15^{th}	6.500	3.799	2.701
16^{th}	10.507	7.608	2.899
17^{th}	4.406	3.654	0.753
18^{th}	1.999	2.238	-0.239
19^{th}	3.033	2.756	0.278
20^{th}	0.771	0.779	-0.008
21^{th}	0.944	3.061	-2.117
22^{th}	7.105	9.883	-2.779

Table A11: GRACE-FO 1, case 2, scaled panel model: options (c) and (d).

Epoch (Mar. 2022)	r_{msi} [km]	r_{cal} [km]	Δr [km]
4^{th}	5.660	1.691	3.969
5^{th}	8.641	4.832	3.809
6^{th}	2.899	0.149	2.750
7^{th}	1.242	1.480	-0.238
8^{th}	4.971	5.359	-0.388
9^{th}	2.697	1.422	1.275
10^{th}	0.373	2.329	-1.956
11^{th}	0.809	2.749	-1.941
12^{th}	5.672	7.818	-2.145
13^{th}	3.037	2.233	0.804
14^{th}	0.497	0.529	-0.032
15^{th}	5.932	3.245	2.687
16^{th}	9.857	6.977	2.879
17^{th}	4.168	3.416	0.752
18^{th}	2.115	2.354	-0.239
19^{th}	3.078	2.798	0.280
20^{th}	0.655	0.905	-0.250
21^{th}	1.201	3.335	-2.134
22^{th}	7.508	10.313	-2.806

Table A12: GRACE-FO 1, case 2, panel model: options (e) and (f).

Epoch (Mar. 2022)	r_{msi} [km]	r_{cal} [km]	Δr [km]
4^{th}	16.943	1.936	15.007
5^{th}	16.642	2.567	14.075
6^{th}	16.380	3.126	13.255
7^{th}	16.534	2.993	13.541
8^{th}	16.187	3.193	12.994
9^{th}	15.685	3.563	12.122
10^{th}	16.024	3.215	12.809
11^{th}	16.520	2.699	13.821
12^{th}	17.374	1.744	15.630
13^{th}	18.051	0.802	17.249
14^{th}	17.978	0.478	17.500
15^{th}	18.089	0.042	18.048
16^{th}	19.037	1.467	17.570
17^{th}	20.089	2.886	17.203
18^{th}	20.120	3.126	16.994
19^{th}	19.781	2.881	16.900
20^{th}	20.004	3.117	16.887
21^{th}	21.031	3.986	17.045
22^{th}	22.771	5.534	17.238

References

Bowden, G. (2022). Orbit-localised thermosphere density prediction using a Kalman filter based calibration of empirical models. *Acta Astronautica*, *197*, 6–13. doi:10.1016/j.actaastro.2022.05.005

Bowman, B., Tobiska, W.K., Marcos, F., Huang, C., Lin, C., Burke, W. (2008). A new empirical thermospheric density model JB2008 using new solar and geomagnetic indices. *AIAA/AAS astrodynamics specialist conference and exhibit*. American Institute of Aeronautics and Astronautics. doi:10.2514/6.2008-6438

Bruinsma, S. (2015). The DTM-2013 thermosphere model. *Journal of Space Weather and Space Climate*, *5*, A1. doi:10.1051/swsc/2015001

Bruinsma, S., & Boniface, C. (2021). The operational and research DTM-2020 thermosphere models. *Journal of Space Weather and Space Climate*, *11*, 47–1. doi:10.1051/swsc/2021032

Bruinsma, S., Boniface, C., Sutton, E.K., Fedrizzi, M. (2021). Thermosphere modeling capabilities assessment: geomagnetic storms. *Journal of Space Weather and Space Climate*, *11*, 12. doi:10.1051/swsc/2021002

Bruinsma, S., Sutton, E., Solomon, S., Fuller-Rowell, T., Fedrizzi, M. (2018). Space weather modeling capabilities assessment: Neutral density for orbit determination at low Earth orbit. *Space Weather*, *16*(11), 1806–1816. doi:10.1029/2018SW002027

Doornbos, E. (2011). Thermospheric density and wind determination from satellite dynamics. *Springer Science & Business Media*. doi:10.1007/978-3-642-25129-0

Doornbos, E., Klinkrad, H., Scharroo, R., Visser, P. (2007). Thermosphere density calibration in the orbit determination of ERS-2 and Envisat. H. Lacoste (Ed.), . Retrieved from https:\bit.ly/envisat_doornbos

Doornbos, E., Klinkrad, H., Visser, P. (2008). Use of two-line element data for thermosphere neutral density model calibration. *Advances in Space Research*, *41*(7), 1115–1122. doi:10.1016/j.asr.2006.12.025

ESA (2014). Swarm PDGS data access user manual (Computer software manual No. SWAM-GSEG-EOPG-MA-14-0032). Retrieved from https://bit.ly/swarm_pdgs

ESA (2022). *ESAs annual space environment report* (LOG No. GEN-DB-LOG-00288-OPS-SD). Space Debris Office. Retrieved from https://bit.ly/esa_debris

ESA (2023). *The Copernicus Open Access Hub*. Retrieved from https://scihub.copernicus.eu/

Forootan, E., Farzaneh, S., Kosary, M., Schmidt, M., Schumacher, M. (2020). A simultaneous calibration and data assimilation (C/DA) to improve NRLMSISE00 using thermospheric neutral density (TND) from space-borne accelerometer measurements. *Geophysical Journal International*, *224*(2), 1096–1115. doi:10.1093/gji/ggaa507

Forootan, E., Farzaneh, S., Lück, C., Vielberg, K. (2019). Estimating and predicting corrections for empirical thermospheric models. *Geophysical Journal International*, *218*(1), 479-493. doi:10.1093/gji/ggz163

GMV (2019). *Sentinel-1 properties for GPS POD* (Tech. Rep.). Retrieved from https://bit.ly/sentinel_pod

Gondelach, D.J., & Linares, R. (2020). Real-time thermospheric density estimation via two-line element data assimilation. *Space Weather*, *18*(2). doi:10.1029/2019sw002356

Gondelach, D.J., & Linares, R. (2021). Real-time thermospheric density estimation via radar and GPS tracking data assimilation. *Space Weather*, *19*(4). doi:10.1029/2020sw002620

He, C., Yang, Y., Carter, B., Kerr, E., Wu, S., Deleflie, F., ... Norman, R. (2018). Review and comparison of empirical thermospheric mass density models. *Progress in Aerospace Sciences*. doi:10.1016/j.paerosci.2018.10.003

JPL, N. (2019). *GRACE-FO Level-1B Release*

version 4.0 from JPL in ASCII. NASA Physical Oceanography DAAC. doi:10.5067/GFL1B-ASJ04

Kim, I., Pawlowski, D.J., Ridley, A.J., Bernstein, D.S. (2008). Localized data assimilation in the ionosphere-thermosphere using a sampled-data unscented Kalman filter. *2008 american control conference* (pp. 1849–1854). doi:10.1109/ACC.2008.4586761

Klinkrad, H. (2006). *Space debris: Models and risk analysis*. Springer-Verlag Berlin Heidelberg. doi:10.1007/3-540-37674-7

Licata, R.J., Mehta, P.M., Tobiska, W.K., Huzurbazar, S. (2022). Machine-learned HASDM thermospheric mass density model with uncertainty quantification. *Space Weather*, *20*(4). doi:10.1029/2021sw002915

March, G., Doornbos, E., Visser, P. (2019). High-fidelity geometry models for improving the consistency of CHAMP, GRACE, GOCE and Swarm thermospheric density data sets. *Advances in Space Research*, *63*(1), 213–238. doi:10.1016/j.asr.2018.07.009

Matsuo, T., Fedrizzi, M., Fuller-Rowell, T., Codrescu, M. (2012). Data assimilation of thermospheric mass density. *Space Weather*, *10*(5). doi:10.1029/2012SW000773

Mehta, P.M., & Linares, R. (2017). A methodology for reduced order modeling and calibration of the upper atmosphere. *Space Weather*, *15*(10), 1270–1287. doi:10.1002/2017SW001642

Montenbruck, O., & Gill, E. (2005). *Satellite orbits: Models, methods and applications*. Springer Science & Business Media. doi:10.1007/978-3-642-58351-3

Morozov, A.V., Ridley, A.J., Bernstein, D.S., Collins, N., Hoar, T.J., Anderson, J.L. (2013). Data assimilation and driver estimation for the Global Ionosphere–Thermosphere Model using the ensemble adjustment Kalman filter. *Journal of Atmospheric and Solar-Terrestrial Physics*, *104*, 126–136. doi:10.1016/j.jastp.2013.08.016

Pardini, C., Moe, K., Anselmo, L. (2012). Thermospheric density model biases at the 23rd sunspot maximum. *Planetary and Space Science*, *67*(1), 130–146. doi:10.1016/j.pss.2012.03.004

Picone, J.M., Hedin, A.E., Drob, D.P., Aikin, A.C. (2002). NRLMSISE-00 empirical model of the atmosphere: Statistical comparisons and scientific issues. *Journal of Geophysical Research: Space Physics*, *107*(A12), SIA 15–1–SIA 15–16. doi:10.1029/2002ja009430

Pérez, D., Wohlberg, B., Lovell, T.A., Shoemaker, M., Bevilacqua, R. (2014). Orbit-centered atmospheric density prediction using artificial neural networks. *Acta Astronautica*, *98*, 9–23. doi:10.1016/j.actaastro.2014.01.007

Qian, L., Burns, A., Emery, B., Foster, B., Lu, G., Maute, A., ... Wang, W. (2014). The NCAR TIE-GCM: A community model of the coupled thermosphere/ionosphere system. , *9780875904917*, 73-83. doi:10.1002/9781118704417.ch7

Ridley, A., Deng, Y., Toth, G. (2006). The Global Ionosphere–Thermosphere Model. *Journal of Atmospheric and Solar-Terrestrial Physics*, *68*(8), 839–864. doi:10.1016/j.jastp.2006.01.008

Siemes, C. (2019). *Swarm satellite thermo-optical properties and external geometry* (Memorandum 2.0 No. ESA-EOPG-MOM-MO-15). ESA. Retrieved from https//bit.ly/swarm_geom

Storz, M.F., Bowman, B.R., Branson, M.J.I., Casali, S.J., Tobiska, W.K. (2005). High accuracy satellite drag model (HASDM). *Advances in Space Research*, *36*(12), 2497–2505. doi:10.1016/j.asr.2004.02.020

Vallado, D.A., & Finkleman, D. (2014). A critical assessment of satellite drag and atmospheric density modeling. *Acta Astronautica*, *95*, 141–165. doi:10.1016/j.actaastro.2013.10.005

van den IJssel, J., Doornbos, E., Iorfida, E., March, G., Siemes, C., Montenbruck, O. (2020). Thermosphere densities derived from Swarm GPS observations. *Advances*

in Space Research, *65*(7), 1758–1771. doi:10.1016/j.asr.2020.01.004

Virtanen, P., Gommers, R., Oliphant, T.E., Haberland, M., Reddy, T., Cournapeau, D., … SciPy 1.0 Contributors (2020). SciPy 1.0: Fundamental algorithms for scientific computing in python. *Nature Methods*, *17*, 261–272. doi:10.1038/s41592-019-0686-2

Visser, P., Doornbos, E., van den IJssel, J., Teixeira da Encarnação, J. (2013). Thermospheric density and wind retrieval from Swarm observations. *Earth, Planets and Space*, *65*(11), 1319–1331. doi:10.5047/eps.2013.08.003

Wall, M.E., Rechtsteiner, A., Rocha, L.M. (2003). Singular Value Decomposition and Principal Component Analysis. In D.P. Berrar, W. Dubitzky, & M. Granzow (Eds.), *A practical approach to microarray data analysis* (pp. 91–109). Boston, MA: Springer US. doi:10.1007/0-306-47815-3_5

Wen, H.Y., Kruizinga, G., Paik, M., Landerer, F., Bertiger, W., Sakumura, C., … Mccullough, C. (2019). *Gravity recovery and climate experiment follow-on (GRACE-FO) Level-1 data product user handbook* (Vol. 11; Tech. Rep. No. JPL D-56935 (URS270772)). NASA JPL. Retrieved from https://bit.ly/grace_level1

Zeitler, L., Corbin, A., Vielberg, K., Rudenko, S., Löcher, A., BloSSfeld, M., … Kusche, J. (2021). Scale factors of the thermospheric density: A comparison of satellite laser ranging and accelerometer solutions. *Journal of Geophysical Research: Space Physics*, *126*(12). doi:10.1029/2021JA029708

3

Conclusions

This master's thesis aimed at investigating the accuracy improvement in orbit prediction of LEO objects by assimilating empirical thermospheric density observations into NRLMSISE-00 atmospheric model. The research questions were addressed through extensive simulations and analysis, which yielded important insights into the potential and limitations of the calibrated model. The main findings demonstrate that the dynamical environment is key for the improved model to outperform the widely used NRLMSISE-00 atmospheric model. Moreover, if the geometry of the satellite is a panel model is descriptive enough, the calibrated NRLMSISE-00 model always outperforms the original model. These findings have significant implications for the development of more accurate and reliable models for orbit prediction of LEO objects, at the cost of computational efficiency, which can help mitigate the risks associated with collisions and improve the efficiency of space operations.

3.1. Sub-research conclusions

Next, every sub-research question mentioned in section 1.1 of this report is answered with the results and methodology explained thoroughly in Chapter 2.

How does the improvement on accuracy of orbit prediction with a calibrated model vary with different solar activity conditions?

To investigate the effect of solar activity on the accuracy of orbit prediction when empirical thermospheric density observations are assimilated into NRLMSISE-00 atmospheric model, the model was calibrated and tested for different solar activity conditions. The calibration was performed using data from January 2019, which corresponds to low solar activity, and March 2022, which corresponds to medium solar activity. Six different combinations of atmospheric model and satellite geometry were tested: calibrated and nominal NRLMSISE-00 density model, cannonball, scaled, and unscaled panel model. A bootstrapping with 19 total windows was performed, and the median was computed for each option, satellite, and case. The improvement on accuracy appears to increase with the drag signal. For example, the best improvement is achieved during March 2022 for satellite Swarm C, as the median accuracy is reduced from 20.67 km with NRLMSISE-00 to 13.75 km with the calibrated model in case 2, while it even increases in case 1. For both satellites, for the two fitted geometries (cannonball model and scaled panel model), the prediction improvement during case 2 is better than in case 1.

However, further investigation might be needed, extending the test cases and the satellites considered. Nevertheless, a consistent improvement was only achieved when the modelled dynamical environment, satellite geometry and satellite attitude, was descriptive enough for the estimation of the initial state to converge.

How the improvement on accuracy of orbit prediction with a calibrated model vary with altitude?

Based on the results obtained from the analysis, the improvement in accuracy of orbit prediction with a calibrated model varies with altitude. The most significant difference observed in the propagation of the three satellites was the magnitude of the range, because of the decreasing atmosphere with altitude. For case 1, Swarm C range increased to 6 km, while GRACE-FO 1 range was bounded to 800 m, and Sentinel 1-A was bounded to 40 m. During case 2, as the density signal was higher, the maximum range

was 40 km, 10 km, and 500 m, respectively, as the altitude increased and the atmosphere vanished. Moreover, it was found that the improvement made by assimilating Swarm C density observations was higher when the drag signal was higher, i.e., in lower altitudes, and medium solar conditions. Thus, the greatest improvement, of 7 km was obtained for satellite Swarm C, at 480 km of altitude, while the improvement in Sentinel 1-A prediction, flying at an orbit of 690 km had an improvement below 10 m. However, further test, with more satellites, and epochs, might be needed to be extended to confirm this hypothesis.

Can the calibrated density model correctly predict the orbit of other objects, whose density observations are not assimilated into the model?

Yes, based on the results obtained from the analysis, it can be concluded that the calibrated density model is capable of correctly predicting the orbit of other objects, even if their density observations are not assimilated into the model. For instance, in Case 1, the accuracy of the GRACE-FO 1 orbit prediction increased from 0.38 km (d) to 0.36 km (c), while in Case 2, it improved from 3.04 km (d) to 2.75 km (c). These results demonstrate the effectiveness of the proposed approach in improving the accuracy of orbit predictions. Despite a decrease in accuracy improvement with altitude, the calibrated density model still outperforms the widely-used NLRMSISE-00 model, suggesting that the former can provide valuable insights and more accurate predictions for a wide range of altitude regimes. These findings underscore the potential benefits of incorporating calibrated density models in the design and operation of space missions that require precise orbit predictions, such as satellite constellations, space debris mitigation, and space situational awareness.

What dynamical model should be used to predict the orbit, and how does it affect the accuracy of orbit prediction with a calibrated model?

The dynamical model used to predict the orbit should include, at least, third body perturbations of the sun and the moon, geopotential up to order 200 for Swarm C, and 128 for GRACE-FO 1 and Sentinel 1-A, and SRP. These perturbations are important to properly model the gravitational and solar radiation pressure effects on the satellite's orbit. Other perturbations that could be included are the gravity bulge caused by ocean or solilunar tides, or the temporal variation of the geopotential contribution. The accuracy of orbit prediction with a calibrated model is affected by the level of detail and accuracy of the dynamical model used. A more accurate and detailed model can lead to better predictions of the satellite's orbit.

The use of order and degree 200x200, allows that, when performing an orbital determination fit to POD observations during a short period of time, the fitted C_D only captures the dynamics of the drag force. This order and degree comes at the cost of increased computational burden. Furthermore, the calibrated method requires calling NRLMSISE-00 twice, making it at least twice as computationally time-consuming as normal NRLMSISE-00. To mitigate this computational burden, NRLMSISE-00 grid can also be sampled in the altitude to perform interpolation of the temporal and spatial component at each call to the mitigated model, removing the need of calling two times NRLMSISE-00.

How does the coupling between C_D and density affect the accuracy of orbit prediction, and to what extent can this coupling be reduced with the calibrated model?

The coupling between the drag coefficient (C_D) and density is a crucial factor affecting the accuracy of orbit prediction. This is because both parameters are multiplied by each other, resulting in a coupled effect of estimation. If C_D and the thermospheric density model are not in the same scale, it becomes necessary to fit them consistently. Estimating the drag coefficient has led to improvements in both the nominal and calibrated NRLMSISE-00 models. However, the extent of improvement in the calibrated model compared to the nominal NRLMSISE-00 model is slight and not always guaranteed, as it varies with the satellite, epoch, and geometry. The calibrated density model has included 11 calibration parameters, while the C_D is a linear multiplication to the density calibration. To partially mitigate the coupling between the parameters, a panel model can be used to define the drag contribution. However, the panel model must be scaled to the POD observations to ensure accuracy.

How does the calibrated density model interacts with different satellite geometries?

The calibrated density model has been tested with different satellite geometries, including cannonball, scaled panel model, and unscaled panel model for Swarm C, GRACE-FO 1, and Sentinel 1-A. The best results were obtained with the cannonball model after fitting the C_D, which was comparable with the scaled macro model. However, the unscaled panel model, only non-fitted geometry, only achieved similar results to the fitted geometries for GRACE-FO 1, and the Swarm C panel model was not able to represent the satellite well enough. This might be due to a 32% difference with high-fidelity

models (March et al., 2019) or due to a flaw in the implementation. The initial state estimation is crucial for correcting any flaws in the satellite geometry and ensuring accurate orbit prediction. While high fidelity models can be implemented for density modelling and POD community, they may be too detailed for typical needs. Therefore, a calibrated density model with a simplified satellite geometry, such as the cannonball model, can provide accurate results while being computationally efficient.

As an additional note, it is worth mentioning that the unscaled panel model for GRACE-FO 1 using the calibrated density model achieved an accuracy of 2.89 km, while the cannonball model achieved 2.75 km, and the scaled panel model achieved 2.47 km for the same satellite (March et al., 2019). These results demonstrate the importance of using an appropriate satellite geometry and the potential benefits of fitting the C_D in the calibrated density model for accurate orbit prediction.

What are the limitations of a prediction with the calibrated density model?

The limitations of the calibrated density model include several factors that can impact the accuracy of the orbit prediction. These include:

1. A poorly descriptive dynamical model: The accuracy of the density model relies on the accuracy of the dynamical model used to propagate the satellite's orbit. If the dynamical model is inadequate or incomplete, it can result in inaccurate orbit predictions. Because of this, the geopotential contribution was increased to 200x200 for the calibrated model to achieve superior performance.

2. A non-descriptive satellite geometry: The satellite's geometry determines the orientation and shape of the satellite, which affects drag and Solar Radiation Pressure (SRP). A non-descriptive or inaccurate geometry can lead to errors in the initial state estimation and subsequent orbit prediction.

3. A wrong attitude: The attitude of the satellite, which determines its orientation with respect to the Earth, can also impact the accuracy of the orbit prediction. A wrong attitude can result in errors in the drag and SRP perturbations and lead to inaccurate orbit predictions.

4. Not enough observations or observations with significant uncertainties: The accuracy of prediction is related to the quantity and quality of the observations used in the initial state estimation. Insufficient observations or observations with significant uncertainties can limit the accuracy of the density model and result in inaccurate orbit predictions.

Overall, these limitations suggest that the calibrated density model should be used with caution and in conjunction with other methods and models to improve the accuracy of orbit predictions.

In addition to the limitations already mentioned, there are several other factors that could impact the performance of the calibrated density model, but its study was out of the scope of this master's thesis. For example, predicting solar indices and attitude can be challenging due to the complexity of these variables and their impact on the thermosphere. The use of the local solar time as independent variable in the two-dimensional grid used to perform the PCA. Additionally, the dynamical environment can also be further analysed to better understand the limitations and performance of the calibrated density model.

3.2. Main research conclusion

In this section, the main research conclusion is answered after answering the sub-research questions:

How much can assimilating empirical thermospheric density observations retrieved from GNSS data into the NRLMSISE-00 atmosphere model improve the orbit prediction of LEO objects?

Assimilating empirical thermospheric density observations retrieved from GNSS data into the NRLMSISE-00 atmosphere model can improve the orbit prediction of LEO objects. The test performed in this master's thesis improved the range of orbital prediction by up to 18 km, for GRACE-FO 1, during high solar activity, with the unscaled panel model. The median of the bootstrapping simulation was reduced from 17.98 km to 2.89 km. For Swarm C, the scaled panel model during high solar activity was able to reduce the range from 20.67 km to 13.75 km. The results suggests that the improvement is better when the drag signal is higher, that is, with increasing solar conditions and decreasing altitude. Furthermore, the importance of a detailed dynamical environment and satellite geometry have been analysed thoroughly in this report. However, the coupling between the drag coefficient and the density

model should be considered, and the initial state estimation and satellite geometry should be carefully taken into account to ensure accurate orbit prediction.

3.3. Recommendations and further research

While this master's thesis provides valuable insights into the accuracy of orbit prediction for LEO objects when assimilating empirical thermospheric density observations into the atmospheric model, there are still several areas for further research.

One of the most important areas is to investigate other sources of uncertainty, such as, instead of using observed values for $F_{10.7}$ and a_P, using predicted values. As mentioned in Chapter 1, the uncertainty on the indices can be bound to 50%, being one of the main sources of uncertainty in the models. The coupling of the indices with the calibration of the density model might be explored when characterizing the uncertainty. The attitude of the spacecraft has been imported and interpolated from ESA data. Simulating the attitude would increase the uncertainty. Additionally, performing a realistic uncertainty characterization and propagation would be valuable to understand the limitations of the method, and to what extent the orbital uncertainty is reduced when employing a calibrated model.

The calibrated NRLMSISE-00 model could be compared with other recent density models such as DTM2020, that is also fitted in the least squares sense to Swarm TMD observations. The grid on the density could use Local Solar Time (LST) as the independent variable instead of the longitude, as the changes in atmospheric TMD are more sensitive to it.

Furthermore, needing to increase the order and degree of the geopotential perturbation to 200x200 was an unexpected result, as, although the acceleration is of the same order, the error in propagation (not using as ground truth POD orbits) with a lower order and degree is of a secondary relevance. Investigating other perturbations for the dynamical environment, such as atmospheric tides, temporal variation of the gravity field, and the influence of the tidal bulge in the propagation would also provide valuable insights, while out of the scope of this work. A thorough analysis on the use of POD orbits, and the potential of using TLE as observations, might be needed when analysing the dynamical environment.

Finally, increasing the number of objects to test, and the testing periods, would be useful to validate the hypothesis drafted from the results. A space debris object could be tested, which is expected to give similar improvements than the cannonball model of the satellites if the quality and quantity of the TLE observations is enough. Overall, there are many areas for further research that would advance our understanding of orbit prediction and improve the accuracy of predictions for LEO objects when using improved atmospheric density models, currently a research gap in the space research community.

A

Reference frames

This appendix chapter introduces and discusses four different reference frames that have been used throughout this study. The first reference frame is the GCRF, which is an inertial reference frame fixed with respect to the distant stars. The second reference frame is the ITRF, which is a rotating, non-inertial, Earth-centred reference frame that is fixed with respect to Earth's surface. The third reference frame is the body frame, which is a local reference frame fixed to a particular object or system and typically defined by the Tangential-Normal-Along track reference frame (TNW) directions. Finally, the fourth reference frame is the wind frame, which is a local reference frame aligned with the direction of the wind. Each of these reference frames should be applied to a particular application. In the following sections, each of the frames is defined, either in absolute terms or as a transformation from another frame.

A.1. International Terrestrial Reference Frame (ITRF)

The ITRF, also known as Earth-Centred, Earth-Fixed (ECEF) Frame, is a non-inertial reference frame whose origin is the centre of mass of the Earth. One of the main uses of ITRF, is observation of radar measurements of Earth's satellites, and POD ephemeris. Unlike the GCRF, which is fixed with respect to the distant stars, the ITRF rotates with the Earth. This reference frame is designed to be as precise as possible, taking into account factors such as tectonic movement and nonlinear station motions (Vallado, 2013), in order to provide an accurate representation of the Earth's surface. It is updated every few years to reflect the latest measurements and observations of the Earth's motion. Despite its non-inertial nature, the ITRF plays a crucial role in many applications, including satellite navigation and geodesy, as it provides a stable and consistent reference frame for measuring positions and distances on the Earth's surface. Its fundamental plane is the Earth equator, and the principal direction is Greenwich meridian.

A.2. Geocentric Celestial Reference System (GCRF)

The GCRF is the inertial counterpart of the ITRF. The GCRF combines the precision, nutation, rotation of the Earth, and polar motion to provide a stable and accurate reference frame for celestial observations and space missions. Unlike the ITRF, which rotates coherent with the Earth, the GCRF is fixed with respect to distant stars, which makes it an ideal reference frame for long-term observations and interplanetary missions. The GCRF is commonly used in astronomy, astrophysics, and space engineering applications, where a precise and consistent reference frame is essential for understanding and predicting celestial phenomena.

The transformation from a position vector in GCRF to ITRF is (Vallado, 2013):

$$\mathbf{r}_{GCRF} = \mathbf{P}(t)\mathbf{N}(t)\mathbf{R}(t)\mathbf{W}(t)\mathbf{r}_{ITRF} \tag{A.1}$$

where $\mathbf{r}_{GCRF}$ represents the position vector in inertial GCRF frame, $\mathbf{r}_{ITRF}$ represents the position vector in non-inertial ITRF frame, $\mathbf{P}(t)$ is the precession matrix, $\mathbf{N}(t)$ is the nutation matrix, $\mathbf{R}(t)$ is the sidereal-rotation matrix, that is, the rotation of the Earth with respect to the sun, and $\mathbf{W}(t)$ is the polar-motion

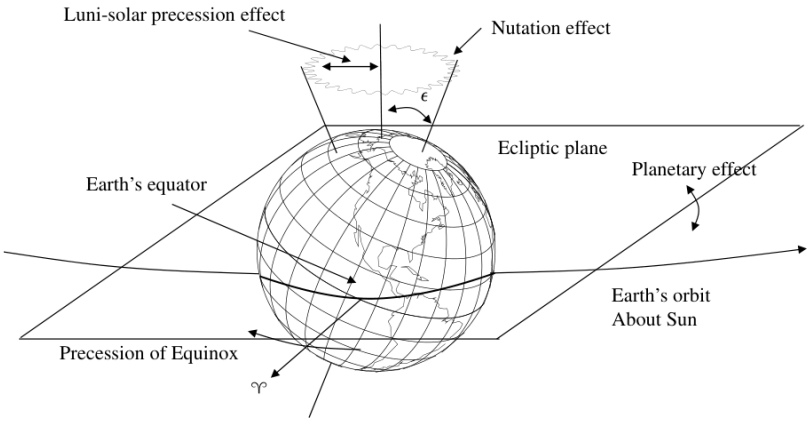

Figure A.1: Main perturbing forces that cause the precession and nutation of the Earth. Figure retrieved from Vallado (2013)-

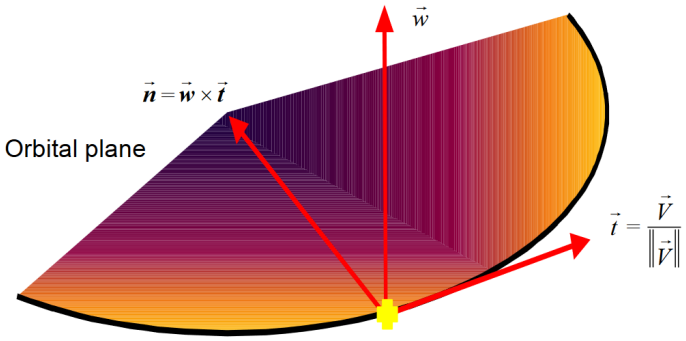

Figure A.2: Local Orbital TNW frame. Retrieved from CCSDS (2019).

matrix, i.e., the rotation of the polar axis. The main forces acting on Earth that allows to define the *sufficiently* inertial frame GCRF are sketched in Figure A.1

A.3. Local orbital frame

Through the report, a TNW local reference frame has also been mentioned. There are several ways to define local orbital frames, but the latest convention has been used (CCSDS, 2019) to define the TNW.

The TNW frame is a local reference frame that is commonly used in aerospace engineering for describing the motion of a flying object. It is a non-inertial reference frame that is fixed to the object, and its axes are tangent, normal, and along the velocity vector of the object, respectively. The tangent axis is perpendicular to the local vertical and points in the direction of the velocity vector, the normal axis is perpendicular to the tangent axis and points towards the centre of the Earth, and the along track axis completes the right-handed trihedron. It is described on Figure A.2. The TNW frame is useful for describing the motion of an object because it separates the motion into three distinct components: the velocity component along the tangent axis, the acceleration component along the normal axis, and the position component along the along track axis. This allows for a more intuitive understanding of the motion of the object, as each component can be analysed separately. The drag acceleration is mainly in the tangential direction.

The TNW frame is often used in satellite and spacecraft control systems, as it provides a natural reference frame for describing the orientation and motion of the object. The orientation of the TNW frame can be defined using either Euler angles or quaternions, depending on the specific application.

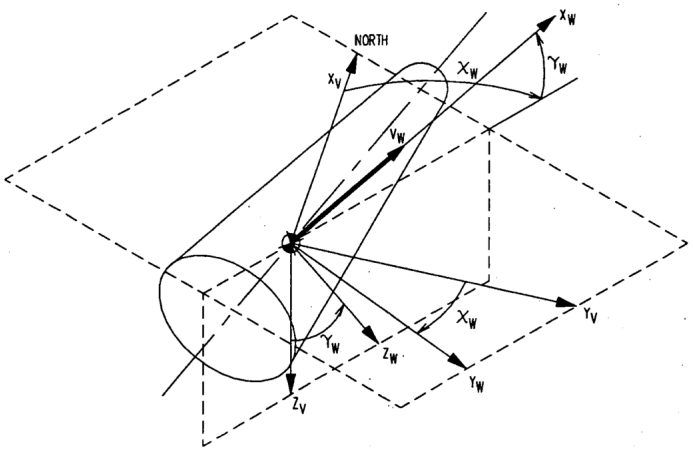

Figure A.3: Relation between wind frame (index W) and vertical frame (index V), equivalent to TNW frame. Retrieved from Mooij (1994).

A.4. Body frame

The body frame is a local reference frame that is fixed to a particular object or system, such as a satellite or a spacecraft. Unlike the ITRF and GCRF, which are global reference frames that are fixed with respect to the Earth and distant stars, respectively, the body frame is a local frame that changes with the attitude of the object. The body frame is typically defined by a right-handed trihedron with the x-axis pointing towards the front of the satellite (in the plane of symmetry), the z-axis pointed downwards in the plane of symmetry, and the y-axis completes the right-handed trihedron (Mooij, 1994). The specific definitions of the x- and y-axes differ depending on the actual satellite shape. For Swarm C, GRACE-FO 1, and Sentinel 1-A, the geometrical definitions are defined by Siemes (2019), Wen et al. (2019), and GMV (2019), respectively.

The orientation of the body frame is usually defined using attitude data in quaternion form, which allows for efficient computations without encountering singularities that may arise when using Euler angle rotations. By using quaternions, it is possible to represent any attitude in a three-dimensional space without encountering singularities that can occur with Euler's matrix rotations.

The body frame is useful in applications where it is necessary to describe the orientation and motion of a particular object, such as spacecraft attitude control, precise definition of a spacecraft geometry with a panel model, or aircraft flight dynamics.

A.5. Wind frame

The wind frame is a local reference frame that is aligned with the direction of the wind. It is typically used in aerospace applications to describe the motion of an aircraft or spacecraft relative to the surrounding air. The wind frame is defined by three directions: the wind direction, the lateral direction, and the vertical direction. The relative motion between the satellite and the and atmosphere, which includes the satellite velocity, the rotational velocity of the atmosphere with Earth, and the actual wind, defines the direction of the oncoming wind.

The wind direction is parallel to the direction of the oncoming wind, the lateral direction is perpendicular to the wind direction and to the satellite position in ITRF frame, and the vertical direction is perpendicular to both the wind and lateral directions, creating a right-handed trihedron. The wind frame is useful in applications such as drag computation in LEO, or aircraft flight dynamics.

Regarding the wind velocity vector, it can be computed with several models, like Horizontal Wind Model 2014 (HWM14; Drob et al., 2015), each one with an associated uncertainty. The most simplified model, and the one used throughout this report, is to assume that the atmosphere is calm, and only the rotation of the Earth with respect to inertial axes is taken into account. Including a more precise wind model is outside the scope of this work, but, as described in Chapter 3, if the accuracy of the dynamical model used can be improved, the calibration of the density model will improve further. However, whether including a detailed wind model constitutes a first-order improvement or a second-

order improvement needs to be further investigated.

B

LSE parameter selection and validation

LSE is a statistical method that allows us to estimate the value of a parameter by minimizing the sum of the squares of the differences between the estimated values and the observed values, weighted by the inverse of the variances of the observed values. In this master's thesis, LSE has been used to calibrate the density model to Swarm C observations. The algorithm has been build from scratch to fully understand the importance of each parameter. In this section, the validation approach that has been used to create the algorithm is described. Although the algorithm used in Chapter 2 is linear, a non-linear LSE was presented to handle different parameter sets. The nomenclature used in this section is the following:

- $\mathbf{y}_0 \equiv \mathbf{y}(t_0)$: Set of parameters to be estimated at the initial epoch t_0. A priori information can be included in the vector $\mathbf{y}_0^{apr}$.
- $\mathbf{p}$: parameters from NRLMSISE-00 that are not estimated.
- $\mathbf{x}_i \equiv \mathbf{x}(t_i)$: State vector at an epoch t_i. Initial state vector at epoch t_0: $\mathbf{x}_0 \equiv \mathbf{x}(t_0)$. During this section, it is the logarithm of the density.
- $f \equiv f(\mathbf{y}_0, \mathbf{p}, t_i)$: Propagation function that allows to obtain the reference (as in obtained by propagating) state vector $\bar{\mathbf{x}}_i$ at epoch t_i:

$$\bar{\mathbf{x}}(t_i) = f(\mathbf{y}_0, \mathbf{p}, t_i) \tag{B.1}$$

- $\mathbf{\Phi}_i \equiv \mathbf{\Phi}(t_i, t_{i-1})$: State transition matrix, obtained either analytically or numerically from the propagator f:

$$\mathbf{\Phi}_i = \frac{\partial \mathbf{x}_i^{\text{ref}}}{\partial \mathbf{x}_{i-1}^{\text{ref}}} = \mathbf{\Phi}(t_i, t_0)\mathbf{\Phi}(t_{i-1}, t_0)^{-1} \tag{B.2}$$

- z_i: Observed measurements at epoch t_i.
- $\hat{z}_i$: Predicted measurements at epoch t_i. The predicted measurements are related to the state with function g_i:

$$\hat{z}_i = g_i(t_i, \bar{\mathbf{x}}_i) \tag{B.3}$$

  When assimilating density measurements, it is the identity function: $\hat{z}_i = g_i(t_i, \bar{\mathbf{x}}_i) = \bar{\mathbf{x}}_i$.

- h_i: Measurement function. $\hat{z}_i$ can also be expressed in terms of the propagation function, such that $h_i = f_i \circ g_i$:

$$\hat{z}_i = h_i(t, \mathbf{y}_0) \tag{B.4}$$

  Again, when directly assimilating density measurements,

$$\hat{z}_i = \bar{\mathbf{x}}_i = f_i(t, \mathbf{y}_0) \tag{B.5}$$

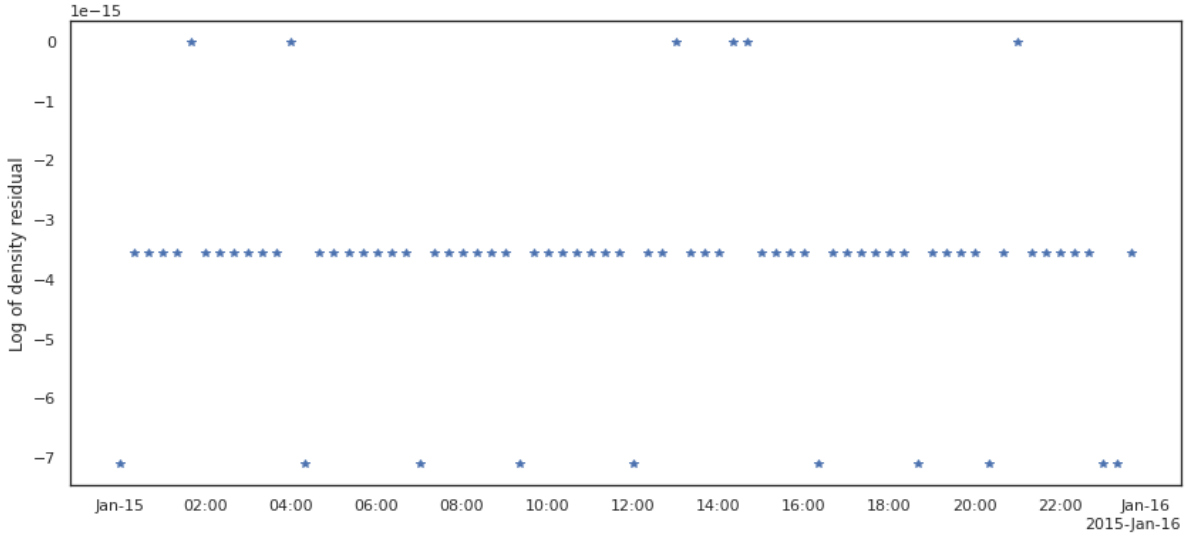

Figure B.1: Residuals of the first dummy calibration performed to validate the LSE method implemented

- $\mathbf{H}$: Jacobian of the measurement function. After linearization, h_i is substituted by the Jacobian:

$$\mathbf{H}_i = \frac{\partial h_i(t, \mathbf{y}_0)}{\partial y_i} \tag{B.6}$$

- $\mathbf{R}$: Measurement noise. Inverse to the weight of each measurement:

$$\mathbf{R}^{-1} = \mathbf{W} = \mathbf{S}^2 = \text{diag}(\sigma_1^{-2}, \dots, \sigma_n^{-2}) \tag{B.7}$$

- Residual Δz_i to minimize:

$$\Delta z = z - \hat{z} = z - h(\mathbf{y_0}) = z - \bar{\mathbf{x}}_i \tag{B.8}$$

First, the LSE was tested with an initial set of parameters y_0 which are $F_{10.7}$, A_P, `ptm[0]`, and `pt[0]`, internal variables defined in NRLMSISE-00 code that define the exospheric temperature. The parameters were chosen from previous literature (Forootan et al., 2020). The initial set was the reference value y_0^{apr}, plus a deviation of a 10%:

$$y_0 = y_0^{apr} + \Delta y_0 \tag{B.9}$$

The observations were the computed density from NRLMSISE-00 using y_0^{apr}. The output of the calibration is expected to be the correction that needs to be summed to the initial parameter to compute the original NRLMSISE-00, that is, $-\Delta y_0$.

However, above strategy was not successful as initially designed, because `ptm[0]` and `pt[0]` are correlated with exactly -1: both parameters are only used to compute the exospheric temperature, multiplied by each other. Thus, it did not always converge to the initial parameters, but to parameters that multiplied give the same result. For example, Figure B.1 shows the residuals before and after the calibration. The covariance and correlation matrices after the calibration are shown in Figure B.2, where it is clear that the problem is ill-posed.

Although the parameters were wrongly selected, the LSE was validated. The method was also tested with an initial reference y_0 as given by Equation (B.9), and observations with a Gaussian noise of 10%:

$$z_i = \hat{x}(y_0^{ref}) + \mathcal{N}(0, \sigma = 0.1 \cdot \text{STD}\left(\hat{x}(y_0^{ref})\right)) \tag{B.10}$$

The result, again, should be the correction, but the residuals should be sampled as a Gaussian distribution with standard deviation $0.1 \cdot \text{STD}\left(\hat{x}(y_0^{ref})\right)$. Figure B.3 confirms the initial expectations. Also, the fitness of the method $J = \Delta z \cdot \Delta z^T$, i.e., the dot product of the residuals, was equal to 1, which confirms that the method is performing correctly.

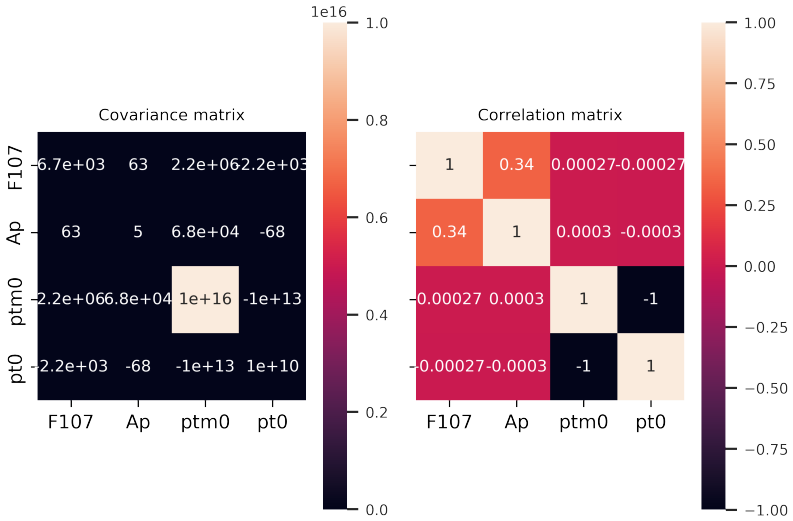

Figure B.2: Covariance and correlation matrices of the first calibration performed, considering as parameters $F_{10.7}$, A_P, `ptm[0]`, and `pt0`

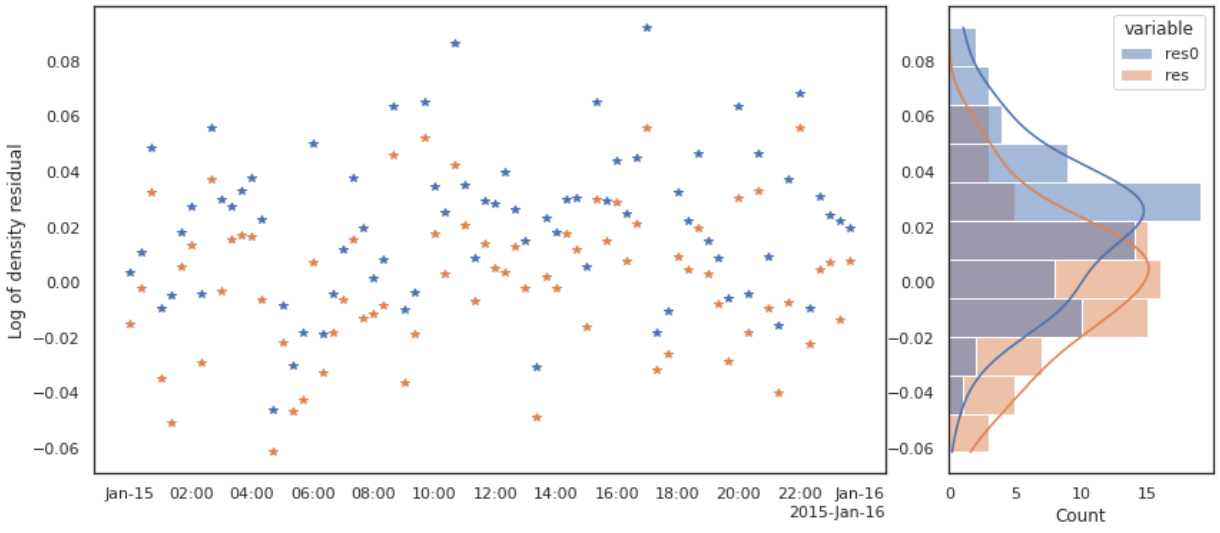

Figure B.3: Residuals of the second dummy calibration performed to validate the LSE method implemented, that is, including Gaussian noise on the observations

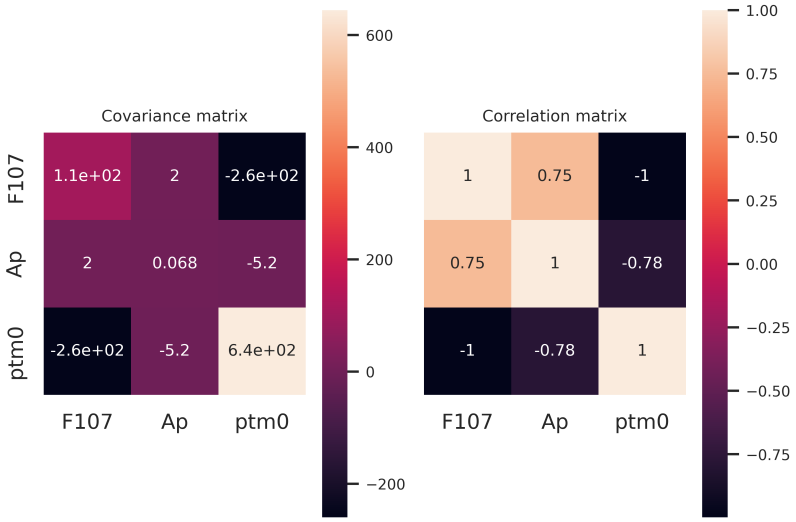

Figure B.4: Covariance and correlation matrices of the first calibration performed, considering as parameters $F_{10.7}$, A_P, and `ptm[0]`

Furthermore, the limits of the convergence were examinated, and a perturbation from 15% to 20% to the initial parameters was found to be the limit of the linearization on the density measurements. However, as Figure B.2 shows, the selection of the initial parameters was wrong, a new set of parameters y_0 was chosen: $F_{10.7}$, A_P, and `ptm[0]`. Selecting `ptm[0]` or `pt[0]` is equivalent, as it was shown before. The resulting covariance and correlation matrices are shown in Figure B.4. In this case, the solar index $F_{10.7}$ was found to have a direct correlation with the internal parameter `ptm[0]`.

Therefore, the parameters y_0 to calibrate were selected as the ones described in Chapter 2, that is, a parameter for each mode of the PCA.

C

Verification and validation

In this chapter, the validation strategy for each of the individual tasks performed during the master's thesis is sketched. It has been divided in three sections: section C.1, that summarizes the procedure to correctly import Swarm C density observations, use the NRLMSISE-00 model and compares both; section C.2, which summarizes the strategy followed to validate the PCA decomposition and the estimation algorithm; and section C.3, which summarices the stepts taken to design the dynamical environment and to validate the attitude used with the panel model.

C.1. NRLMSISE-00 model

The NRLMSISE-00 model is a widely used semi-empirical model for the density, temperature, and atmospheric composition in the thermosphere, which uses $F_{10.7}$ and A_P indices as input. It has been internally adjusted to match several sources of atmospheric data, such as spectrometer and incoherent Scatter-radar measurements, drag measurements and satellite-borne accelerometer datasets (Hedin, 1987; Picone et al., 2002). While the use of operational indices is an advantage of the model, the output density can have up to 30% uncertainty, which is a significant limitation. Additionally, the variability of density can be large depending on the input options, such as the use of daily A_P or 4-hourly a_P indices, $F_{10.7}$ or $F_{10.7A}$, etc... Therefore, it is important to validate the model's output against other sources of atmospheric data and operational software to ensure its correct use. In this section, the validation procedures used in this study are described, which consist of three steps: first, the import of Swarm C density observations is validated, then, the input parameters used for NRLMSISE-00 are validated as the recommended one, and last, the output density is validated with a software version of NRLMSISE-00 used operationally, and verified against the density database downloaded from Swarm C.

C.1.1. Importing of Swarm C density observations

Swarm C is one of the three satellites of the Swarm mission, launched by ESA in 2014 to measure the magnetic field and electric field of the Earth. The satellite carries instruments that can precisely measure the acceleration field on the spacecraft. Then, the GNSS tracking dat is used to eliminate any bias on the measurements of the drag force, and, with a high-fidelity geometric model of the satellite, to obtain measurements of the atmospheric density. The Swarm C density observations are available in a dataset that includes measurements from April 2014 to current time, and they can be used to calibrate atmospheric models such as NRLMSISE-00. In this section, the process of importing the Swarm C density observations is discussed, and the observations compared with the model's output.

The dataset used to import Swarm C density observations is available in ESA (2014). It contains seven columns: epoch, altitude, longitude, latitude, LST, argument of latitude, and TMD. First, Figure C.1 and Figure C.2 was created by replicating (van den IJssel et al., 2020, Figure 6) to verify that the same trend is obtained for the whole dataset. Each vertical line represents an orbit of Swarm C, and the plot is cropped at $3 \cdot 10^{-12}$. Qualitatively, Figure C.1 corresponds with (van den IJssel et al., 2020, Figure 6), and the trend followed by the density in Figure C.2 is the same as in literature.

For completeness, Figure C.3 shows the density measurements along with the density value computed by NRLMSISE-00 at the epoch and location of each observation for two years: 2014, and

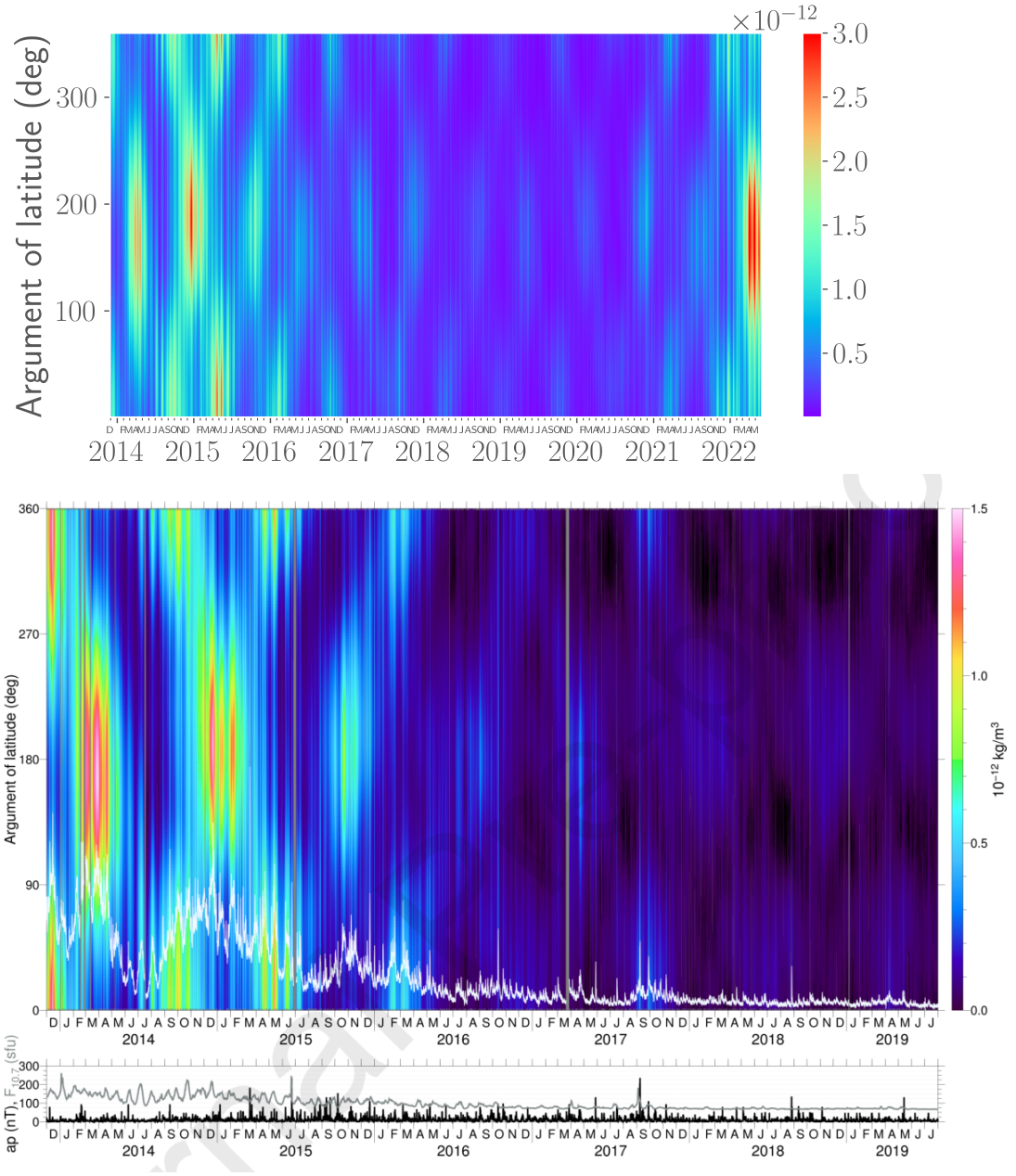

Figure C.1: Colour map of Swarm C density measurements as retrieved from ESA (2014) (top). Replicated (van den IJssel et al., 2020, Figure 6) (bottom).

2018, which correspond to a solar maximum and a solar minimum. The value of the mean and standard deviation between the two distributions (using the description from Chapter 2) is 0.84 and 46.99% for the solar maximum, and 0.59 and 56.04% for the solar minimum, which corresponds to the notion that NRLMSISE-00 captures better the atmospheric density during high solar activity periods.

C.1.2. Input parameters

The NRLMSISE-00 model requires several input parameters to compute the density and temperature in the thermosphere. These parameters include the year, day of year, seconds of the day, altitude, geodetic latitude, geodetic longitude, LST, and various solar and geomagnetic indices. The solar indices include the daily average $F_{10.7}$ proxy and its 81-day average ($\bar{F_{10.7}}$), while the geomagnetic index A_P is the daily average of the magnetic index. Additionally, the model includes several parameters used

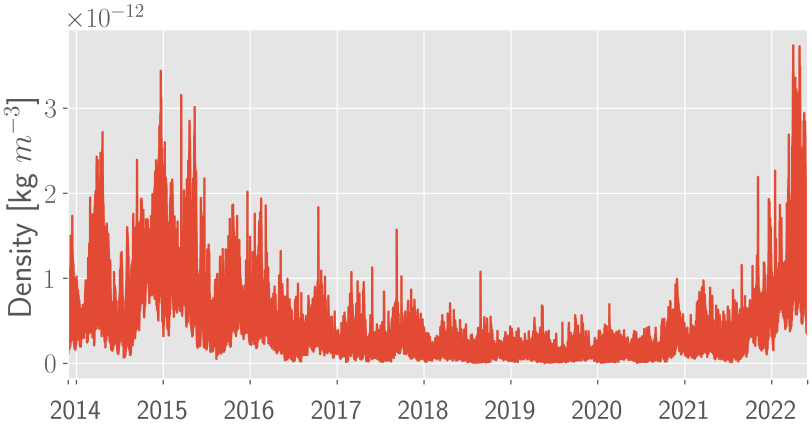

Figure C.2: Time series of Swarm C density measurements as retrieved from ESA (2014). Replicated (van den IJssel et al., 2020, Figure 6).

for internal adjustment, such as `ptm[0]` and `pt0`, which, multiplied, give the exospheric temperature, main parameter of the model. Instead of the daily average over one day of the parameter A_P, the 8-hourly mean can be used as input for NRLMSISE-00. Proper specification of these input parameters is crucial for accurate modelling of the density and temperature at lower altitudes of the atmosphere.

Every parameter has been carefully selected according to the recommendations given by Vallado and Finkleman (2014). However, there are two aspects that required further consideration to validate and verify the usage of the model: the selection of the LST, and the use of 8-hourly a_P indices.

Local Solar Time (LST) represents the time of day based on the position of the Sun relative to the local meridian of the observer, and it is an important input parameter for the NRLMSISE-00 model. According to NRLMSISE-00 documentation, LST is related to the seconds of the day and longitude of the observer by the formula:

$$\theta_{LST} = \frac{\texttt{sec}}{3600} + \frac{\lambda}{15} \tag{C.1}$$

where θ_{LST} is the LST in hours, `sec` is the number of seconds in the day (after midnight), and λ is the longitude of the spacecraft. However, θ_{LST} is defined in Vallado (2013) as:

$$\theta_{LST} = \theta_{GMST} + \lambda = \theta_{GMST,0h} + \omega_E \texttt{sec} + \lambda = \tag{C.2}$$

where θ_{GMST} is the position of the GMST with respect to the vernal equinox, $\theta_{GMST,0h}$ is the GMST at midnight and ω_E is the angular velocity of the Earth. It is important to note that the input LST for the NRLMSISE-00 model should correspond to the LST measured from GMST at midnight. Initially, $\theta_{GMST,0h}$ was summed twice, once in the computation of LST and again in the internal computation of the model. To avoid this double counting, it is necessary to use the correct formula for LST as specified in the NRLMSISE-00 documentation.

To verify the importance of using the correct formula for LST in the NRLMSISE-00 model, we compared the output densities obtained by using Equation (C.2) (which accounts for $\theta_{GMST,0h}$ twice) and Equation (C.1) (which avoids the double counting) with empirical density observations from the Swarm satellite mission. Specifically, the database of Swarm C densities was used to obtain the seconds of the day and longitude for several orbits, and computed the corresponding LST using both equations. Apart from the density at each epoch, the database includes information about the LST, longitude, altitude, latitude, and argument of latitude. Figure C.4 shows that when Equation (C.2) was used, the difference between the computed LST and the one from the database is minimal. The differences are due that Swarm C density database is computed with the mean equinox, and not with the apparent equinox, which does not include secular and periodic contributions. This provides further evidence of the importance of using the correct formula for LST in the NRLMSISE-00 model to ensure accurate density predictions.

Space weather indices are another important input parameter for the NRLMSISE-00 model, which are used to account for variations in the atmospheric density and temperature due to changes in the

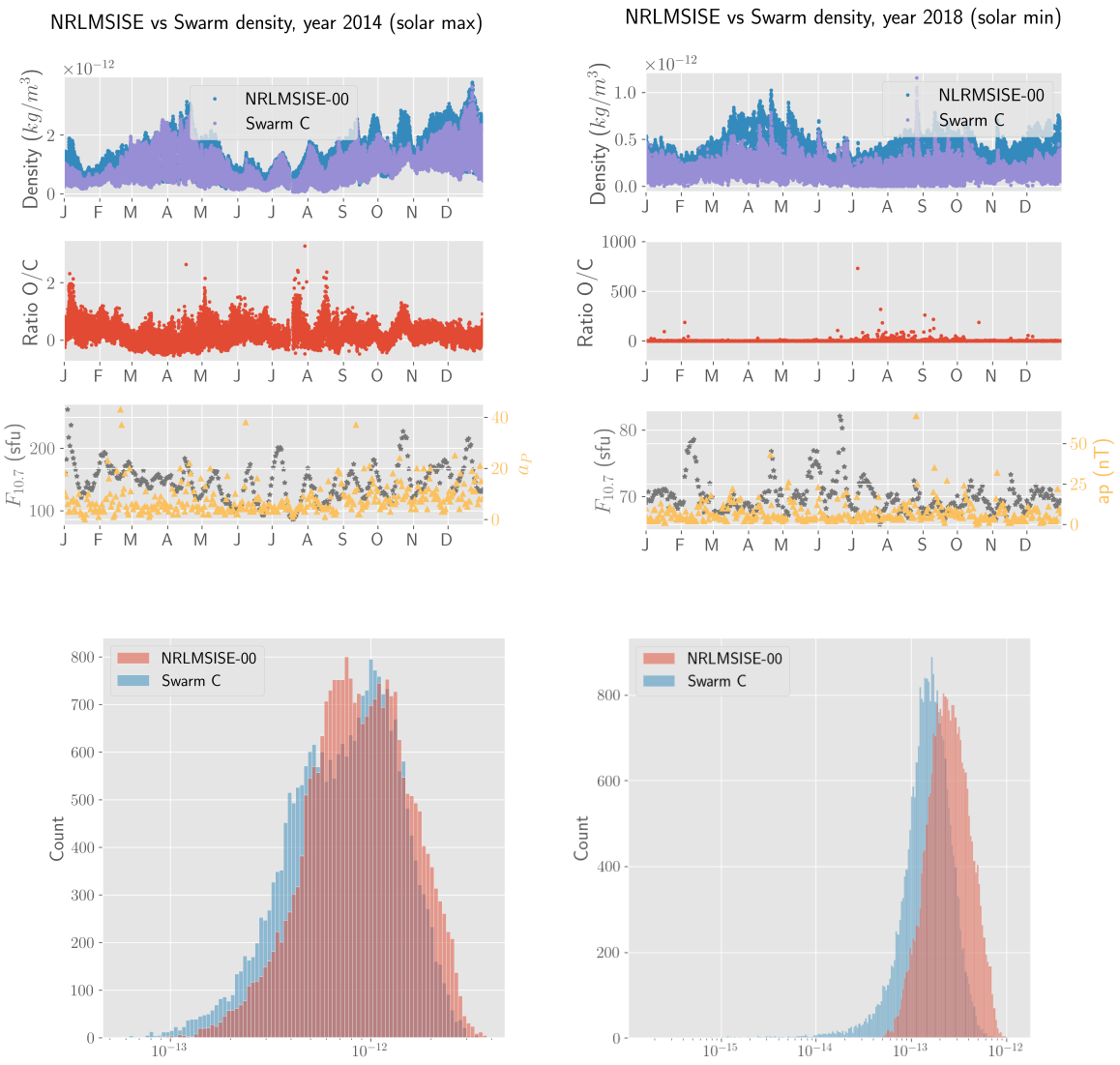

Figure C.3: Density measurements of Swarm C satellite, along with the computed value (top, upper half); ratio between observed and computed density values (middle, upper half); and $F_{10.7}$ and A_P values for each epoch (bottom, upper half). Histogram of measurements the measurements vs computed density at the lower half. Repeated for 2014 (left), solar maximum, and 2018 (right), solar minimum

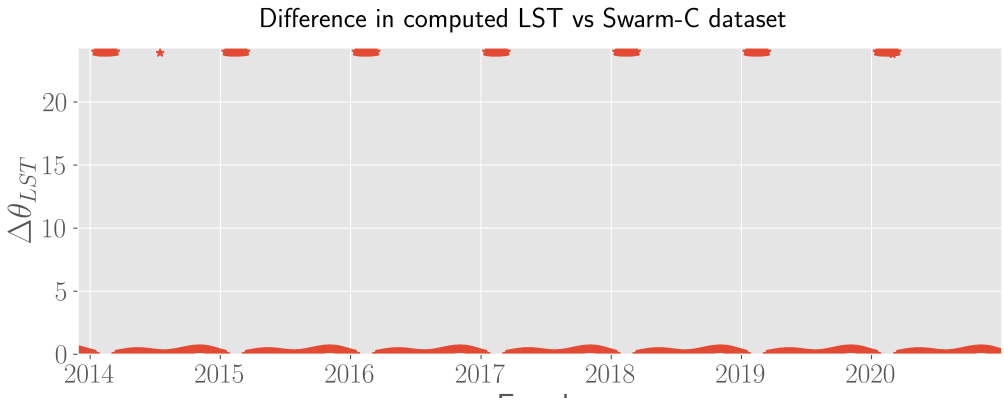

Figure C.4: Comparison between computed LST using Equation (C.2) and Swarm C dataset.LST in hours.

Earth's magnetic field. The NRLMSISE-00 model uses two different indices, the solar proxies $F_{10.7}$ and $\bar{F_{10.7}}$, and the geomagnetic index A_P. There is consensus on using the solar proxies as indicated by the model documentation, that is, using the mean value $\bar{F_{10.7}}$ for the previous day, and the adjusted values to exactly 1 AU (Picone et al., 2002; Vallado and Finkleman, 2014). Furthermore, it is recommended to use the 8-hourly indices, or even to interpolate the indices to the epoch that is being computed. To verify that the use of 8-hourly indices improves the accuracy of the model, a comparison was performed between the output density obtained with the mean A_P over one day and with the 8-hourly indices.

The results showed that the use of hourly ap indices leads to better agreement with observed densities.

C.1.3. Comparison with other sources

Comparing different implementations of NRLMSISE-00 is necessary to validate that the implementation being used is functioning correctly and accurately reproducing the output of the original model. To avoid that errors are introduced during implementation, such as the use of inappropriate indices, inputs, incorrect assumptions, or misinterpretation of the original source code documentation. These errors can lead to differences in the output of different implementations, which can result in incorrect data analysis. By comparing the output of different implementations, any discrepancies or errors can be identified and corrected, increasing confidence in the accuracy of the model output. The implementation used to calibrated NRLMSISE-00 has been compared with two other sources: Swarm C density observations previously imported, to validate that the results are the same as in literature; and a nominal propagation of an orbit with GMV software, operational software used at GMV.

To compare with the **Swarm C density dataset**, Figure 8 from van den IJssel et al. (2020) is replicated in Figure C.5. The measurements are resampled every 20 min, and, for each sampled measurement, the density obtained with NRLMSISE-00 is computed. The mean and standard deviation are computed with the procedure explained in Chapter 2. The general shape of the graphs is similar to the one present in literature, while the numbers are close enough: a value of 0.587 is obtained for the mean of the ratio, while a value of 56% is obtained for the standard deviation, in contrast with the values of 0.582 and 48.2% found in literature. Regarding the correlation value, it is computed here as the Pearson correlation coefficient, while the value in literature is only stated as a correlation value, without a description of the particular implementation. The slight improvements in correlation, and the slight increase in standard deviation might also be caused by a different use of NRLMSISE-00 inputs, such as the use of daily a_p indices. However, the qualitative shape of Figure C.5 corresponds with (van den IJssel et al., 2020, Figure 8), and the different values for the mean and standard deviation are small enough to validate NRLMSISE-00 input. Furthermore, only one point every 20 min is taken, which might affect the computation of the standard deviation, as (van den IJssel et al., 2020, Figure 8) has been computed with all the avbailable points.

Next, to compare with **GMV software**, a nominal propagation of a satellite at 400 km of height is computed. The satellite has a mass of 2160 km, radiation area of 38 m^2, and drag area of 6.35 m^2. Figure C.6 shows the drag contribution at inertial, GCRF, frame. Afterwards, the orbit was propagated with the default drag contribution in GMV software, and with the NRLMSISE-00 implementation defined above. The element to validate here is the implementation of NRLMSISE-00 that uses a `Python` wrapper over a `C` compiled version of NRLMSISE-00. The orbits were coincident below numerical tolerance, and thus, validated.

C.2. Assimilation of Empirical Density Measurements

With the final objective of improving the accuracy of density predictions in the Earth's atmosphere, density measurements have been assimilated into a decomposed version of NRLMSISE-00 numerical model. In this study, we have employed two methods: PCA, to extract the main relevant spatial and temporal components of NRLMSISE-00, and LSE, to assimilate empirical density measurements from the Swarm C satellite into the PCA model. PCA is a dimensionality reduction technique that allows us to identify and remove any redundant or noisy information from the empirical density dataset, while LSE is a regression method that estimates the NRLMSISE-00 model parameters using the density observations.

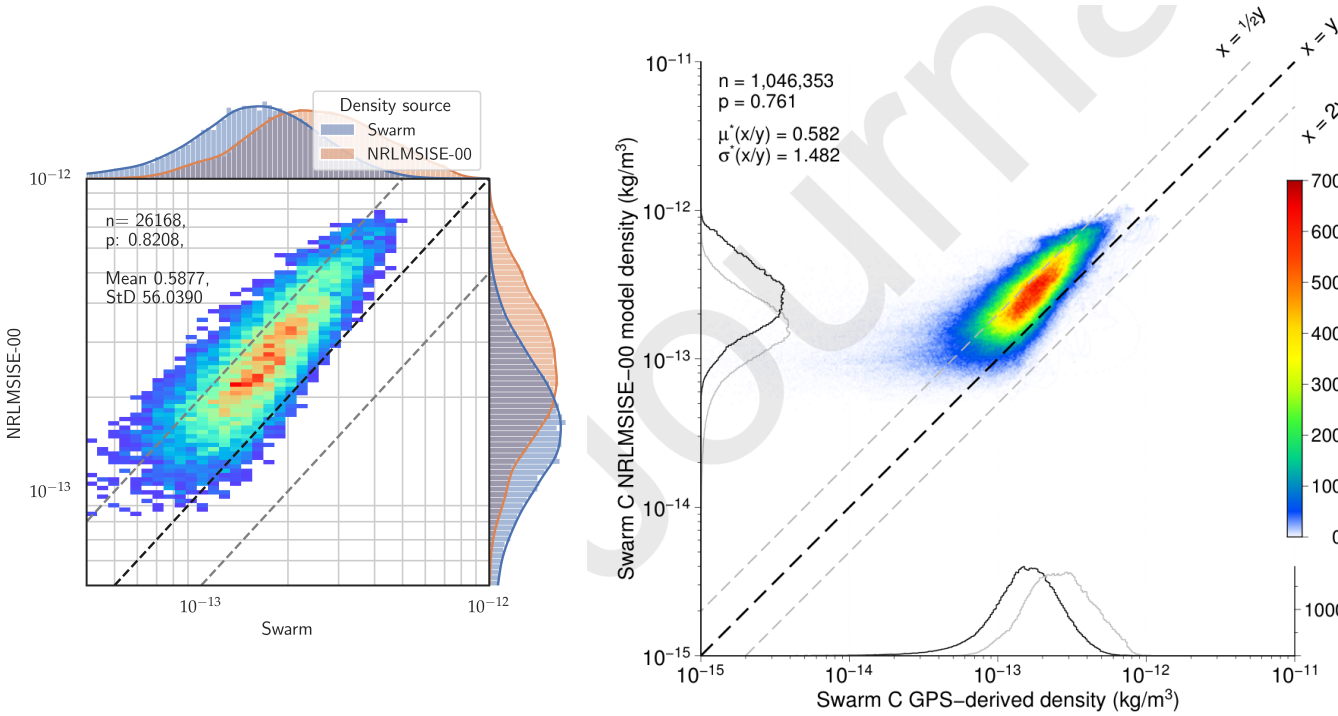

Figure C.5: Swarm C measurements vs modelled estimations for 2018 (left). Replicated Figure 8 from van den IJssel et al. (2020) (right).

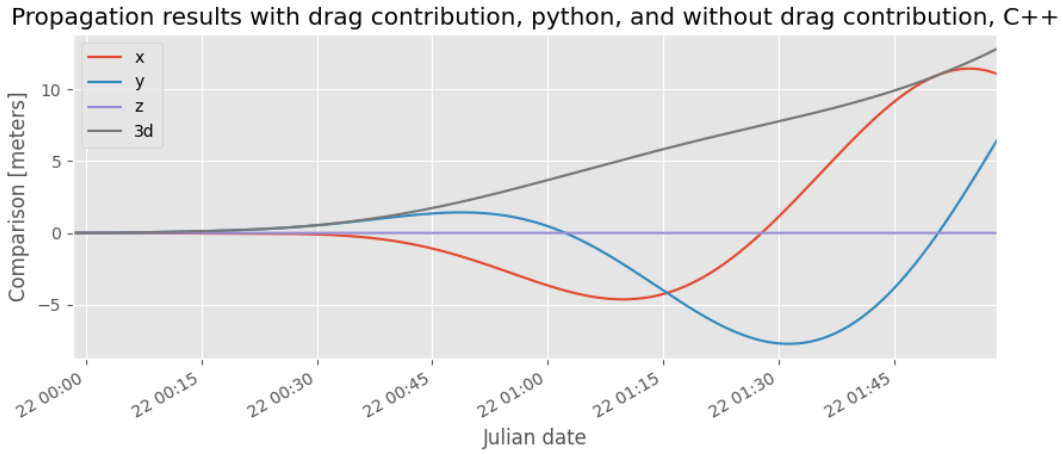

Figure C.6: Comparison of a nominal propagation of a satellite at 400 km of altitude including drag contribution and not including it. The drag contribution has been modelled to use the same version of NRLMSISE-00 presented above, also the one in GMV software

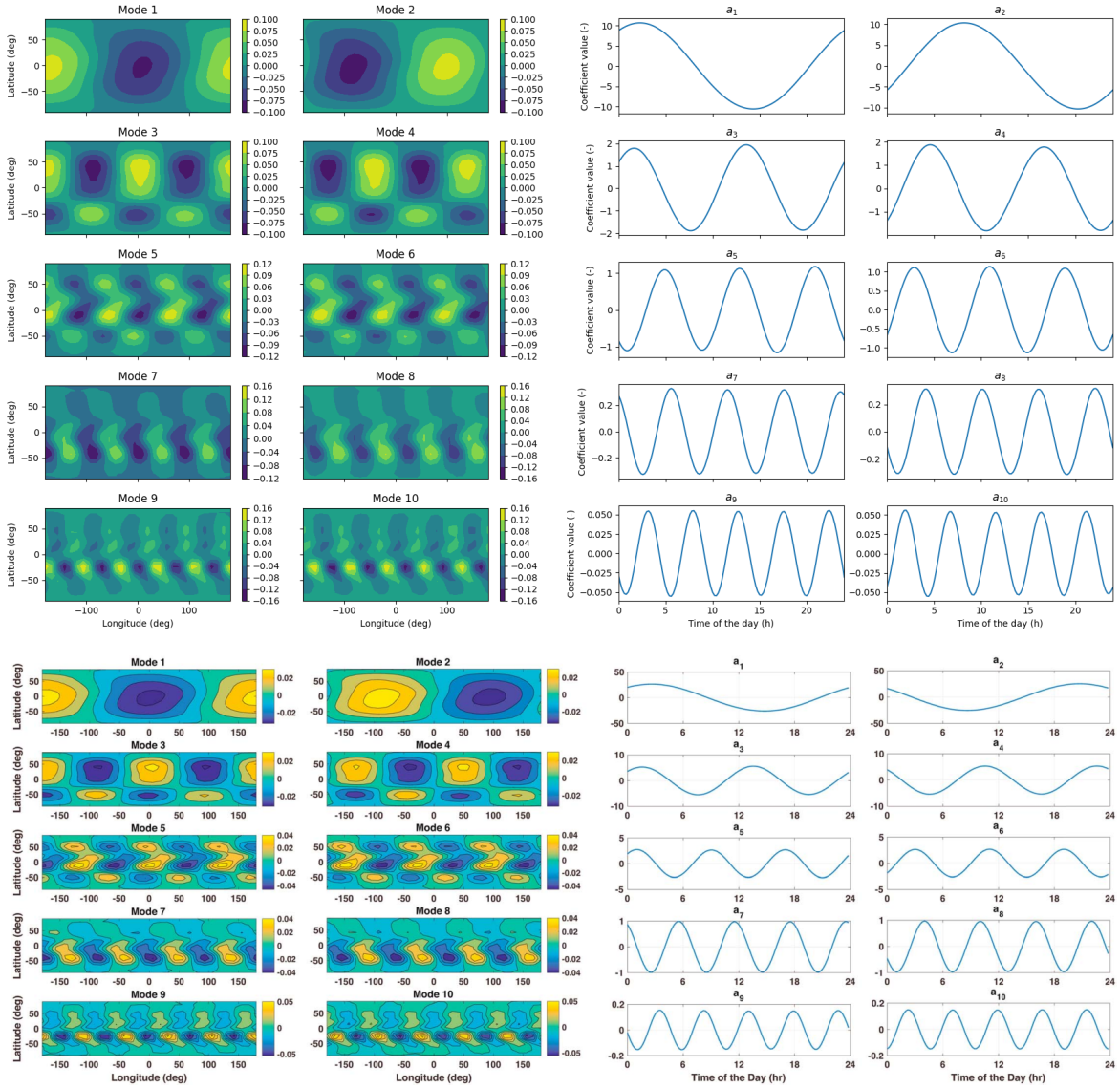

Figure C.7: Spatial and temporal evolution of the 10 principal components or modes of NRLMSISE-00 (top) during the 1st of January of Julian year 0, with $F_{10.7} = \bar{fsol} = 150$ sfu, and $A_P = 4$. The inputs of NRLMSISE-00 have been selected to match (Mehta and Linares, 2017, Figure 2) (bottom), and not any practical model.

C.2.1. PCA decomposition

Principal Component Analysis (PCA) is a statistical technique used to reduce the dimensionality of large datasets by identifying the underlying patterns and extracting the most relevant information. In the context of atmospheric modelling, PCA can be used to decompose the variability of the empirical density measurements into a smaller set of orthogonal modes that represent the temporal and spatial variation, which can then be used to improve the accuracy of the model predictions. It is based on linear algebra, in particular, the USV decomposition of non-squared matrices, extension of the decomposition into eigenvalues of squared matrices. The algorithmic implementation from `scikit-learn` has been used, which is validated by its creators.

The PCA decomposition of NRLMSISE-00 has been verified by comparing it with previous literature, in particular, replicating Figure 2 from Mehta and Linares (2017) in Figure C.7. By repeating a PCA on a similar grid, equivalent modes are obtained. Figure C.7 is created with the observed solar proxies $F_{10.7}$ and A_P as retrieved from Vallado and Kelso (2013). On the other hand, Mehta and Linares (2017) used values for the solar proxies $F_{10.7} = \bar{F_{10.7}} = 150$ sfu, and a geomagnetic index $A_P = 4$. The grid on longitude, latitude, and epochs per day is (30x20x120).

Although the absolute magnitude of each mode does not correspond with the literature, the shape and period of each node does, which is enough to validate a proper decomposition of NRLMSISE-00 at the most important components. As shown in Chapter 2, using a more detailed grid on the longitude does not modify the main nodes, but increasing the time-span of the calibration to one month brings forward slowly varying modes.

C.2.2. LSE verification

The parameter selection of the LSE estimation procedure is explained in Appendix B. A non-linear LSE was employed, and validated, to use the method with different sets of initial parameters. Finally, the parameters used were one per mode of the PCA calibration, which have a linear dependency with the density observations. Therefore, the validated non-linear method was finally employed with a linear procedure, in which matrix $\mathbf{H}$ can be either computed with the Jacobian, or used directly as an input. Both matrices were coincident for the calibration performed. Furthermore, to validate that the parameters employed are properly calibrated, apart from the results shown in Appendix B, a circular procedure was performed: first, the parameters were calibrated using the standard PCA decomposition as model, and with Swarm C observations as measurements. Afterwards, the density was computed using the calibrated PCA decomposition, and Swarm C observations again. The second time, the estimated parameters converged to the unit, validating the model.

C.3. Orbit prediction

Regarding the numerical propagation for the orbit prediction, an operational piece of software, GMV software, was used. Each individual function from GMV software is unit tested, and the usual functions are system-wide tested. Despite minor bugs found, the code is validated.

C.3.1. Dynamical environment

Nevertheless, the dynamical model used has been verified. For the cannonball model, the accelerations that have been obtained are plotted in Chapter 2, and the subsequent explanation and conclusions have been drawn. For the panel model, Figure C.8 shows the accelerations on a typical orbit for each satellite. The dynamical model chosen is validated for Sentinel 1-A and for GRACE-FO 1, and the attitude is validated too: a wrong attitude definition would cause the accelerations to oscillate quickly at each orbit. In fact, the interpolated attitude for Swarm C presents huge oscillations in magnitude: from a typical order of magnitude of $10 \times 10^7\,\mathrm{m\,s^{-2}}$, to an order of $10 \times 10^{-14}\,\mathrm{m\,s^{-2}}$, and therefore, its use is not recommended. The attitude used, as imported from (ESA, 2014), GRACE-FO 1 (Wen et al., 2019), and Sentinel 1-A (ESA, 2023), is therefore verified for Sentinel 1-A and GRACE-FO, but not for Swarm C.

C.3.2. Spacecraft attitude

Furthermore, the attitude of each satellite is defined by quaternions, to avoid singular points when computing Euler's angles of rotation. Each quaternion $\mathbf{q}$ is composed by four components $\mathbf{q} = (q_1, q_2, q_3, q_4)$. The norm of each quaternion should be the unit:

$$q_1^2 + q_2^2 + q_3^2 + q_4^2 = 1 \tag{C.3}$$

Furthermore, the angular velocity $\boldsymbol{\omega}$ of a satellite can be expressed as a quaternion with null scalar part $\boldsymbol{\omega} = (0, \omega_x, \omega_y, \omega_z)$, and they can be related with the quaternion differentiation's formula (Ioffe, 2023, Section 6):

$$\frac{d\mathbf{q}}{dt} = \frac{1}{2}\boldsymbol{\omega}\mathbf{q} \tag{C.4}$$

If the quaternions are differentiated with respect to time using finite differences of order one, Equation (C.4) can be used to obtain the angular velocity from the quaternions. As the movement of a satellite is defined by the movement in a conic section, the resulting angular velocity should be close to zero in x and z directions (Ioffe, 2023), and be around 1 mrad in y direction, either positive or negative depending on the spacecraft orientation: $\boldsymbol{\omega} \sim (0, \pm 1\,\mathrm{mrad}, 0)$.

The imported attitude data for GRACE-FO 1 and Sentinel 1-A has been correctly verified this way, as they assume a rotation from GCRF to body-centered frame. Swarm C imported attitude, on the other

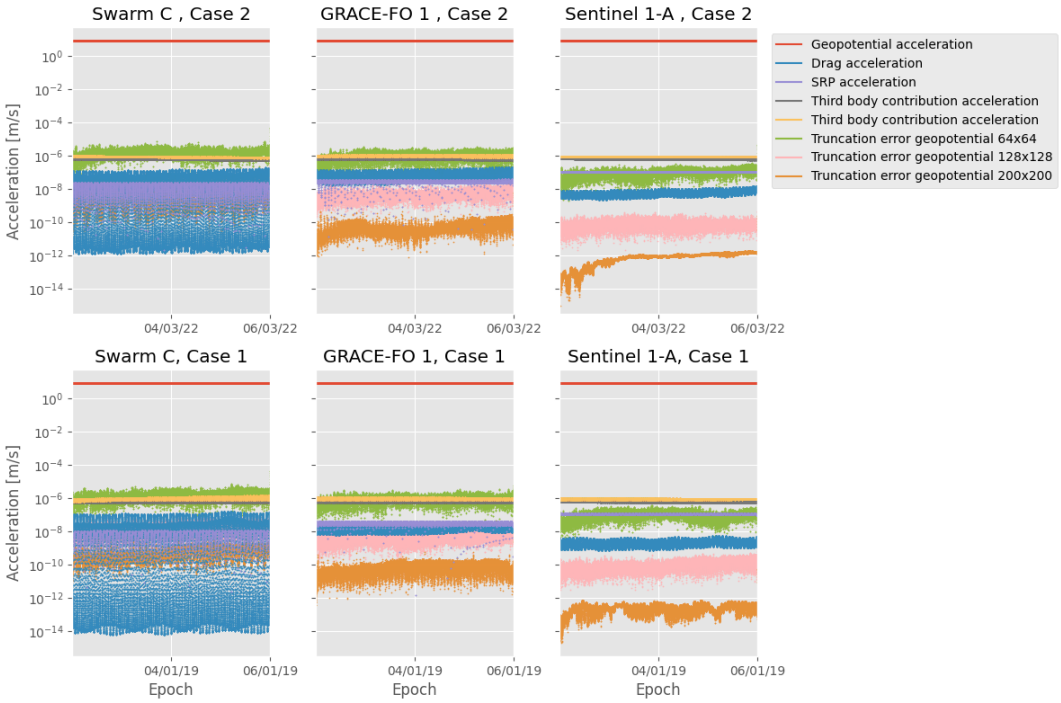

Figure C.8: Accelerations for a nominal propagation, for the three satellites, and two solar conditions, with a panel model geometry.

hand, defines a rotation from ITRF to body-centered frame. Thus, the rotation from ITRF to GCRF has been composed to verify the imported attitude. Table C.1, Table C.2, and Table C.3 show the angular velocity obtained from the first order differentiation of the quaternions for the three satellites. Although for Sentinel 1-A, the magnitude on the z axis is higher than on Swarm C and GRACE-FO 1, the same attitude data has been internally in GMV software development, and therefore, it has been already verified.

Table C.1: Verification of GRACE-FO 1 attitude imported from Wen et al. (2019).

Epoch	ω_x [rad s^{-1}]	ω_y [rad s^{-1}]	ω_z [rad s^{-1}]
2^{nd}Jan19 00:00:38.5	$-1.511 \cdot 10^{-6}$	0.001104	$-1.184 \cdot 10^{-6}$
2^{nd}Jan19 00:00:39.5	$-4.788 \cdot 10^{-7}$	0.001102	$1.476 \cdot 10^{-6}$
2^{nd}Jan19 00:00:40.5	$3.361 \cdot 10^{-7}$	0.001104	$-3.696 \cdot 10^{-7}$
2^{nd}Jan19 00:00:41.5	$-2.39 \cdot 10^{-6}$	0.001102	$1.154 \cdot 10^{-6}$
2^{nd}Jan19 00:00:42.5	$-1.564 \cdot 10^{-7}$	0.001102	$-4.328 \cdot 10^{-7}$
2^{nd}Jan19 00:00:43.5	$2.719 \cdot 10^{-7}$	0.001104	$1.255 \cdot 10^{-7}$
2^{nd}Jan19 00:00:44.5	$-2.214 \cdot 10^{-7}$	0.001102	$6.025 \cdot 10^{-8}$
2^{nd}Jan19 00:00:45.5	$-2.131 \cdot 10^{-6}$	0.001102	$-2.664 \cdot 10^{-7}$
2^{nd}Jan19 00:00:46.5	$-2.216 \cdot 10^{-7}$	0.001102	$6.13 \cdot 10^{-8}$
2^{nd}Jan19 00:00:47.5	$2.056 \cdot 10^{-7}$	0.001104	$6.206 \cdot 10^{-7}$

Table C.2: Verification of Swarm C attitude imported from Siemes (2019).

Epoch	ω_x [rad s^{-1}]	ω_y [rad s^{-1}]	ω_z [rad s^{-1}]
1^{st}Jan19 00:00:37.5	$6.71 \cdot 10^{-5}$	-0.001126	0.0001299
1^{st}Jan19 00:00:38.5	$6.955 \cdot 10^{-5}$	-0.001125	0.0001313
1^{st}Jan19 00:00:39.5	$6.793 \cdot 10^{-5}$	-0.001124	0.0001287
1^{st}Jan19 00:00:40.5	$6.915 \cdot 10^{-5}$	-0.001127	0.0001293
1^{st}Jan19 00:00:41.5	$6.748 \cdot 10^{-5}$	-0.001125	0.0001303
1^{st}Jan19 00:00:42.5	$6.857 \cdot 10^{-5}$	-0.001125	0.0001295
1^{st}Jan19 00:00:43.5	$6.758 \cdot 10^{-5}$	-0.001126	0.000127
1^{st}Jan19 00:00:44.5	$6.629 \cdot 10^{-5}$	-0.001124	0.0001304
1^{st}Jan19 00:00:45.5	$6.939 \cdot 10^{-5}$	-0.001126	0.0001294

Table C.3: Verification of Sentinel 1-A attitude imported from ESA (2023).

Epoch	ω_x [rad s^{-1}]	ω_y [rad s^{-1}]	ω_z [rad s^{-1}]
12^{th}Jan19 00:00:05.5	$7.741 \cdot 10^{-5}$	-0.0009283	-0.000514
12^{th}Jan19 00:00:06.5	$7.619 \cdot 10^{-5}$	-0.0009286	-0.0005124
12^{th}Jan19 00:00:07.5	$7.319 \cdot 10^{-5}$	-0.0009294	-0.0005126
12^{th}Jan19 00:00:08.5	$7.174 \cdot 10^{-5}$	-0.0009267	-0.0005103
12^{th}Jan19 00:00:09.5	$7.34 \cdot 10^{-5}$	-0.0009281	-0.0005094
12^{th}Jan19 00:00:10.5	$7.055 \cdot 10^{-5}$	-0.0009314	-0.0005126
12^{th}Jan19 00:00:11.5	$7.765 \cdot 10^{-5}$	-0.0009294	-0.0005093
12^{th}Jan19 00:00:12.5	$7.043 \cdot 10^{-5}$	-0.0009299	-0.0005122
12^{th}Jan19 00:00:13.5	$7.041 \cdot 10^{-5}$	-0.0009289	-0.0005096
12^{th}Jan19 00:00:14.5	$6.85 \cdot 10^{-5}$	-0.0009278	-0.0005109
12^{th}Jan19 00:00:15.5	$7.078 \cdot 10^{-5}$	-0.0009246	-0.000511
12^{th}Jan19 00:00:16.5	$7.969 \cdot 10^{-5}$	-0.0009265	-0.0005098

Bibliography

Bowman, B., Tobiska, W. K., Marcos, F., Huang, C., Lin, C., and Burke, W. (2008a). A new empirical thermospheric density model JB2008 using new solar and geomagnetic indices. In *AIAA/AAS Astrodynamics Specialist Conference and Exhibit*. American Institute of Aeronautics and Astronautics. doi: 10.2514/6.2008-6438.

Bowman, B. R., Tobiska, W. K., Marcos, F. A., and Valladares, C. (2008b). The JB2006 empirical thermospheric density model. *Journal of Atmospheric and Solar-Terrestrial Physics*, *70*(5), 774–793. doi: 10.1016/j.jastp.2007.10.002.

Bruinsma, S. (2015). The DTM-2013 thermosphere model. *Journal of Space Weather and Space Climate*, *5*, A1. doi: 10.1051/swsc/2015001.

Bruinsma, S., and Boniface, C. (2021). The operational and research DTM-2020 thermosphere models. *Journal of Space Weather and Space Climate*, *11*, 47–1. doi: 10.1051/swsc/2021032.

Bruinsma, S., Sutton, E., Solomon, S., Fuller-Rowell, T., and Fedrizzi, M. (2018). Space weather modeling capabilities assessment: Neutral density for orbit determination at low Earth orbit. *Space Weather*, *16*(11), 1806–1816. doi: 10.1029/2018SW002027.

Bruinsma, S., Boniface, C., Sutton, E. K., and Fedrizzi, M. (2021). Thermosphere modeling capabilities assessment: geomagnetic storms. *Journal of Space Weather and Space Climate*, *11*, 12. doi: 10.1051/swsc/2021002.

Callejón Cantero, M., Siemes, C., and Pastor, A. (2023). Improving orbit prediction via thermospheric density calibration. In T. Flohrer, R. Moissl, and F. Schmitz (eds.), *2nd NEO and Debris Detection Conference, Darmstadt, Germany, 24-26 Jan. 2023*, (pp. 1–13). ESA Space Debris Office. Retrieved from `https://bit.ly/neo_sst`.

CCSDS (2019). *Navigation Data Definitions and Conventions*. Tech. Rep., CCSDS. Retrieved from `https://bit.ly/ccsds_oem`.

Doornbos, E. (2011). *Thermospheric density and wind determination from satellite dynamics*. Ph.D. thesis, Technische Universiteit Delft. doi: 10.1007/978-3-642-25129-0.

Doornbos, E., and Klinkrad, H. (2006). Modelling of space weather effects on satellite drag. *Advances in Space Research*, *37*(6), 1229–1239. doi: 10.1016/j.asr.2005.04.097.

Doornbos, E., Klinkrad, H., Scharroo, R., and Visser, P. (2007). Thermosphere density calibration in the orbit determination of ERS-2 and Envisat. Retrieved from `https:\bit.ly/envisat_doornbos`.

Doornbos, E., Klinkrad, H., and Visser, P. (2008). Use of two-line element data for thermosphere neutral density model calibration. *Advances in Space Research*, *41*(7), 1115–1122. doi: 10.1016/j.asr.2006.12.025.

Drob, D. P., Emmert, J. T., Meriwether, J. W., Makela, J. J., Doornbos, E., Conde, M., Hernandez, G., Noto, J., Zawdie, K. A., McDonald, S. E., et al. (2015). An update to the horizontal wind model (HWM): The quiet time thermosphere. *Earth and Space Science*, *2*(7), 301–319. doi: 10.1002/2014EA000089.

Emmert, J., Drob, D., Picone, J., Siskind, D., Jones, J., M., Mlynczak, M., Bernath, P., Chu, X., Doornbos, E., Funke, B., Goncharenko, L., Hervig, M., Schwartz, M., Sheese, P., Vargas, F., Williams, B., and Yuan, T. (2021). NRLMSIS 2.0: A whole-atmosphere empirical model of temperature and neutral species densities. *Earth and Space Science*, *8*(3). doi: 10.1029/2020EA001321.

ESA (2014). *Swarm PDGS Data Access User Manual*. European Space Agency. Retrieved from https://bit.ly/swarm_pdgs.

ESA (2022). *ESA's Annual Space Environment Report*. LOG GEN-DB-LOG-00288-OPS-SD, Space Debris Office. Retrieved from https://bit.ly/esa_debris.

ESA (2023). The Copernicus Open Access Hub. Retrieved from https://scihub.copernicus.eu/.

Forootan, E., Farzaneh, S., Kosary, M., Schmidt, M., and Schumacher, M. (2020). A simultaneous calibration and data assimilation (C/DA) to improve NRLMSISE00 using thermospheric neutral density (TND) from space-borne accelerometer measurements. *Geophysical Journal International*, *224*(2), 1096–1115. doi: 10.1093/gji/ggaa507.

Friis-Christensen, E., Lühr, H., Knudsen, D., and Haagmans, R. (2008). Swarm – an earth observation mission investigating geospace. *Advances in Space Research*, *41*(1), 210–216. doi: 10.1016/j.asr.2006.10.008.

GMV (2019). *Sentinel-1 properties for GPS POD*. Tech. Rep. Retrieved from https://bit.ly/sentinel_pod.

Gondelach, D. J., and Linares, R. (2020). Real-time thermospheric density estimation via two-line element data assimilation. *Space Weather*, *18*(2). doi: 10.1029/2019sw002356.

Gondelach, D. J., and Linares, R. (2021). Real-time thermospheric density estimation via radar and GPS tracking data assimilation. *Space Weather*, *19*(4). doi: 10.1029/2020sw002620.

He, C., Yang, Y., Carter, B., Kerr, E., Wu, S., Deleflie, F., Cai, H., Zhang, K., Sagnières, L., and Norman, R. (2018). Review and comparison of empirical thermospheric mass density models. *Progress in Aerospace Sciences*. doi: 10.1016/j.paerosci.2018.10.003.

Hedin, A. E. (1987). MSIS-86 thermospheric model. *JGR. Journal of geophysical research. Part D, Atmospheres*, *92*(5), 4649–4662. doi: 10.1029/JA092iA05p04649.

van den IJssel, J., Doornbos, E., Iorfida, E., March, G., Siemes, C., and Montenbruck, O. (2020). Thermosphere densities derived from Swarm GPS observations. *Advances in Space Research*, *65*(7), 1758–1771. doi: 10.1016/j.asr.2020.01.004.

Ioffe, M. (2023). Quaternion differentiation. Retrieved from bit.ly/quat_diff.

ISO (1975). *Standard Atmosphere*. Standard ISO/TC 20/SC 6 2533:1975, ISO Central Secretary, Geneva, CH. Retrieved from https://www.iso.org/standard/7472.html.

Kim, I., Pawlowski, D. J., Ridley, A. J., and Bernstein, D. S. (2008). Localized data assimilation in the ionosphere-thermosphere using a sampled-data unscented Kalman filter. In *2008 American Control Conference*, (pp. 1849–1854). IEEE. doi: 10.1109/ACC.2008.4586761.

Klinkrad, H. (2006). *Space Debris: Models and Risk Analysis*. Springer-Verlag Berlin Heidelberg. doi: 10.1007/3-540-37674-7.

Licata, R. J., Mehta, P. M., and Tobiska, W. K. (2020). Impact of space weather driver forecast uncertainty on drag and orbit prediction. In R. Wilson, J. Shan, K. Howell, and F. Hoots (eds.), *2020 AAS/AIAA Astrodynamics Specialist Conference-423, Lake Tahoe, California*, vol. 175, (pp. 1941–1959). Univelt Inc.

Licata, R. J., Mehta, P. M., Tobiska, W. K., and Huzurbazar, S. (2022). Machine-learned HASDM thermospheric mass density model with uncertainty quantification. *Space Weather*, *20*(4). doi: 10.1029/2021sw002915.

March, G., Doornbos, E., and Visser, P. (2019). High-fidelity geometry models for improving the consistency of CHAMP, GRACE, GOCE and Swarm thermospheric density data sets. *Advances in Space Research*, *63*(1), 213–238. doi: 10.1016/j.asr.2018.07.009.

Matsuo, T., Fedrizzi, M., Fuller-Rowell, T., and Codrescu, M. (2012). Data assimilation of thermospheric mass density. *Space Weather*, *10*(5). doi: 10.1029/2012SW000773.

Mehta, P. M., and Linares, R. (2017). A methodology for reduced order modeling and calibration of the upper atmosphere. *Space Weather*, *15*(10), 1270–1287. doi: 10.1002/2017SW001642.

Montenbruck, O., and Gill, E. (2005). *Satellite Orbits: Models, Methods and Applications*. Springer Science & Business Media. doi: 10.1007/978-3-642-58351-3.

Mooij, E. (1994). *The motion of a vehicle in a planetary atmosphere*. Tech. Rep., Faculty of Aerospace Engineering, TUDelft.

Morozov, A. V., Ridley, A. J., Bernstein, D. S., Collins, N., Hoar, T. J., and Anderson, J. L. (2013). Data assimilation and driver estimation for the Global Ionosphere–Thermosphere Model using the ensemble adjustment Kalman filter. *Journal of Atmospheric and Solar-Terrestrial Physics*, *104*, 126–136. doi: 10.1016/j.jastp.2013.08.016.

Pardini, C., Moe, K., and Anselmo, L. (2012). Thermospheric density model biases at the 23rd sunspot maximum. *Planetary and Space Science*, *67*(1), 130–146. doi: 10.1016/j.pss.2012.03.004.

Picone, J. M., Hedin, A. E., Drob, D. P., and Aikin, A. C. (2002). NRLMSISE-00 empirical model of the atmosphere: Statistical comparisons and scientific issues. *Journal of Geophysical Research: Space Physics*, *107*(A12), SIA 15–1–SIA 15–16. doi: 10.1029/2002ja009430.

Pérez, D., Wohlberg, B., Lovell, T. A., Shoemaker, M., and Bevilacqua, R. (2014). Orbit-centered atmospheric density prediction using artificial neural networks. *Acta Astronautica*, *98*, 9–23. doi: 10.1016/j.actaastro.2014.01.007.

Qian, L., Burns, A., Emery, B., Foster, B., Lu, G., Maute, A., Richmond, A., Roble, R., Solomon, S., and Wang, W. (2014). The NCAR TIE-GCM: A community model of the coupled thermosphere/ionosphere system. *9780875904917*, 73–83. doi: 10.1002/9781118704417.ch7.

Ridley, A., Deng, Y., and Toth, G. (2006). The Global Ionosphere–Thermosphere Model. *Journal of Atmospheric and Solar-Terrestrial Physics*, *68*(8), 839–864. doi: 10.1016/j.jastp.2006.01.008.

Sáez Bo, D., and Escobar Antón, D. (2018). *Performance characterization of SST Systems based on Radar Sensors*. Master's thesis, Carlos III University of Madrid.

Siemes, C. (2019). *Swarm satellite thermo-optical properties and external geometry*. Memorandum 2.0 ESA-EOPG-MOM-MO-15, ESA. Retrieved from `https//bit.ly/swarm_geom`.

Storz, M. F., Bowman, B. R., Branson, M. J. I., Casali, S. J., and Tobiska, W. K. (2005). High accuracy satellite drag model (HASDM). *Advances in Space Research*, *36*(12), 2497–2505. doi: 10.1016/j.asr.2004.02.020.

Vallado, D. A. (2013). *Fundamentals of astrodynamics and applications*, vol. 12. Springer Science & Business Media, 4th ed.

Vallado, D. A., and Finkleman, D. (2014). A critical assessment of satellite drag and atmospheric density modeling. *Acta Astronautica*, *95*, 141–165. doi: 10.1016/j.actaastro.2013.10.005.

Vallado, D. A., and Kelso, T. (2013). Earth orientation parameter and space weather data for flight operations. In *23rd AAS/AIAA Space Flight Mechanics Meeting, Kauai, HI*, (pp. 2679–2698).

Visser, P., Doornbos, E., van den IJssel, J., and Teixeira da Encarnação, J. (2013). Thermospheric density and wind retrieval from Swarm observations. *Earth, Planets and Space*, *65*(11), 1319–1331. doi: 10.5047/eps.2013.08.003.

Wen, H. Y., Kruizinga, G., Paik, M., Landerer, F., Bertiger, W., Sakumura, C., Bandikova, T., and Mccullough, C. (2019). *Gravity recovery and climate experiment follow-on (GRACE-FO) Level-1 data product user handbook*. Tech. Rep. JPL D-56935 (URS270772), NASA JPL. Retrieved from `https://bit.ly/grace_level1`.

Zeitler, L., Corbin, A., Vielberg, K., Rudenko, S., Löcher, A., Bloßfeld, M., Schmidt, M., and Kusche, J. (2021). Scale factors of the thermospheric density: A comparison of satellite laser ranging and accelerometer solutions. *Journal of Geophysical Research: Space Physics*, *126*(12). doi: 10.1029/2021JA029708.